

RIDGE-RUNNEL MIGRATION - EXPERIMENT AND NUMERICAL INVESTIGATION

by

JENS FIGLUS, NOBUHISA KOBAYASHI,

AND CHRISTINE GRALHER

RESEARCH REPORT NO. CACR-10-02
JULY, 2010

CENTER FOR APPLIED COASTAL RESEARCH
OCEAN ENGINEERING LABORATORY
UNIVERSITY OF DELAWARE
NEWARK, DE 19716

ACKNOWLEDGMENTS

This study was supported by the U.S. Army Engineer Research and Development Center under Contract No. W912-09-C-0023.

TABLE OF CONTENTS

| | |
|---|----------|
| ABSTRACT | vii |
| Chapter | |
| 1 INTRODUCTION | 1 |
| 1.1 Motivation | 1 |
| 1.2 Previous Work | 3 |
| 1.3 Methodology and Scope | 5 |
| 2 RIDGE-RUNNEL EXPERIMENT | 9 |
| 2.1 Experimental Setup | 9 |
| 2.1.1 Sediment Characteristics | 11 |
| 2.1.2 Test Procedure | 14 |
| 2.2 Wave Generation and Measurement | 15 |
| 2.2.1 Wave Gauges | 15 |
| 2.2.2 Acoustic Doppler Velocimeters | 16 |
| 2.3 Profiling | 18 |
| 2.3.1 Laser Line Scanner | 18 |
| 2.3.2 Ultrasonic Thickness Gauges | 23 |
| 2.4 Overwash Collection | 25 |
| 2.4.1 Water Collection Basin | 25 |
| 2.4.2 Sand Trap | 26 |

| | |
|---|-----------|
| 3 RIDGE-RUNNEL DATA ANALYSIS | 29 |
| 3.1 Morphology and Overwash | 29 |
| 3.1.1 Ridge-Runnel Migration | 30 |
| 3.1.2 Transport Rates | 37 |
| 3.1.3 Ridge and Runnel Geometry Evolution | 41 |
| 3.2 Wave Gauge Records | 46 |
| 3.2.1 Offshore Parameters | 46 |
| 3.2.2 Setup, Wave Height, and Wet Probability | 51 |
| 3.2.3 Wave Spectra | 59 |
| 3.2.4 Wet and Dry Gauges | 62 |
| 3.3 Velocity Measurements | 67 |
| 3.3.1 3D ADV | 67 |
| 3.3.2 2D ADV | 71 |
| 3.3.3 Vectrino | 75 |
| 4 NUMERICAL MODEL CSHORE | 81 |
| 4.1 Combined Wave and Current Model in the Wet Zone | 81 |
| 4.2 Probabilistic Model for Wet and Dry Zone with Ponded Water | 85 |
| 4.3 Sediment Transport Model | 92 |
| 5 COMPARISON OF NUMERICAL MODEL WITH RIDGE-RUNNEL EXPERIMENT | 99 |
| 5.1 Input Parameters | 99 |
| 5.2 Hydrodynamics | 102 |
| 5.2.1 Free-Surface Elevation | 103 |
| 5.2.2 Cross-Shore Velocity | 112 |
| 5.2.3 Wet Probability | 120 |
| 5.3 Profile Evolution | 123 |
| 5.4 Wave Overtopping and Overwash Rates | 128 |

| | | |
|----------|---|------------|
| 6 | VERIFICATION OF CSHORE | 131 |
| 6.1 | Laboratory Dune Data | 131 |
| 6.2 | Field Dune Data | 141 |
| 7 | CONCLUSIONS | 147 |
| | REFERENCES | 151 |

ABSTRACT

Ridge-runnel systems are dynamic coastal morphological features made up of a shore-parallel emergent crest (ridge) separating a body of water (runnel) from the open ocean. Since ridges may comprise large volumes of sediment, their movement plays a key role in the coastal sediment budget. Yet, sediment transport processes responsible for ridge-runnel evolution are still poorly understood and modeling capabilities remain limited. This may be attributed in part to the complex interaction of the hydrodynamic forcing and the morphological response, but also to the limited amount of associated field and laboratory data.

Ridge-runnel systems appear at various scales and locations as long as during the tide cycle the ridge crest becomes exposed, trapping water in a depression on its landward side. Wave overtopping may then carry sediment and water over the ridge crest into the runnel while at the same time changing the ridge-runnel shape. Water collected in the runnel forms a seaward flow through rip channels around the ridge if the runnel is drained, or returns seaward over the ridge if the runnel is not drained and filled up.

For the present study, two laboratory tests representing the drained and undrained scenarios were conducted in a movable-bed wave flume. Runnel drainage in this wave flume experiment was mimicked by allowing wave overtopping of a vertical wall landward of the runnel. Measurements of high-resolution profile changes, overwash transport rates, shallow water flow velocities and free surface elevation from outside the surf zone to the intermittently wet and dry zone produced a unique ridge-runnel migration data set to quantify the drainage effect on ridge migration.

The onshore ridge migration occurred in both tests, but almost four times faster for the drained test. This suggests that rapid beach recovery may occur if the runnel is drained through rip channels.

The numerical model CSHORE is modified to allow a ponded runnel in predicting beach profile evolution where the ponded water causes deposition of sediment transported over the ridge crest. The ponded water effect on cross-shore sediment transport is shown to be crucial in reproducing the measured evolution of the ridge-runnel system with and without drainage. Additional comparisons with various measured field and laboratory data sets substantiate the CSHORE improvement and underline the importance of ponded water for morphological changes on sandy beaches.

Chapter 1

INTRODUCTION

Ridge-runnel systems are dynamic coastal morphological features made up of a shore-parallel emergent crest (ridge) separating a body of water (runnel) from the open ocean. As such they are present in the intermittently wet and dry zone of the beach profile where fluctuating water levels and waves constantly reshape their appearance. The migration of ridge-runnel systems is linked to complicated hydrodynamic and sediment transport processes and is the focus of this investigation.

1.1 Motivation

Beaches suffering from erosion due to severe storm impact may recover under normal wave conditions. The process of beach recovery, however, is much slower since it occurs under less energetic wave conditions. The onshore migration of ridge-runnel systems is considered to play a significant role in the beach recovery process since ridges may contribute large amounts of sediment to the coastal sediment budget. Improving our understanding of the hydrodynamics and sediment transport mechanisms involved in ridge-runnel migration is essential for predicting morphology evolution in the intermittently wet and dry zone of the beach. However, these processes are hard to predict partly because of the poor understanding of hydrodynamics and sediment dynamics in the swash zone on a complicated bathymetry. Ridge-runnel systems are most prominent on sandy beaches after severe storm events with elevated storm tide levels.

Several processes contribute to the evolution of ridge-runnel systems. Waves overtop and move the ridge crest, carrying water and sediment into the runnel. As the runnel fills up, return flows are initiated either as offshore return currents over the ridge crest or through rip channels intersecting the ridge. Figure 1.1 depicts these two scenarios of ridge-runnel systems found in the field. On the left is a photograph of Vero Beach, Florida, at high tide after hurricane Jeanne had passed through (Photo by NOAA http://www.nws.noaa.gov/mdl/rip_current/). The alongshore ridge-runnel system is intersected by a rip channel facilitating return flow out of the runnel. The right photo shows a post-storm ridge-runnel system at South Bethany, Delaware (Photo by DNREC <http://www.swc.dnrec.delaware.gov/SiteCollectionDocuments/Soil/Shoreline/StrikeBalance.pdf>, page 13). This runnel seems to be alongshore uniform and does not include rip channels within this photo. Offshore return flow of excess runnel water occurs over the ridge crest.



Figure 1.1: Photos of two different ridge-runnel systems formed during storm conditions. The left image shows a ridge-runnel system intersected by a rip-channel at Vero Beach, FL (photo by NOAA). The right image was taken at South Bethany, DE (photo by DNREC) after a North-Easter had passed through. The ridge-runnel system appears to be alongshore uniform.

The ponded water in the runnel facilitates sediment deposition since flow velocities inside the runnel are small compared to the wave overtopping velocities

on the ridge crest. This attenuation effect may be a key factor for rapid beach recovery and needs to be investigated further.

Accurate numerical modeling of morphological changes remains one of the most challenging feats in coastal engineering. The numerical treatment of the wet and dry zone is uncertain because a range of time and length scales in hydrodynamics and sediment transport. Individual waves, wave groups, daily water level changes, storm surges, and the long-term succession of storms and periods of calm conditions all contribute to the ever changing bottom morphology. Modeling ridge-runnel evolution is of specific interest in this study because of the potential role in rapid beach recovery. Similar crest and trough arrangements occur at different length scales for sand waves, intertidal bars, and even entire island-bay systems.

Quantitative field and laboratory data on ridge-runnel systems are scarce. Most existing field investigations are confined to a specific location and short time periods (not more than a few tide cycles). Numerous qualitative observations of related phenomena have been reported but detailed measurements of wave motion, flow velocities, sediment transport rates and profile changes are rare. The following section lists a few examples in the literature.

1.2 Previous Work

Ridge-runnel systems appear in the literature under various names mostly related to intertidal bars. Masselink et al. (2006) gave an overview of available field observations. They categorized intertidal bars into three different regimes according to their scale. Slip-face bars are the largest intertidal bar feature and make up the first regime. Low-amplitude ridges are more subdued morphological forms and fall into the second regime. Sand waves represent relatively marginal repetitive features making up the third regime. The tests carried out in the present investigation pertain to the slip-face category. Masselink et al. (2006) pointed out the dominant importance of tidal water level variations and wave processes in shallow water depths

for the evolution of such features. They qualitatively described hydrodynamic and sediment transport processes and their morphological response.

Several authors discussed field measurements of onshore migrating intertidal bars. Robin et al. (2009) measured morphological changes, hydrodynamics and sediment tracer movement for one intertidal bar located in an ebb delta inlet system. They carried out four short experiments (one tide cycle each) under different wave and tide conditions. Their observed ridge-runnel system (slip-face bar type) exhibited onshore migration on the order of $1\text{ cm}/\text{min}$ during high-energy wave conditions. No movement was registered during calm periods. The migration occurred at times in the tide cycle when the ridge-runnel system was located in the shoaling, surf, and swash regimes. Houser and Greenwood (2007) reported onshore migration of a ridge-runnel system (swash bar) during a storm on the Danish coast (two tide cycles). They explained the migration by the gradient in the fluid acceleration skewness. Aagaard et al. (2006) observed onshore migration of an intertidal bar over four tide cycles and compared the difference in sediment transport and circulation patterns before and after the runnel had filled. Vincent and Green (1990) measured suspended sand concentration profiles and velocities near the crest of a ridge-runnel system on an English beach. Two 12-min time series were recorded in a non-breaking wave regime where onshore-skewed wave-induced flows close to the bed were found to be responsible for the shoreward flux of sand.

Numerical approaches to ridge-runnel migration varied tremendously depending on desired detail and represented time scale. Since our main interest pertains to the daily to monthly evolution of beach profiles and related engineering applications we will not focus on detailed wave-resolving models. A review by de Vriend et al. (1993) shed light on several mathematical approaches to long-term coastal morphology modeling. They explained models based on statistical extrapolation of past coastal behavior, semi-empirical models, and models using formally integrated

representations of inherent small-scale processes. The common goal is to reduce computational effort by eliminating details that may not be important for long-term morphology predictions. This leads to the creation of more transparent and stable models. Masselink (2004), for example, introduced a morphodynamic model to predict the behavior of multiple intertidal bars. They employed a sinusoidal sediment transport shape function shifted along the beach profile with regard to the tide level. In their formulation the runnels acted as sediment transport barriers which is supposed to simulate attenuation effects.

1.3 Methodology and Scope

The work cited in the previous section shows that ridge-runnel systems are in fact an important morphological feature because they affect the sediment transport patterns in the intermittently wet and dry zone significantly. We conducted a ridge-runnel experiment to investigate the evolution of these morphological features in a controlled laboratory setting. The experimental results are used to calibrate the process-based cross-shore numerical model CSHORE which is extended to a ridge-runnel system. The experiment was designed specifically to reproduce onshore migration of the most pronounced ridge-runnel type (slip-face bar) under fairly energetic wave conditions. Since evidence from field measurements suggests that active ridge migration occurs mainly while the crest is emergent (e.g. Robin et al., 2009), a constant still water level seaward of the ridge was adopted in the experiment.

The idealized top view schematics shown in Figure 1.2 represent the two different return flow scenarios found in ridge-runnel systems (Section 1.1). The left panel depicts the three-dimensional (3D) scenario where waves overtopping the emergent ridge fill the runnel and initiate offshore return flows through rip channels and back over the ridge. The right panel depicts the two-dimensional (2D) situation where no rip-channels are present. Reproducing these two scenarios in a 2D

laboratory flume requires a few simplifications. Figure 1.3 shows a side view of the two initial profiles in a sand flume with a fixed-height back wall to represent the 3D and 2D scenarios. The High Ridge (HR) setup in the left panel mimics 3D runnel drainage by allowing wave overtopping over the vertical wall at the landward end of the profile. High ridge pertains to the fact that the initial ridge crest is higher than the vertical wall crest. The LR or Low Ridge test (right panel), on the other hand, simulates the 2D scenario by preventing wave overtopping over the vertical wall. The entire profile including the water level was lowered in the LR test.

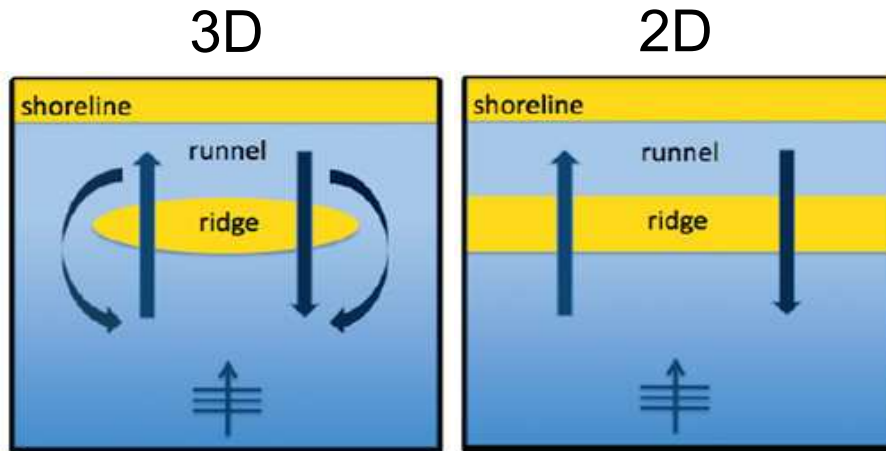


Figure 1.2: Schematic of 3D and 2D ridge-runnel scenarios. Figure adapted from Gralher (2010).

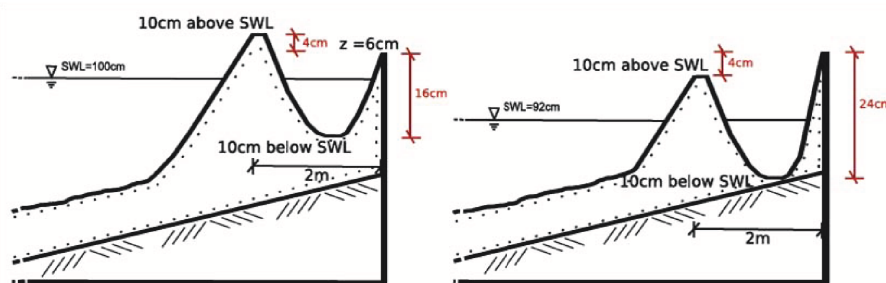


Figure 1.3: High Ridge (HR) and Low Ridge (LR) initial setup. The initial HR (LR) ridge crest is situated 4 cm above (below) the vertical wall crest. Figure adapted from Gralher (2010).

The experiment was conducted in a sand flume to monitor the morphological evolution of the two different ridge-runnel setups under irregular waves. Hydrodynamic measurements at different cross-shore locations were accompanied by overtopping and overwash collection behind the vertical wall. An innovative sand trap located inside a water collection basin behind the vertical wall enabled us to measure the temporal variations of overtopping and overwash transport rates.

The present study aims at creating a unique set of laboratory data pertaining to wave-induced ridge-runnel migration including the effect of water ponding on bottom profile changes. These data are then used to extend and calibrate the numerical model CSHORE (Kobayashi et al., 2010) developed to predict berm and dune erosion. The following chapters describe the experiment setup, instrumentation, collected data, and analysis procedures. Furthermore, the essential parts of the numerical model CSHORE are explained before comparisons between the data and CSHORE are presented to show the capability and difficulty in capturing the essential hydrodynamic and morphological processes responsible for ridge-runnel migration.

Additionally, the modified CSHORE is compared with profile changes in previous laboratory experiments and in the field. These profiles exhibit various degrees of overwash and erosion and some include ridge-runnel features. The comparisons indicate the applicability of the latest CSHORE with only one empirical parameter to be calibrated. Finally, the experimental and numerical results are summarized and conclusions are presented.

Chapter 2

RIDGE-RUNNEL EXPERIMENT

In this chapter the experimental setup for two ridge-runnel tests conducted in the “Sand Tank” of the University of Delaware is presented. The devices for measuring hydrodynamics, morphological changes and sediment transport are explained briefly. For a more detailed explanation refer to Figlus et al. (2009) who conducted a dune overwash experiment in this sand tank.

Ridge-runnel migration is thought to play a significant role in beach recovery after a storm. Often, ridge-runnel systems are present at the beach after storm tides recede. This situation is taken as the starting point of the experiment. The formation of a ridge-runnel system is not investigated in this study. Ridge-runnel migration is a result of complicated interlinked hydrodynamic and sediment transport processes. Wave-induced overtopping of the ridge crest transports water and sand into the runnel, fills it up and causes apparent onshore migration. The return flow out of the runnel may occur back over the ridge (2D scenario) or through channels interrupting the ridge crest at various intervals (3D scenario). These two return flow configurations are investigated in this experiment since they have a major effect on the ridge-runnel migration.

2.1 Experimental Setup

Two different initial ridge-runnel profiles (HR and LR) were constructed with fine sand ($d_{50} = 0.18\text{ mm}$) in a 23 m long and 1.15 m wide flume section of the University of Delaware Sand Tank before being exposed to identical wave conditions

generated by a piston-type wave maker. Figure 2.1 shows a schematic side view of the flume section. The displayed sand bottom profile corresponds to the initial setup for the LR test. A dividing wall along the center line of the tank separates the flume section from the rest of the tank. This setup minimizes seiching and limits the amount of sand required for the experiment. Approximately ten tons of sand have been placed on top of a 1/30 rigid plywood slope. The flume section includes a state-of-the-art laser profiling system (Section 2.3) and a water collection basin with a sediment trap (Section 2.4). Eight capacitance wave gauges and three acoustic Doppler velocimeters provide hydrodynamic measurements (Section 2.2).

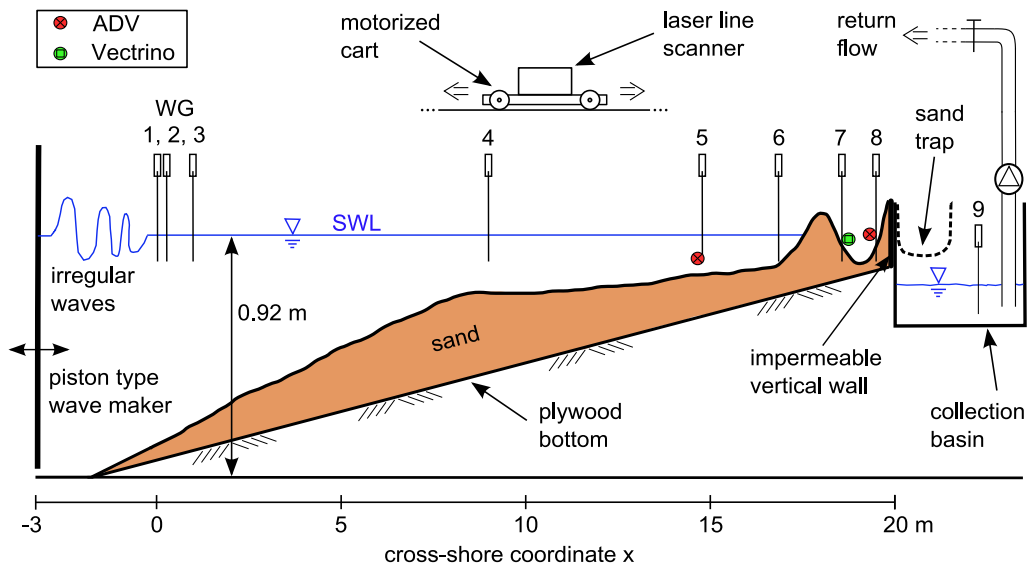


Figure 2.1: Schematic side view of the ridge-runnel experiment setup for the LR test including wave paddle, beach profile on top of plywood slope, collection basin with sediment trap, water recirculation system and measurement instrument locations.

The HR (High Ridge) and LR (Low Ridge) tests had similar initial profiles and were subject to identical wave forcing conditions under controlled laboratory conditions. The main difference was the water and sediment transport out of the runnel at its landward end. To mimic the 3D ridge-runnel scenario, water and sediment were allowed to exit the system through wave overtopping and overwash

over a low-crested impermeable wall behind the runnel. In this HR test the initial ridge crest exceeded the wall crest by 4 cm and the offshore water depth in front of the wave maker was 100 cm . During a test run overwash sediment and water were carried over the crest of the impermeable vertical wall, through a sand trap constructed of a lightweight aluminum frame and a polyester fabric mesh with a micron rating of 74 retaining overwash sediment larger than silt. Details on the overwash collection system are given in Section 2.4. For the 2D case, the same initial ridge-runnel setup was lowered by 8 cm (including the water level). In this LR test water and sediment could only exit the runnel as return flow over the ridge. The focus of the experiment was on wave-induced ridge-runnel migration where the still water level (SWL) in front of the ridge was constant throughout each test.

A right-hand Cartesian coordinate system is used throughout. Its origin coincides with the still water level (SWL) at the location of offshore wave gauge 1 (WG1) and its x-axis points onshore along the center line of the flume section. The z-axis is positive upward. Most measurement instruments used in the experiment were mounted on metal frame carts movable in cross-shore direction along a set of T-tracks (Figure 2.2). A laser line-scanner was mounted on a motorized cart for high-resolution 3D profile scans of the subaerial portion of the profile where the SWL was lowered and the runnel was drained for the laser scanning. A rotating mirror assembly allows for longshore sweeps of the bottom profile by the laser beam. The cross-shore position of the cart is determined by a stationary laser range finder shooting its beam at a target on the cart. The underwater portion of the profile is scanned acoustically using three ultrasonic thickness transducers along three transects.

2.1.1 Sediment Characteristics

The sediment used in the experiment is considered poorly graded (well sorted) fine sand of light brown color. Grain shapes are subangular to subrounded and

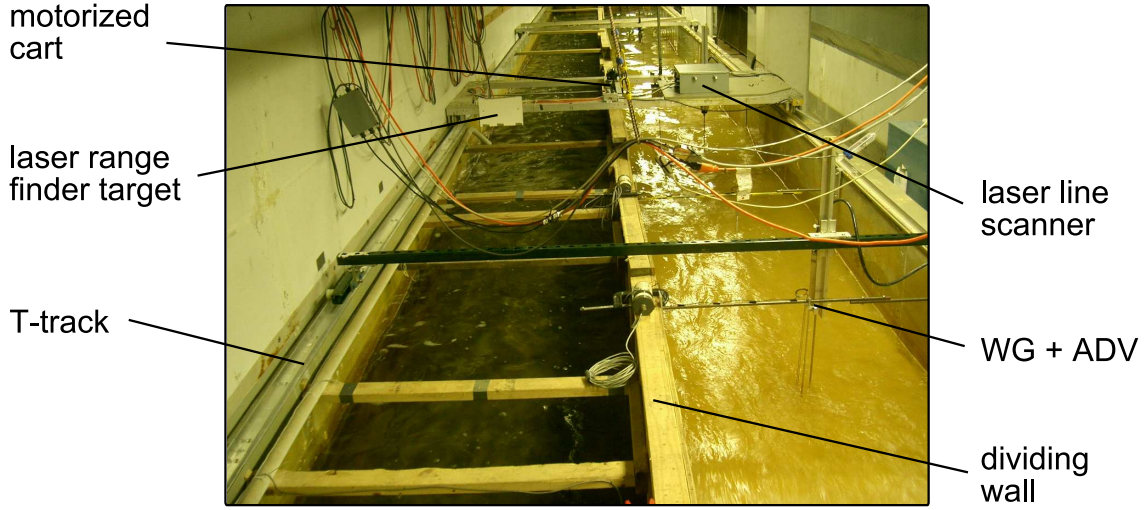


Figure 2.2: Picture of wave flume setup facing offshore.

the Unified Soil Classification System (USCS) label for this sand is SP. The grain size distribution obtained from a sieve analysis of several sand samples yields the characteristic sediment diameters used in the subsequent data analysis (see Figure 2.3). In order to get a better representation of the actual sediment diameters retained in each sieve, geometric mean values of sieve openings between adjacent sieves are used. The uniformity coefficient, C_u , and the coefficient of curvature, C_c , of the sediment (e.g. Holtz and Kovacs, 1981) are calculated from the size distribution curve as

$$C_u = \frac{d_{60}}{d_{10}} = 1.7 \quad ; \quad C_c = \frac{(d_{30})^2}{d_{60} \times d_{10}} = 0.9 \quad (2.1)$$

where indices of the characteristic diameters used above indicate percent finer by weight.

The sand's specific gravity s is the ratio of its density ρ_s to fresh water density ρ ($s = \rho_s/\rho$). The measured values of specific gravity, porosity, n_p , and average fall velocity, w_f are listed in Table 2.1 along with other parameters describing the sediment characteristics.

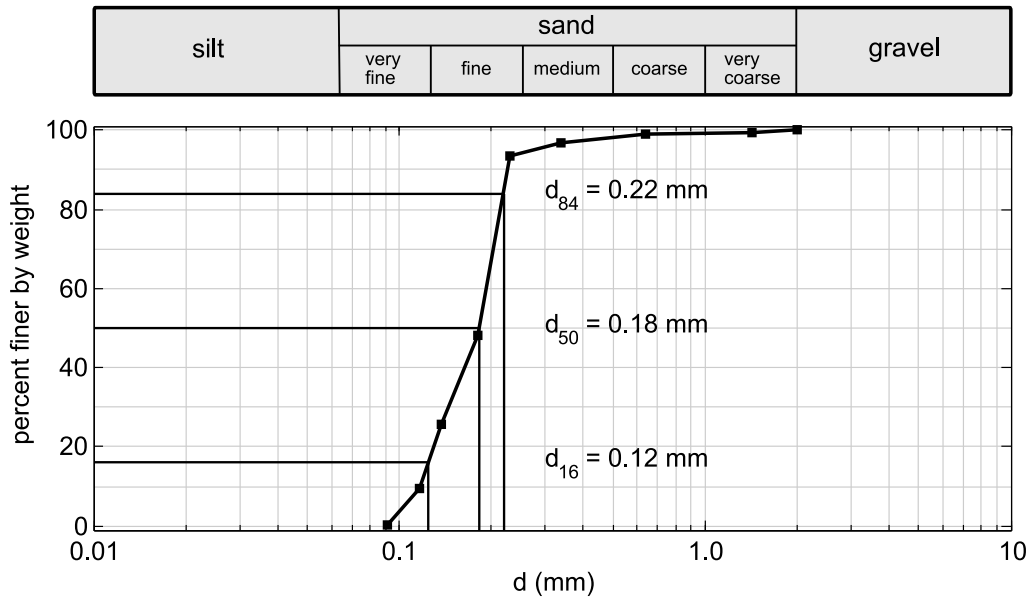


Figure 2.3: The sieve analysis of the sediment used in the experiment shows a well sorted grain size distribution of mainly fine sand. The data points are geometric mean diameters corresponding to adjacent sieve sizes.

Table 2.1: Sediment characteristics.

| | |
|--------------------------|------------------------------|
| USCS label | SP (poorly graded sand) |
| color | light brown |
| grain shape | subangular to subrounded |
| d_{16}, d_{50}, d_{84} | 0.124 mm, 0.183 mm, 0.221 mm |
| d_{10}, d_{30}, d_{60} | 0.117 mm, 0.146 mm, 0.194 mm |
| C_u, C_c | 1.7, 0.9 |
| s, n_p, w_f | 2.6, 0.4, 2.0 cm/s |

2.1.2 Test Procedure

After the initial ridge-runnel profile was constructed and scanned, the water depth in the flume was raised to the specified SWL followed by the calibration of all the instruments. For the initial run of HR and LR, the runnel water level (RWL) was the same as SWL. For all proceeding runs, the runnel was drained for the laser scanning and filled back up to restore the RWL. Each run consisted of an irregular wave train of 400-s duration with a TMA spectral shape created by the wave maker (the spectral significant wave height $H_{mo} = 18\text{ cm}$, and the spectral peak period $T_p = 2.6\text{ s}$). During the run, free surface elevation and water velocities were measured at specified locations throughout the flume.

The waves shoaled, broke, formed a surf zone, created uprush on the seaward ridge face, and overtopped the ridge crest to fill the runnel. The water and sand carried over the crest of the impermeable vertical wall at the landward end of the runnel was collected in the designated sand trap and collection basin. Cumulative water and sand overwash were measured in each run of the HR test. Profile scans were performed between runs and required drainage of a certain amount of water to increase the subaerial portion of the profile for the laser scanning. That included the water present inside the runnel. The test series ended after the ridge-runnel system had completely disappeared. The HR test required 10 runs (4000 s) and the LR test lasted 35 runs (14,000 s).

The profile changes during the HR test were more rapid than during the LR tests. Hence, HR profiles were scanned more frequently (Section 2.3). Laser scans had a cross-shore range from $x = 6\text{ m}$ all the way to the vertical wall landward of the runnel. Acoustic scans covered the rest of the offshore profile where only minor changes occurred. After each scan the SWL and RWL were adjusted to their required levels for the next run.

2.2 Wave Generation and Measurement

Waves were created by the paddle of the piston-type wave maker located at the offshore end of the flume. The water depth at the wave maker was 1.00 m for the HR test and 0.92 m for LR. The input signal to the wave actuator consisted of a time series of 8000 voltage values for the duration of 400 s corresponding to a certain paddle displacement aiming to reproduce an irregular wave train with a TMA spectral shape. A National Instruments 16 channel SCSI data acquisition board controlled by a LabView user interface handled data logging and wave maker control simultaneously. The data from all instruments was recorded at 20 Hz .

2.2.1 Wave Gauges

Free-surface elevation in the flume was measured by 8 capacitance wave gauges (WG1-WG8) located along the center line in the wave flume section of 1.15 m width (Table 2.2). Capacitance wave gauges include a vertical electrical wire loop connected to a circuit board which employs two frequency oscillators to determine the capacitance in the wire over a set range. As the waves pass the half-submerged wire, the capacitance registered by the circuit board changes proportionally to the depth of the wire submerged in water. The conversion to water free-surface elevation η follows a linear relationship with measurement errors of $\pm 1\text{ mm}$.

Offshore wave conditions and run repeatability were checked by WG1 through WG3, where three gauges are necessary to separate incident and reflected wave signals following Kobayashi et al. (1990). The chosen spacing between the three gauges yields a resolvable frequency range of $0.15 - 1.70\text{ Hz}$ for this procedure which covers the entire range of relevant frequencies in this experiment. WG1-WG6 were located seaward of the ridge-runnel system and were always submerged under water. WG7 and WG8 were particularly important since they were located in the region of ridge-runnel migration with significant profile changes and intermittent wet and dry periods. They were initially located inside the runnel with their wires extending

into the sand bottom. At this location they measured free-surface elevation consisting of wave oscillations, RWL changes, and bottom profile evolution. These three components of the WG record are separated as explained later in Section 3.2.4.

Table 2.2: Wave gauge locations (WG1-WG8) for HR and LR tests.

| | WG1 | WG2 | WG3 | WG4 | WG5 | WG6 | WG7 | WG8 |
|---------|------|------|------|------|-------|-------|-------|-------|
| x (m) | 0.00 | 0.25 | 0.95 | 8.27 | 14.90 | 16.97 | 18.52 | 19.46 |
| y (m) | 0.00 | 0.00 | 0.00 | 0.00 | 0.00 | 0.00 | 0.00 | 0.00 |

$y = 0$ along the flume center line

Wave gauges located in the wet zone (WG1-WG6) were calibrated at the beginning of each test day to minimize errors (Figlus et al., 2009). WG7-WG8 were calibrated before and after each test with only minimal deviation. Results are presented in Section 3.2.

2.2.2 Acoustic Doppler Velocimeters

The instruments used for velocity measurements were mostly operated under unfavorable conditions. The nature of this experiment yielded rapid profile changes accompanied by very small water depths on the ridge crest during wave overtopping events. Two Sontek acoustic Doppler velocimeters (ADV) with a sampling rate of 20 Hz and an additional Nortek Vectrino with a sampling rate of 200 Hz for the LR test recorded flow velocities in front and on top of the ridge and in the runnel. Velocity measurements were always taken next to existing wave gauges. The coordinates of the respective sampling volumes are given in Table 2.3. The vertical coordinate depends on the local bottom elevation and varied from run to run.

ADV1 at the WG5 cross-shore location is a 3D instrument with downward pointing probe tips measuring velocities in the cross-shore (u), alongshore (v), and

Table 2.3: ADV measurement volume locations for HR and LR tests.

| | ADV1 (3D) | Vectrino (LR only) | ADV2 (2D) |
|---------|-----------|---------------------|-------------------|
| x (m) | 14.90 | 18.52 | 19.46 |
| y (m) | 0.15 | 0.15 | 0.15 |
| z (m) | $-2d/3$ | mostly $z_b + 0.01$ | varies with d_r |

d = local water depth at the start of each run

z_b = local bottom elevation at the start of each run

d_r = local water depth inside the runnel at the start of each run

vertical (w) directions in a sampling volume 5 cm below the probe tips. ADV2 at the WG8 location is a 2D instrument with sideways pointing probe tips which allows for measurement of the two velocity components u and v at the location of the sampling volume. The Vectrino (LR test only) is a side-looking 3D instrument and was used specifically for velocity measurements in the vicinity of the migrating ridge crest.

The principle of operation is the same for all three instruments. An acoustic pulse is emitted from the transmitter and reflected by suspended particles in the passing water. The signal picked up by the receiving probe tips is Doppler shifted due to the motion of the water past the probe which allows for calculation of the fluid velocity through correlation. Since fine sand is suspended during each wave run the ADVs give strong signal-to-noise ratios with error estimates of ± 0.5 cm/s while submerged in water.

In Figure 2.4 the WG and ADV placements for the HR and LR tests are shown for the region of major profile change ($x = 14.0$ to 19.9 m). The ridge-runnel evolution is visualized by three profiles measured during the HR (top panel) and LR (bottom panel) tests. These major profile changes required adjustment of the vertical position of the velocity measuring volumes (circles) in order to capture flow

velocities in very small water depths. The actual vertical coordinates z_{ADV} for ADV2 and Vectrino are given in the data analysis section (Tables 3.16, 3.17, and 3.18). They were chosen using profile measurements from extensive preliminary testing (Gralher, 2010). Before each run the instruments were placed so that a clearance of approximately 1 cm from the expected profile after the run would remain. This prevented instrument burial during a run and increased the duration of instrument submergence without interference with the bottom boundary. Despite the careful placement, extensive filtering was required for the Vectrino data to eliminate outliers (see Section 3.3.3). Statistical velocity parameters computed from the measured time series are presented in Section 3.3.

2.3 Profiling

The bottom morphology in the experiment changed rapidly over the course of a test due to the intense wave action. In order to keep track of the rapid ridge-runnel evolution, it is crucial to obtain measurements of profile changes at high spatial and temporal resolution with a high level of accuracy. Two different measurement systems were employed to record bottom elevation changes. The subaerial portion of the beach profile was measured by a laser line scanner and the submerged portion was measured using ultrasonic thickness gauges.

2.3.1 Laser Line Scanner

Bottom elevation changes were most prominent in the zone encompassing the ridge and runnel. Scanning this area of rapid profile change using laser technology has many advantages including the possibility for automation and direct data logging as well as its accuracy and speedy measurements.

A class III Acuity AR4000-LIR laser line scanner system (Figure 2.5) in conjunction with a class II Acuity AR1000 laser distance finder delivered high-resolution 3D scans of the subaerial portion of the bed profile. Both lasers obtain

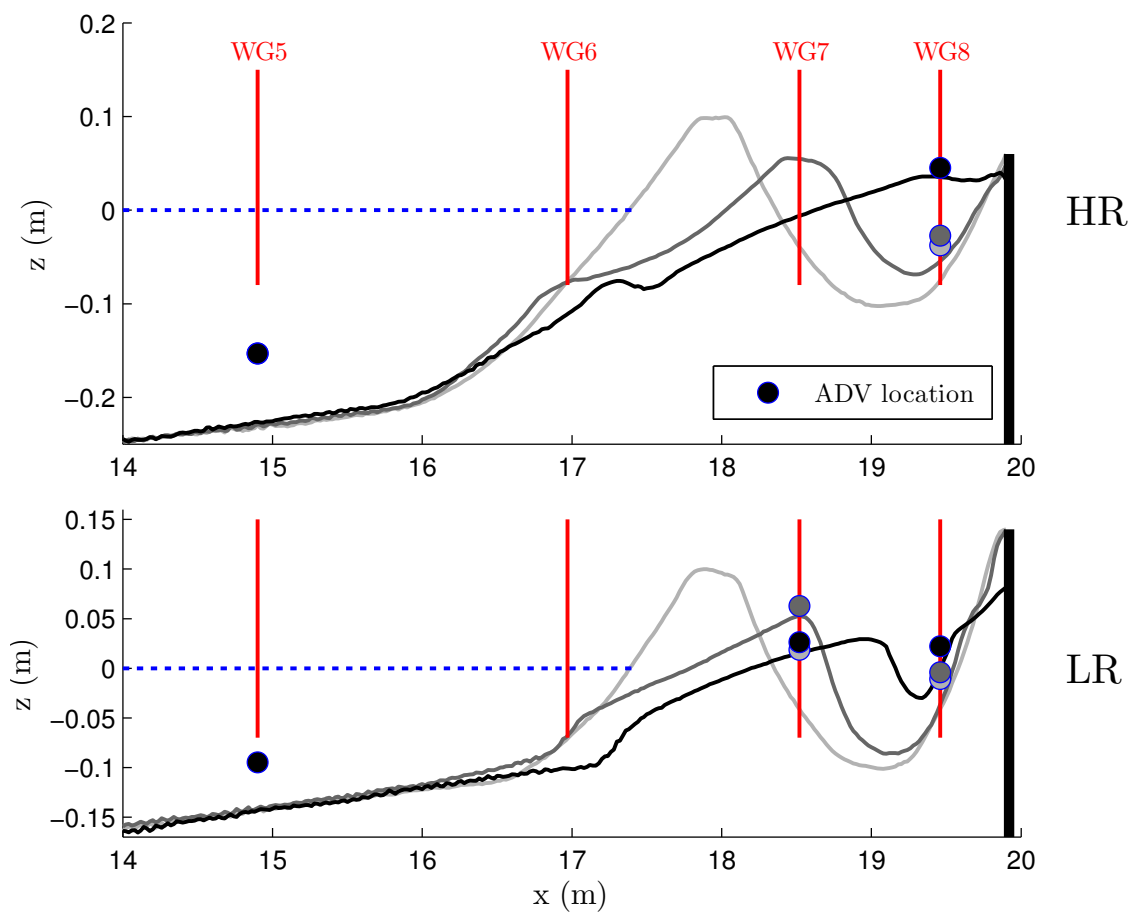


Figure 2.4: WG and ADV placement during HR (top) and LR (bottom) tests. Cross-shore locations of WGs (red vertical lines) and ADVs (circles) remained fixed. The vertical position of the ADV measuring volumes varied with bottom profile elevation.

distance measurements via a time-of-flight measurement of the emitted laser beam as it reflects off of a target. The main components of the AR4000 line scanner system are the horizontally mounted 780 nm IR laser diode with an optical power output of 8 mW and a rotating mirror assembly which deflects the outgoing and reflected laser beam by 90° to allow for a 2D scan of the vertical (y - z) plane during a full 360° sweep of the mirror around its horizontal axis.



Figure 2.5: The AR4000 laser line scanner system is mounted inside an enclosure case on a motorized cart and includes a rotating mirror to deflect the laser beam for 360° scans. Only distance samples collected within the field of view limited by the enclosure scanning window are processed.

Performance and measurement accuracy depend on a variety of factors like distance from the target, amplitude of the return signal (reflectivity of the target), and three types of noise including detector thermal noise, laser diode noise, and noise related to the chosen sampling resolution. The line scanner has a maximum range of 9 m but is configured with a close focus optics option which yields the greatest measurement sensitivity around 1 m from the sensor, consistent with the required range of $0.5 - 1.5\text{ m}$ in the experiment.

Fine sand has good diffuse reflective properties which leads to high return signal amplitudes in the detection photo diode. This ensures very accurate readings

but the three types of noise that can affect the standard deviation of the return signal vary depending on the sampling rate. The AR4000 line scanner is connected to a PC via a high speed interface card capable of sampling distance measurements at a rate of 50,000 Hz . For the present application the sampling rate was set to 10,000 Hz which yields a root-mean-square noise value of approximately 1.5 mm mainly related to drift and fluctuation of the emitted laser beam (laser diode noise). For more information on operation and performance of the AR4000-LIR line scanner consult the user's manual (Acuity, 2003b) which is available online (www.acuityresearch.com).

In order to create 3D images of the surface scanned by the ($y - z$) line scanner, the line scanner system was mounted on a motorized cart moving along the flume's x-axis on a set of T-tracks. Care was taken to arrange the line scanner in such a way that the axes of mirror rotation and emitted laser beam coincide with the centerline (x-axis) of the flume so that one sweep of the mirror yields distance measurements of an alongshore slice of the flume topography. This was accomplished by calibrating the line scanner position through repeated scans of a custom made aluminum frame with an adjustable horizontal longshore bar and vertical walls with exact right angles.

In an effort to limit the amount of data collected during scanning, the field of view is limited mechanically by an enclosure case and electronically through software to 60° on either side of the vertical (z-axis) facing downward from the cart into the flume which is sufficient to digitize the entire width of the sandy bottom topography.

The cart is equipped with a servo motor and control unit capable of moving the line scanner back and forth in the cross-shore direction with continuously adjustable speeds up to 10 cm/s . The x-coordinate of the 2D slice scanned by the line scanner at any point along the flume is provided by the AR1000 distance sensor. This laser range finder emits a horizontal beam of visible red light (650 nm) with

optical power output of 1 mW . It measures the distance from its fixed position next to the collection basin to the moving cart. A portion of the light scattered from a reflective target mounted on the motorized cart is collected and focused on a photo detector inside the AR1000 to calculate the distance of the target from the fixed position of the range finder via the time-of-flight method. Since a reflective target is used, the AR1000 can measure distances of up to 150 m with an accuracy of $\pm 2\text{ mm}$ (Acuity, 2003a). Figure 2.6 shows a top view schematic of the described arrangement.

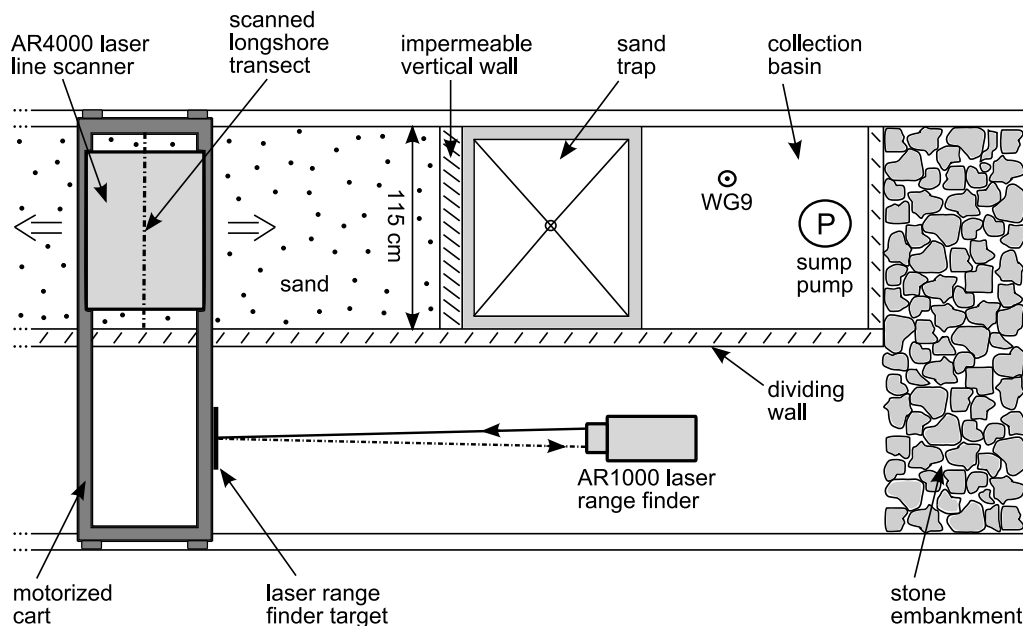


Figure 2.6: Schematic top view of experimental setup. The fixed AR1000 laser range finder gives the x-location of the motorized cart traveling along the flume at constant speed while the AR4000 laser line scanner measures longshore transects of the bottom profile at specified increments.

During a scan the cart is moving at a constant speed of 1 cm/s while the line scanner does sweeps of alongshore slices in a fraction of a second at set cross-shore increments controlled by the AR1000 distance sensor. The scanned alongshore slices are practically perpendicular to the x-axis since the slow motion of the cart during an entire 360° sweep of the line scanner is negligible compared to the high speed

rotation of the mirror. For this experiment the line scanner has been configured to collect 500 data points per alongshore slice at a sampling frequency of 10,000 Hz which corresponds to a measurement time of 0.05 s per slice. The rotation speed of the mirror is set to allow for 3 revolutions during that time. Alongshore slices are measured every 2 cm over a length of 14 m in this experiment which leads to an overall time of 20 minutes required for one complete scan.

Data from the line scanner and distance finder are collected through the high speed interface card and the RS232 serial connection, respectively, and streamed to custom programmed LabView software which accesses software libraries specifically written to control the AR4000 line scanner system (Dunnum, 2006).

Only the subaerial portion of the profile can be scanned by the line scanner system since the laser distance measurements are calibrated for time-of-flight in air. However, since the scan is automated, accurate and requires only little time, the subaerial portion is increased to stretch over a cross-shore distance of 14 m ($x = 6 - 20 m$) by lowering the water level in the tank to the desired level after each run. The limit of $x = 6 m$ is located well seaward of WG4 positioned at $x = 8.27 m$ as listed in Table 2.2.

2.3.2 Ultrasonic Thickness Gauges

The offshore portion of the profile ($x = 0 - 7 m$) including 1 m of overlap with the laser scan is measured using three submerged 1 MHz ultrasonic transducers connected to a Panametrics 25MX precision thickness gauge via an MX-8 multiplexer. The transducers measure the time for acoustic signals to be reflected from the sandy bottom and convert it to the water depth at this specific location. They are mounted 30 cm apart in an alongshore array on a specialized vernier caliper extending downward into the water from a movable cart. As the cart is moved from one cross-shore location to the next along the flume the transducers take depth readings at their respective alongshore locations yielding three individual cross-shore profile lines at

$y = 30\text{ cm}$, $y = 0\text{ cm}$, and $y = -30\text{ cm}$. A representative 2D offshore profile is then obtained by averaging the three transects.

The transducers give depth readings to millimeter precision up to their operational limit of 10 cm from the reflective bottom boundary. The vernier caliper is adjusted before each scan to stay within this operational range. Hence, the measurement accuracy of the acoustic profiling method is mainly dependent on the vernier caliper precision and is assumed to be on the order of 5 mm . Collected data is logged by the 25MX thickness gauge and later transferred to a PC for further processing. The time requirement to scan the offshore portion of the profile is approximately 30 minutes.

Laser and acoustic scans together yield the profile evolution for the entire flume section. A total of 11 laser scans (before and after each run) and 3 acoustic scans (initial, middle of the test, final) were performed for the 10 runs of the HR test. The LR test was completed in 35 runs with 12 laser scans and 6 acoustic scans. Scans were not required after each run during LR since the ridge-runnel evolution was much slower. The profiles corresponding to runs with no scan were interpolated linearly. An overview of the run numbers of scanned profiles is given in Table 2.4 where the integer zero implies the initial profile of each test.

Table 2.4: Run numbers of laser and acoustic profile scans performed for HR and LR.

| | HR | LR |
|----------|----------|----------------------------------|
| Laser | 0, 1-10 | 0, 1-4, 6, 9, 13, 17, 23, 29, 35 |
| Acoustic | 0, 5, 10 | 0, 9, 17, 23, 29, 35 |

0 = initial scan

2.4 Overwash Collection

The HR test included wave overtopping and sediment overwash over the vertical wall at the landward end of the runnel. The flow over the vertical wall mimicked the effect of 3D flow out of natural runnels through rip channels. In order to determine the transport rates of water and sediment exiting the runnel over the vertical wall, a special experimental setup was required to collect, separate and measure the volume of overtopping water and overwash sediment. A custom-built water collection basin behind the vertical wall housed a horizontal sand trap to separate the overwash sediment from the overtopping water (Figure 2.7).

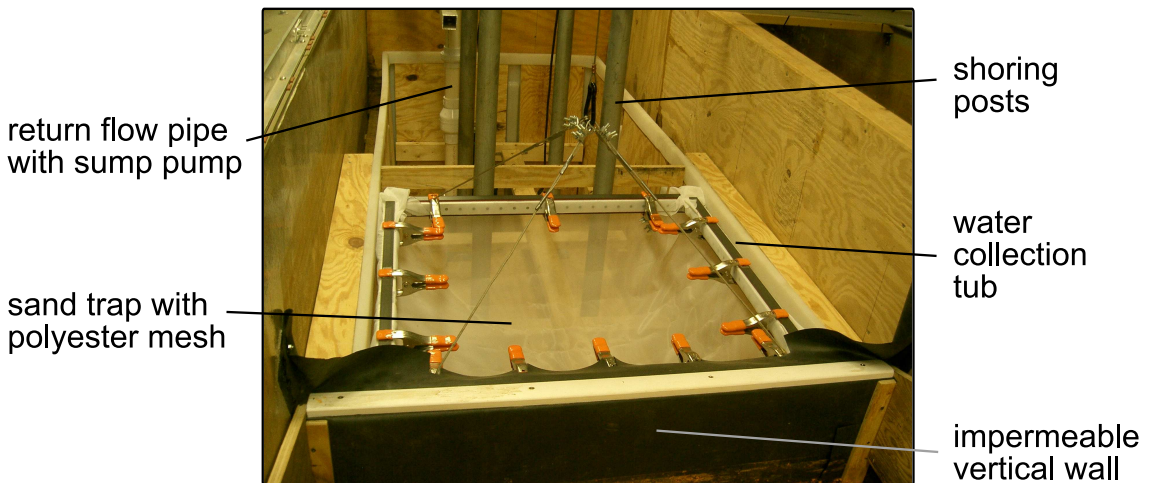


Figure 2.7: Sand trap and water collection basin setup.

2.4.1 Water Collection Basin

The rectangular water collection basin located behind the wall had a capacity of 500 gallons (1900 liters) with dimensions of $2.44\text{ m} \times 0.97\text{ m} \times 0.78\text{ m}$ (*length* \times *width* \times *height*). To prevent leakage of the basin, a one piece seamless polyethylene construction was chosen and scaffolding in combination with plywood panels on the inside walls was used to preserve the tub's shape against deformation from the hydrostatic water pressure during a run. The rim of the basin reached up to the crest

of the impermeable vertical wall at the landward end of the ridge-runnel profile. The wall crest elevation was $z = 6\text{ cm}$ above SWL for HR and $z = 14\text{ cm}$ above SWL for LR. The difference of 8 cm was enough to prevent waves from overtopping the wall during the LR test.

The water level inside the collection basin was measured by two independent systems for redundancy. Both a mechanical float gauge and an electronic capacitance wave gauge (WG9) indicated the location of the water surface within $\pm 1\text{ mm}$ accuracy. Calibration of the instruments, conversion to collected water volume, and error estimates were discussed in Figlus et al. (2009).

A recirculation system ensured a constant ($\pm 1\text{ mm}$) water level in the wave tank during each run by pumping excess water out of the collection basin. The recirculation system consisted of a Zoeller E284 sump pump, a Bürkert 8035 inline paddle wheel flow meter, a ball valve and two check valves connected by schedule 40 2-inch PVC pipes. Pump operating cycles were controlled by a float switch between maximum and minimum water levels in the collection basin. As soon as the water level exceeded the maximum level, pumping commenced until the water level dropped to the minimum level. The total volume of water flowing over the vertical wall in Figure 2.7 during a run is the sum of the volume collected in the collection basin, the volume pumped out during the run, and the volume contained in the wet sand caught in the trap.

2.4.2 Sand Trap

A mixture of sediment and water was carried over the crest of the impermeable vertical wall in each HR run. In order to separate the overwash sediment from the water a horizontal sand trap was lowered into the front third of the collection basin with a tight fit. A rubber lip made from flexible pond liner material directed the water and sediment mixture into the trap. The trap itself was made up of a polyester fabric mesh secured to a lightweight aluminum frame by retaining clamps

which allowed for easy replacement of the fabric if necessary. Suspended from a slewing crane, the sand trap was easily moved in and out of the collection basin for sand removal or repairs.

The polyester fabric mesh had a micron rating of 74 which means that particles with a diameter exceeding 0.074 mm were retained. Hence, particles considered to be fine sand or larger were collected in the sediment trap whereas particles considered to be silt or clay passed the mesh together with the overtopped water. Results from sieve analyses of the sediment used in the experiment indicate that 2% of the sediment might not be retained by the polyester mesh.

After each 400-s test run the trap remained in place for approximately 15 minutes to allow most of the excess water contained in the wet overwash sand to drain into the collection basin. The retained wet sand was then removed and weighed before and after oven drying for at least 12 hours to determine its dry weight and the weight of the contained water.

Chapter 3

RIDGE-RUNNEL DATA ANALYSIS

In this chapter the data collected during the ridge-runnel experiment is presented. Results include morphological evolution and overwash measurements as well as wave gauge and velocity data. Several preliminary tests were conducted to determine the instrument locations. The preliminary test results are consistent with those presented in the following.

3.1 Morphology and Overwash

The evaluation of the measured morphological changes and overwash quantities plays an integral part in understanding the complex mechanisms involved in ridge-runnel evolution. Broken waves running up and down the seaward ridge slope eroded sediment, suspended sediment, and modified the ridge shape. Sediment was either carried over the ridge crest into the runnel by overtopping waves or transported offshore by backwash and undertow current. Once water and sediment entered the runnel, several processes occurred. The runnel filled up with water and acted as a settling basin for the overwash sediment. As the runnel water level (RWL) increased due to continued wave overtopping, there were two ways for water to exit the runnel: Either by means of an offshore return flow over the ridge crest or as overwash flow over the vertical wall into the collection basin. The main difference between the HR and LR tests was that for the LR test water exited the filled runnel as offshore return flow only. Most of the sediment transported into the runnel was observed to settle in the runnel because the offshore return flow accompanied

little wave action and the ponded water reduced the sediment concentration in the overwash flow for the HR test.

Figure 3.1 shows 3D laser scans at various time levels with time $t = 0$ for the initial profile during the HR and LR tests to give a visual impression of the collected profile evolution data in the zone of major profile changes.

3.1.1 Ridge-Runnel Migration

For the analysis of the sand bottom evolution, profile scans obtained from the laser line scanner system and the three acoustic sensors were reduced to 2D (x and z) coordinates using the alongshore average of the measured data across the 115 cm wide flume. The x-axis is set along the flume center line and has its origin at the location of WG1 with the vertical coordinate z positive upward above SWL.

Ridge-runnel migration in this experiment was onshore for both tests. However, HR and LR tests showed significant differences in ridge migration speed and profile adjustment due to the inherently different hydrodynamic forcing. Figure 3.2, depicts the evolution of the measured HR (top) and LR (bottom) ridge-runnel profiles in the region of major profile changes ($x = 15.5 - 19.9\text{ m}$). A green to red color map is used to show the time dependent progression of the profile change from the initial to the final scan. The time interval between each plotted profile is 400 s.

The initial ridge crest was located 10 cm above SWL for both tests as shown in Figure 1.3 where the runnel water level (RWL) was the same as SWL. The runnel was filled with water during the first half of the first 400-s run of each test. During this initial ponding period, crest lowering and onshore ridge migration were at a maximum for both HR and LR tests because water ponding promoted the settlement of sediment in the runnel. Throughout the experiment, the ridge crest elevation was never lowered below SWL. Once the runnel was filled, the morphological evolution for HR and LR started to differ significantly due to the different boundary conditions at the landward end of the runnel.

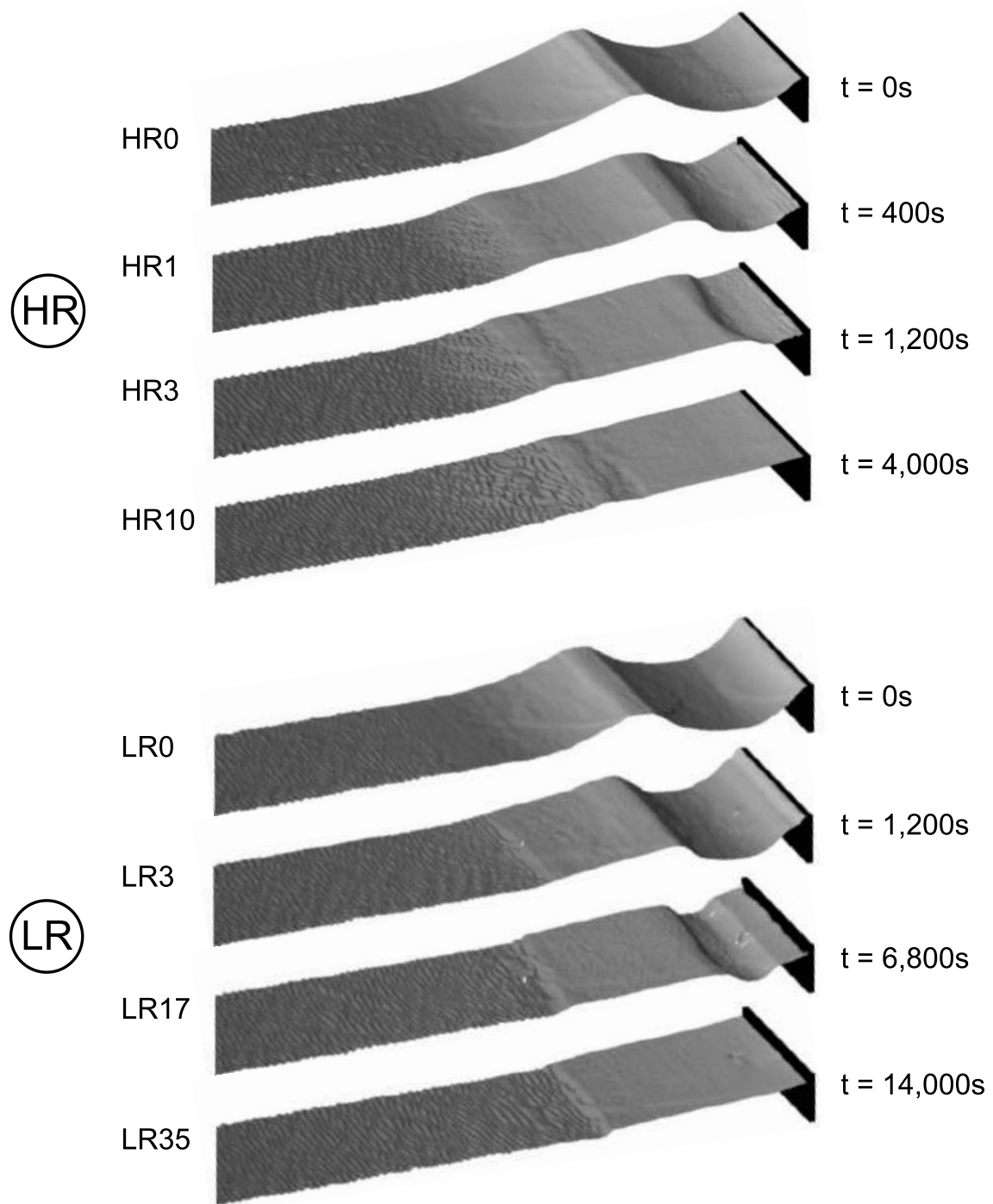


Figure 3.1: 3D profile scans for HR and LR.

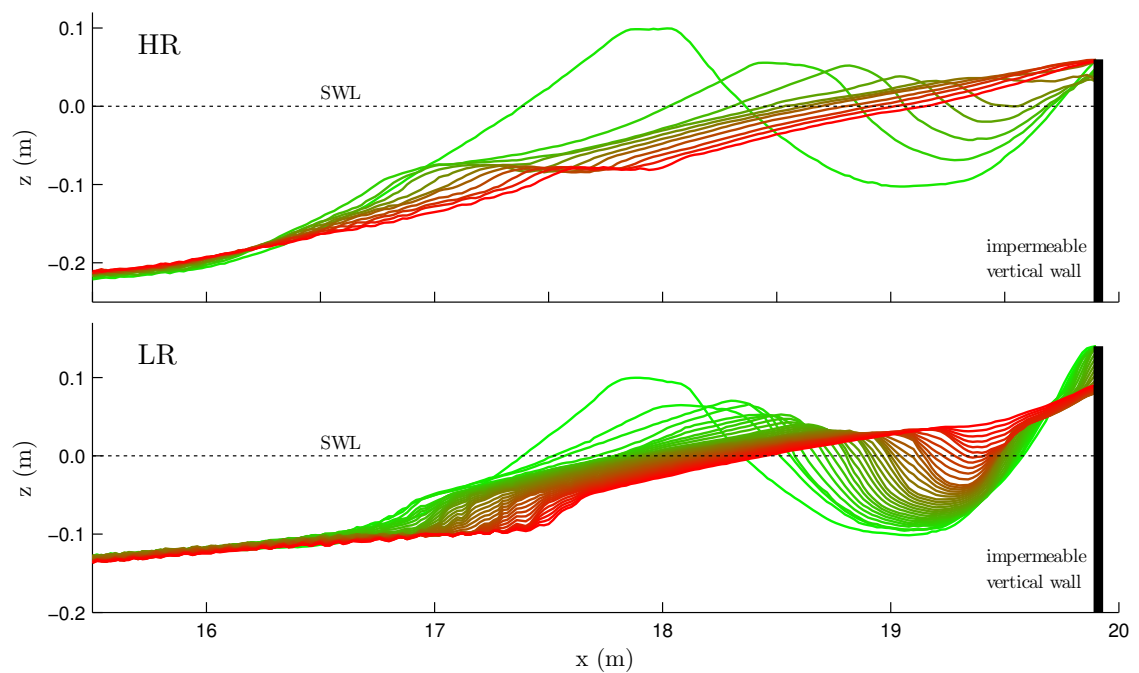


Figure 3.2: Ridge-runnel evolution in the zone of major profile changes measured for HR and LR. A color map from green (initial) to red (final) indicates the profile changes over time

The lowered ridge crest in the HR test migrated onshore at a rate of approximately $3\text{ cm}/\text{min}$. The crest elevation stayed fairly constant at the level of the wall crest. A terrace was also formed around $z = -0.1\text{ m}$ and the terrace migrated onshore at a rate of approximately $1\text{ cm}/\text{min}$. As the ridge crest and runnel trough migrated landward, the distance between them decreased steadily while the ridge-runnel feature maintained its relative shape. After run HR6 the ridge and runnel merged into a $1/14$ beach slope. The integer after HR or LR indicates the run number corresponding to the number of 400-s bursts. A quantitative assessment of ridge and runnel geometry is presented in Section 3.1.3.

Figure 3.2 indicates a much slower ridge-runnel onshore migration for LR because of no water and sediment transport over the vertical wall crest. Wave overtopping of the wall reduces seaward return flow and suspended sediment transport as explained in Section 4.1. Instead of a terrace, a step formed at the toe of the seaward ridge slope which decreased gradually to a final slope of $1/15$. The slope developing between the ridge crest and runnel trough was much steeper (up to $1/5$ in run LR17).

The HR test was stopped after ten 400-s runs (4,000 s total) and the LR test was terminated after 35 runs (14,000 s total). At the end of both test series the ridge-runnel feature was completely smoothed out. An equilibrium beach state was not reached for HR since wave overtopping and overwash over the vertical wall crest would continue to reduce the amount of sediment in front of the wall. The final LR profile, however, was in a state of equilibrium since changes in the last several runs were negligible. It needs to be stated that the present experiment focused on ridge-runnel migration due to wave overtopping and overwash under constant water level in order to isolate the wave effect on the migration patterns.

Separating the profile evolution of both ridge-runnel tests into different phases allows us to present the migration process in a more concise manner. We chose three

distinct phases of ridge-runnel evolution based on the measured profile shapes.

Phase 1: The seaward ridge slope adjusts to the forcing conditions by forming a concave beach profile. Waves overtopping the ridge crest fill up the runnel, lower the crest elevation significantly, and transport a relatively large amount of sediment into the runnel, leading to rapid onshore ridge migration. Offshore flow over the ridge is initiated after the runnel is filled up.

Phase 2: Onshore migration and progressive reduction of the ridge-runnel cross-sectional area. The rate of the ridge-runnel profile evolution is influenced by the wave-induced water flow into and out of the runnel. The runnel is always filled with water.

Phase 3: Profile evolution of a sloping beach in front of the wall after the ridge-runnel system is completely smoothed out.

Table 3.1 lists the run numbers and durations for each phase in addition to a brief verbal description of the dominant morphological processes. Figure 3.3 depicts the 4 measured profiles separating the 3 evolution phases described in Table 3.1 for each test. The apparent differences between HR (top) and LR (bottom) include the larger profile change for HR during Phase 1 and the more rapid ridge-runnel elimination during Phase 2. In addition, the continued erosion and onshore movement of the beach during Phase 3 in the HR test due to wave-induced overwash contrasts with the almost equilibrium behavior of the LR beach for no overwash.

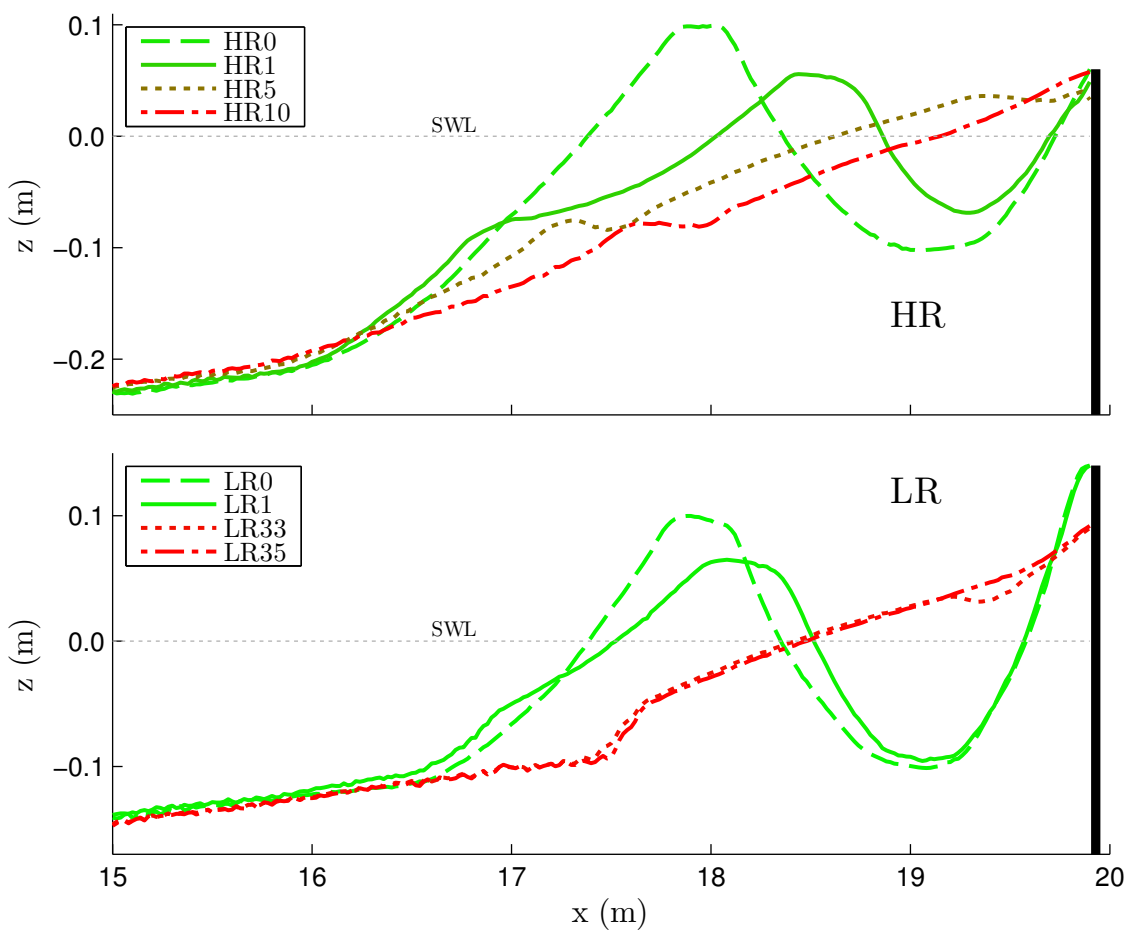


Figure 3.3: Measured HR and LR profiles separating three evolution phases.

Table 3.1: Phases of profile evolution for HR and LR tests.

| Phase | Description | HR | LR |
|-------|---|-----------------------------|----------------------------------|
| 1 | Initial ridge crest lowering and runnel trough filling. Relatively rapid onshore migration. Formation of concave seaward ridge profile in response to wave forcing. | HR1 (0 – 400 s) | LR1 (0 – 400 s) |
| 2 | Progressive reduction of ridge-runnel cross-sectional area during landward migration up to complete disappearance. | HR2–HR5 (400 – 2,000 s) | LR2–LR33 (400 – 13,200 s) |
| 3 | Sloping beach profile evolution in front of wall. | HR6–HR10 (2000 – 4000 s) | LR34–LR35 (13,200 – 14,000 s) |

3.1.2 Transport Rates

In this experiment, the rates of water and sediment carried over the vertical wall crest at the landward end of the runnel were measured as averages over each 400-s run. The HR and LR tests were set up to mimic 3D and 2D ridge-runnel water and sediment transport patterns, respectively. During the HR test water and sediment were allowed to exit the runnel by either offshore return flow over the ridge or onshore wave overtopping and overwash over the vertical wall. For the LR test the latter possibility was eliminated. Hence, transport rates over the vertical wall were zero for LR.

During each run of the HR test, water and sediment were transported over the crest of the vertical wall by wave overtopping. This overwash was then forced through a horizontal streamer trap retaining the sand particles by means of a fine polyester fabric mesh (Section 2.4.2). The overtopped water was collected, measured and pumped back into the wave tank to keep the SWL constant during a run. The analysis of each collected sand sample included its wet weight immediately after the collection and its dry weight after 12 hours of oven drying.

Overwash sediment volume per unit width, V_{bs} , was estimated using the entire dry weight of a sample and dividing it by the density of quartz sand $\rho_s = 2.6 \text{ g/cm}^3$ and the width of the flume (115 cm) where V_{bs} is the volume per unit width of the overwash sand without voids (bedload + suspended load). Water volume is comprised of two parts including the amount overtopped and measured during a run and the amount stored in the wet overwash sand. The water volume per unit width, V_m , was obtained by dividing the measured volume (cm^3) by the flume width of 115 cm. In Figure 3.4 the overwash results from the HR test are plotted as time series of the sediment (bedload + suspended load) transport rate q_{bs} , the water transport (wave overtopping) rate q_m and their ratio q_{bs}/q_m . These rates (cm^2/s) represent averages over the respective run lasting 400 s and each data point is plotted

at the middle of the respective 400-s run interval with

$$\begin{aligned} q_{bs} &= \frac{V_{bs}}{400 \text{ s}} \\ q_m &= \frac{V_m}{400 \text{ s}} \end{aligned} \quad (3.1)$$

It is noted that the time-averaged volume flux q is constant in the absence of water ponding. For the three overwash tests in Figlus et al. (2009), the wave overtopping rate is denoted as q_o because of the assumption of no water ponding and $q = q_o$. For the HR and LR tests, q varies with x and $q = q_m$ at $x = x_m$ located at the landward end (maximum x_m) of the beach, corresponding to the location of the vertical wall.

The combined bedload and suspended load transport rate q_{bs} (top panel) changes by an order of magnitude from the initial run ($0.01 \text{ cm}^2/\text{s}$) to the final run ($0.20 \text{ cm}^2/\text{s}$). The change happens quite rapidly between runs HR5 and HR7. This transition appears to be related to the change of the beach profile in front of the vertical wall in view of Figure 3.2 where the vertical wall exposed to wave action after HR5 was covered with sediment after HR6. Outside of this transition period the values remain fairly constant at the two values above. The runnel was filled up completely with sediment after HR5.

The wave overtopping rate q_m (middle panel) varies less among the ten runs. The initial maximum of $24 \text{ cm}^2/\text{s}$ was followed by a steady decrease over the next 3 runs to a minimum value of $9 \text{ cm}^2/\text{s}$ in run HR4. After that, the overtopping rate increased slightly over 2 runs and then stayed approximately constant ($14 \text{ cm}^2/\text{s}$) for the remainder of the test (HR7-HR10). The difference in elevation between the changing ridge crest and the fixed wall crest explains the steady decrease from maximum to minimum overtopping rate during the first 4 runs (HR1-HR4). In the beginning of the HR test, the ridge crest was higher than the vertical wall crest

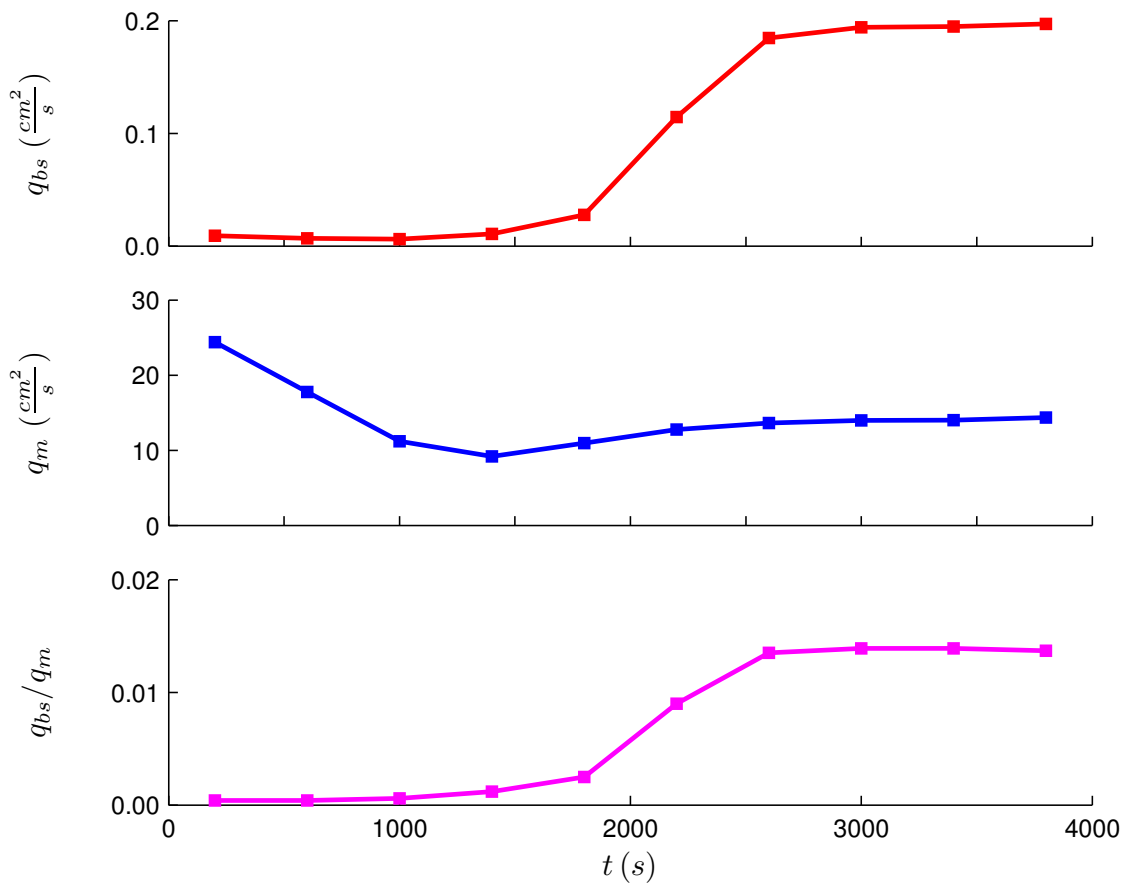


Figure 3.4: Overwash transport rate parameters as a function of time t for the HR test. The top two panels show the sand transport rate q_{bs} (bedload + suspended load) and water transport rate q_m , respectively. Their ratio is depicted in the bottom panel. Data points are averages over the respective 400-s run.

and water transported over the ridge crest filled up the runnel and was carried over the vertical wall. As the ridge crest was lowered and migrated onshore, wave overtopping of the ridge crest might have decreased and offshore return flow might have increased. The increase in q_m between HR4 and HR6 could be explained by the coverage of the wall with sediment as was the case with q_{bs} (sediment) but this effect on q_m (water) was more subtle. After HR6, the overtopping rate q_m was limited by the crest elevation of the vertical wall.

The ratio q_{bs}/q_m is the sediment concentration in the overtopping flow and follows the same trend as q_{bs} due to its larger relative changes compared to q_m . Values ranged from 0.04% during HR1 to 1.4% at the end of the test. It should be stated again that $q_{bs} = 0$ and $q_m = 0$ during the entire LR test. As a result, no figure is plotted for q_{bs} and q_m for LR.

3.1.3 Ridge and Runnel Geometry Evolution

Geometric parameters of the ridge and runnel obtained from the 2D profiles are used to quantify the profile changes in concise manners. Cross-shore and long-shore coordinates of the ridge crest (x_c, z_c) and runnel trough (x_t, z_t) are determined as local maxima and minima, respectively. Vertical coordinates are given with respect to SWL. Ridge and runnel volumes per unit flume width are parameterized as areas with respect to SWL (A_+, A_-) as well as with respect to crest and trough elevation (A_c, A_t) as shown in Figure 3.5.

A_+ is the ridge crest area above SWL bounded by the first two consecutive zero-crossing points of the profile with the x-axis. By definition, A_+ is always positive. A_- is the trough area (void) below SWL bounded by the second and third profile zero-crossing points. A_- is always negative. These values indicate the changes of ridge and runnel areas relative to SWL but can only be computed if three profile zero-crossing points exist. As soon as the runnel trough elevation exceeds SWL, A_+ and A_- cannot be determined.

The parameters A_c and A_t avoid this shortcoming and can be calculated as long as the ridge-runnel feature exists. A_c is the ridge crest area above the horizontal line through (x_t, z_t) . It is bounded in cross-shore direction by x_t and the offshore intersection of the horizontal line with the profile. A_t is the trough area (possible ponded water area) below the horizontal line through (x_c, z_c) . It is bounded in cross-shore direction by x_c and the onshore intersection of the horizontal line with the profile or the landward end of the profile ($x = 19.9\text{ m}$) if no intersection exists.

The temporal variation of the parameters is displayed for the HR (left) and LR (right) tests where values related to the ridge crest are shown as blue circles and values related to the runnel trough are shown as red squares. The time axes extend over the entire test duration of the respective test. The measured evolution of sediment overwash and wave overtopping rates for HR in Figure 3.4 are shown again

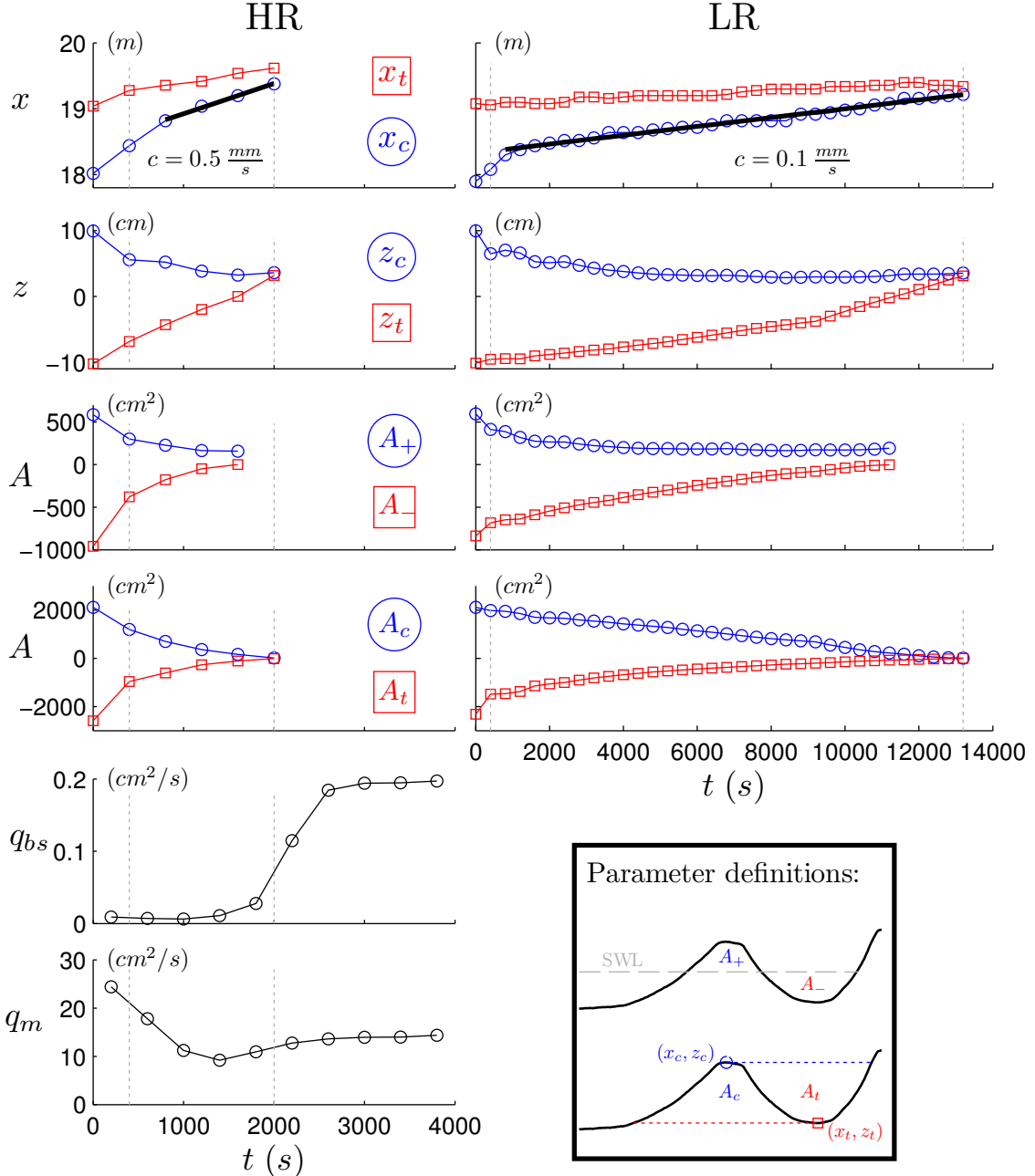


Figure 3.5: Temporal variation of ridge and runnel geometry parameters for HR (left) and LR (right). Three ridge-runnel evolution phases are separated by vertical dashed lines. The onshore speed c of crest migration during Phase 2 is 0.5 mm/s and 0.1 mm/s for HR and LR, respectively.

to interpret the measured temporal changes physically. Finally, vertical dashed lines demarcate the three evolution phases in Table 3.1.

In both the HR and LR tests, the initial cross-shore locations of crest (x_c) and trough (x_t) were located approximately 1 m apart at $x = 18$ and $x = 19$ m, respectively. After the initial landward migration during Phase 1, both x_c and x_t settled into a relatively steady landward migration rate during Phase 2. The ridge migration speed is estimated as the slope c of the $x_c(t)$ curve during Phase 2 only. For HR this rate was 0.5 mm/s (3 cm/min) whereas the LR ridge moved at a speed of 0.1 mm/s (0.6 cm/min), 5 times slower than the HR ridge.

Initial vertical locations for crest and trough were $z_c = 10$ cm and $z_t = -10$ cm, respectively, for both tests. In Phase 1 the crest elevation was reduced by about 4 cm for HR and LR. During Phase 2 of the HR test z_c first decreased to its minimum value before increasing slightly as the ridge-runnel feature migrated onshore on the sloping beach. The minimum z_c value was 3.25 cm after HR4 which coincided with the minimum wave overtopping rate q_o . The overall trend for z_c during the LR test was similar with a minimum of 2.86 cm after LR21. However, before LR21 the crest elevation actually increased slightly during LR2 and LR6. In general, for both tests z_c changed less during Phase 2 than Phase 1. The trough elevation z_t increased steadily for HR and LR with a final value of about 3 cm above SWL for both tests.

The evolution of the area changes with respect to SWL is shown in the third row of panels in Figure 3.5. For HR (LR) A_+ decreased from 586 cm² (595 cm²) to 158 cm² (194 cm²) at the end of HR5 (LR28). The values stayed positive since the ridge crest remained above SWL. The area A_- was negative and decreased in absolute value from 959 cm² (837 cm²) to 0 (1 cm²) in run HR5 (LR28). The fourth row of panels displays A_c and A_t . The initial value of A_c and A_t are about 3 times larger than the respective values for A_+ and A_- . The Phase 2 evolution of A_c and

A_t followed a relatively linear trend with both values merging at zero after the ridge-runnel feature was merged. All parameter values shown in Figure 3.5 are tabulated in Tables 3.2 and 3.3 for HR and LR, respectively.

Table 3.2: Temporal variation of ridge-runnel geometry for HR test.

| Profile | t (s) | x_c (m) | z_c (cm) | A_+ (cm^2) | A_e (cm^2) | x_t (m) | z_t (cm) | A_- (cm^2) | A_t (cm^2) |
|---------|------------|--------------|---------------|---------------------|---------------------|--------------|---------------|---------------------|---------------------|
| HR0 | 0 | 18.02 | 9.95 | 586 | 2115 | 19.04 | -10.25 | -959 | -2589 |
| HR1 | 400 | 18.44 | 5.57 | 301 | 1194 | 19.28 | -6.87 | -379 | -965 |
| HR2 | 800 | 18.82 | 5.21 | 228 | 696 | 19.36 | -4.31 | -177 | -608 |
| HR3 | 1200 | 19.04 | 3.84 | 164 | 360 | 19.42 | -1.96 | -48 | -268 |
| HR4 | 1600 | 19.20 | 3.25 | 158 | 159 | 19.54 | -0.01 | 0 | -110 |
| HR5 | 2000 | 19.38 | 3.61 | N/A | 10 | 19.62 | 3.18 | N/A | -9 |
| HR6 | 2400 | N/A | N/A | N/A | N/A | N/A | N/A | N/A | N/A |
| HR7 | 2800 | N/A | N/A | N/A | N/A | N/A | N/A | N/A | N/A |
| HR8 | 3200 | N/A | N/A | N/A | N/A | N/A | N/A | N/A | N/A |
| HR9 | 3600 | N/A | N/A | N/A | N/A | N/A | N/A | N/A | N/A |
| HR10 | 4000 | N/A | N/A | N/A | N/A | N/A | N/A | N/A | N/A |

N/A implies no parameter value identifiable from the measured profile.

Table 3.3: Temporal variation of ridge-runnel geometry for LR test.

| Profile | t (s) | x_c (m) | z_c (cm) | A_+ (cm^2) | A_c (cm^2) | x_t (m) | z_t (cm) | A_- (cm^2) | A_t (cm^2) |
|---------|------------|--------------|---------------|---------------------|---------------------|--------------|---------------|---------------------|---------------------|
| LR0 | 0 | 17.90 | 9.98 | 595 | 2110 | 19.08 | -10.14 | -837 | -2315 |
| LR1 | 400 | 18.08 | 6.48 | 414 | 1975 | 19.06 | -9.56 | -683 | -1482 |
| LR2 | 800 | 18.30 | 7.03 | 388 | 1948 | 19.10 | -9.46 | -648 | -1466 |
| LR3 | 1200 | 18.38 | 6.60 | 320 | 1854 | 19.10 | -9.49 | -637 | -1378 |
| LR4 | 1600 | 18.44 | 5.27 | 274 | 1701 | 19.08 | -9.05 | -589 | -1141 |
| LR5 | 2000 | 18.48 | 5.14 | 266 | 1673 | 19.08 | -8.82 | -544 | -1058 |
| LR6 | 2400 | 18.52 | 5.27 | 267 | 1653 | 19.10 | -8.61 | -507 | -1008 |
| LR7 | 2800 | 18.52 | 4.73 | 243 | 1591 | 19.18 | -8.38 | -473 | -906 |
| LR8 | 3200 | 18.56 | 4.30 | 224 | 1537 | 19.18 | -8.17 | -444 | -817 |
| LR9 | 3600 | 18.64 | 4.01 | 211 | 1488 | 19.16 | -7.97 | -420 | -744 |
| LR10 | 4000 | 18.64 | 3.80 | 200 | 1428 | 19.18 | -7.68 | -385 | -685 |
| LR11 | 4400 | 18.64 | 3.58 | 193 | 1373 | 19.20 | -7.41 | -353 | -625 |
| LR12 | 4800 | 18.68 | 3.40 | 189 | 1323 | 19.20 | -7.15 | -325 | -570 |
| LR13 | 5200 | 18.70 | 3.31 | 188 | 1274 | 19.20 | -6.90 | -300 | -523 |
| LR14 | 5600 | 18.72 | 3.25 | 184 | 1204 | 19.20 | -6.56 | -270 | -484 |
| LR15 | 6000 | 18.72 | 3.20 | 183 | 1139 | 19.20 | -6.23 | -243 | -445 |
| LR16 | 6400 | 18.76 | 3.17 | 184 | 1075 | 19.20 | -5.89 | -217 | -409 |
| LR17 | 6800 | 18.82 | 3.21 | 188 | 1015 | 19.22 | -5.57 | -196 | -378 |
| LR18 | 7200 | 18.82 | 3.12 | 180 | 936 | 19.26 | -5.20 | -172 | -345 |
| LR19 | 7600 | 18.82 | 3.04 | 172 | 870 | 19.28 | -4.87 | -148 | -313 |
| LR20 | 8000 | 18.82 | 2.95 | 167 | 815 | 19.30 | -4.58 | -126 | -280 |
| LR21 | 8400 | 18.82 | 2.86 | 166 | 767 | 19.30 | -4.32 | -107 | -247 |
| LR22 | 8800 | 18.92 | 2.91 | 168 | 721 | 19.30 | -4.05 | -92 | -224 |
| LR23 | 9200 | 18.92 | 2.97 | 175 | 679 | 19.30 | -3.78 | -80 | -201 |
| LR24 | 9600 | 18.94 | 2.95 | 173 | 552 | 19.34 | -3.00 | -58 | -174 |
| LR25 | 10000 | 18.98 | 2.94 | 172 | 448 | 19.34 | -2.28 | -38 | -147 |
| LR26 | 10400 | 19.00 | 2.96 | 174 | 355 | 19.34 | -1.56 | -21 | -123 |
| LR27 | 10800 | 19.06 | 3.02 | 182 | 278 | 19.36 | -0.87 | -8 | -100 |
| LR28 | 11200 | 19.08 | 3.16 | 194 | 218 | 19.36 | -0.22 | -1 | -82 |
| LR29 | 11600 | 19.16 | 3.39 | N/A | 171 | 19.40 | 0.39 | N/A | -68 |
| LR30 | 12000 | 19.16 | 3.40 | N/A | 105 | 19.40 | 1.11 | N/A | -49 |
| LR31 | 12400 | 19.18 | 3.41 | N/A | 57 | 19.36 | 1.79 | N/A | -32 |
| LR32 | 12800 | 19.20 | 3.45 | N/A | 24 | 19.36 | 2.47 | N/A | -17 |
| LR33 | 13200 | 19.22 | 3.55 | N/A | 6 | 19.34 | 3.13 | N/A | -5 |
| LR34 | 13600 | N/A | N/A | N/A | N/A | N/A | N/A | N/A | N/A |
| LR35 | 14000 | N/A | N/A | N/A | N/A | N/A | N/A | N/A | N/A |

N/A implies no parameter value identifiable from the measured profile.

3.2 Wave Gauge Records

Wave gauges 1 through 8 recorded free-surface elevation during 10 HR runs and 35 LR runs. Each of these 400-s time series yielded information about wave parameters, power spectral density, wave setup or setdown, and wet probability at the respective cross-shore location listed in Table 2.2. These data are analyzed and explained in the following sections. The initial transition of 20 s in each 400-s time series is removed to eliminate ramp-up effects. The reduced time series comprised approximately 200 waves which is sufficient for statistical analysis.

3.2.1 Offshore Parameters

Wave parameters measured at the location of WG1 ($x = 0$) are considered offshore in this experiment. WG1 was located approximately 3 m away from the wave maker in a water depth of 0.90 m for the HR test and 0.82 m for the LR test. Tables 3.4 to 3.7 list the incident and total (incident + reflected) wave parameters from the spectral and time series analysis of each 400-s run of the HR and LR tests. Measured time series from WG1, WG2, and WG3 were used to separate incident and reflected waves as explained in Section 2.2.1. Tabulated parameters include the spectral significant wave height H_{mo} , the root-mean-square wave height H_{rms} and the significant wave height H_s as well as the spectral peak period T_p and the significant wave period T_s . In addition, the reflection coefficient R is listed. Average values for all runs of each test are given at the bottom of the respective tables.

The parameters H_{mo} , H_{rms} , and T_p are derived from the wave frequency spectrum. Integrating the wave frequency spectrum in the frequency domain yields the zero-th moment, m_0 (cm²), which is equivalent to the variance of the free surface elevation by definition of the wave frequency spectrum (Goda, 2000). Similarly, the standard deviation, σ_η , of the free-surface elevation is equal to the square root of the zeroth moment ($\sigma_\eta = \sqrt{m_0}$). The spectral significant wave height is defined as $H_{mo} = 4\sigma_\eta$ and the root-mean-square wave height is defined here as $H_{rms} =$

Table 3.4: Spectrum and time series parameters for incident waves at WG1 location for 10 runs of HR test.

| Run | H_{mo} (cm) | H_{rms} (cm) | H_s (cm) | T_p (s) | T_s (s) | R |
|------|---------------|----------------|------------|-----------|-----------|------|
| HR1 | 17.90 | 12.66 | 17.95 | 2.57 | 2.32 | 0.17 |
| HR2 | 18.01 | 12.73 | 17.86 | 2.57 | 2.28 | 0.13 |
| HR3 | 18.18 | 12.86 | 17.79 | 2.57 | 2.27 | 0.10 |
| HR4 | 18.20 | 12.87 | 17.92 | 2.57 | 2.30 | 0.10 |
| HR5 | 18.31 | 12.95 | 18.06 | 2.57 | 2.30 | 0.11 |
| HR6 | 18.24 | 12.90 | 17.96 | 2.57 | 2.31 | 0.10 |
| HR7 | 18.21 | 12.88 | 17.92 | 2.57 | 2.28 | 0.10 |
| HR8 | 18.16 | 12.84 | 17.86 | 2.57 | 2.30 | 0.10 |
| HR9 | 18.12 | 12.82 | 17.75 | 2.57 | 2.29 | 0.10 |
| HR10 | 18.19 | 12.86 | 18.08 | 2.57 | 2.30 | 0.10 |
| Avg. | 18.15 | 12.84 | 17.91 | 2.57 | 2.29 | 0.11 |

Table 3.5: Spectrum and time series parameters for total (= incident + reflected) waves at WG1 location for 10 runs of HR test.

| Run | H_{mo} (cm) | H_{rms} (cm) | H_s (cm) | T_p (s) | T_s (s) | R |
|------|---------------|----------------|------------|-----------|-----------|------|
| HR1 | 17.72 | 12.53 | 17.53 | 2.70 | 2.33 | 0.17 |
| HR2 | 17.68 | 12.50 | 17.34 | 2.57 | 2.30 | 0.13 |
| HR3 | 18.03 | 12.75 | 17.84 | 2.57 | 2.31 | 0.10 |
| HR4 | 17.99 | 12.72 | 17.88 | 2.57 | 2.28 | 0.10 |
| HR5 | 18.05 | 12.76 | 17.99 | 2.57 | 2.29 | 0.11 |
| HR6 | 17.98 | 12.71 | 17.72 | 2.57 | 2.31 | 0.10 |
| HR7 | 17.99 | 12.72 | 17.91 | 2.57 | 2.32 | 0.10 |
| HR8 | 17.89 | 12.65 | 17.70 | 2.57 | 2.32 | 0.10 |
| HR9 | 17.92 | 12.67 | 17.83 | 2.57 | 2.33 | 0.10 |
| HR10 | 17.95 | 12.69 | 17.73 | 2.57 | 2.31 | 0.10 |
| Avg. | 17.92 | 12.67 | 17.75 | 2.58 | 2.31 | 0.11 |

Table 3.6: Spectrum and time series parameters for incident waves at WG1 location for 35 runs of LR test.

| Run | H_{mo} (cm) | H_{rms} (cm) | H_s (cm) | T_p (s) | T_s (s) | R |
|------|---------------|----------------|------------|-----------|-----------|------|
| LR1 | 17.98 | 12.71 | 17.89 | 2.57 | 2.34 | 0.14 |
| LR2 | 17.68 | 12.50 | 17.47 | 2.57 | 2.31 | 0.12 |
| LR3 | 17.75 | 12.55 | 17.48 | 2.57 | 2.33 | 0.11 |
| LR4 | 17.33 | 12.26 | 17.06 | 2.57 | 2.30 | 0.10 |
| LR5 | 17.37 | 12.28 | 17.27 | 2.57 | 2.31 | 0.10 |
| LR6 | 17.49 | 12.37 | 17.27 | 2.57 | 2.31 | 0.10 |
| LR7 | 17.53 | 12.39 | 17.10 | 2.57 | 2.27 | 0.10 |
| LR8 | 17.45 | 12.34 | 17.18 | 2.57 | 2.30 | 0.09 |
| LR9 | 17.45 | 12.34 | 17.13 | 2.57 | 2.32 | 0.10 |
| LR10 | 17.34 | 12.26 | 17.09 | 2.57 | 2.31 | 0.10 |
| LR11 | 17.50 | 12.37 | 17.15 | 2.57 | 2.31 | 0.09 |
| LR12 | 17.50 | 12.37 | 17.22 | 2.57 | 2.31 | 0.10 |
| LR13 | 17.46 | 12.35 | 17.29 | 2.57 | 2.31 | 0.10 |
| LR14 | 17.49 | 12.37 | 17.18 | 2.57 | 2.34 | 0.10 |
| LR15 | 17.46 | 12.35 | 17.19 | 2.57 | 2.31 | 0.10 |
| LR16 | 17.49 | 12.36 | 17.26 | 2.57 | 2.32 | 0.10 |
| LR17 | 17.42 | 12.32 | 17.18 | 2.57 | 2.31 | 0.10 |
| LR18 | 18.06 | 12.77 | 17.77 | 2.57 | 2.31 | 0.10 |
| LR19 | 18.18 | 12.86 | 17.71 | 2.57 | 2.27 | 0.10 |
| LR20 | 18.18 | 12.86 | 17.79 | 2.57 | 2.30 | 0.10 |
| LR21 | 18.17 | 12.85 | 17.77 | 2.57 | 2.28 | 0.10 |
| LR22 | 18.21 | 12.88 | 17.83 | 2.57 | 2.26 | 0.10 |
| LR23 | 18.18 | 12.86 | 17.91 | 2.57 | 2.26 | 0.10 |
| LR24 | 17.98 | 12.71 | 17.55 | 2.57 | 2.28 | 0.10 |
| LR25 | 18.12 | 12.81 | 17.93 | 2.57 | 2.31 | 0.10 |
| LR26 | 18.09 | 12.79 | 17.85 | 2.57 | 2.30 | 0.10 |
| LR27 | 18.09 | 12.79 | 17.85 | 2.57 | 2.30 | 0.10 |
| LR28 | 18.07 | 12.78 | 17.85 | 2.57 | 2.28 | 0.10 |
| LR29 | 18.09 | 12.79 | 17.92 | 2.57 | 2.28 | 0.10 |
| LR30 | 17.87 | 12.64 | 17.63 | 2.57 | 2.29 | 0.10 |
| LR31 | 18.03 | 12.75 | 17.63 | 2.57 | 2.30 | 0.10 |
| LR32 | 18.04 | 12.75 | 17.85 | 2.57 | 2.28 | 0.10 |
| LR33 | 18.04 | 12.76 | 17.95 | 2.57 | 2.29 | 0.10 |
| LR34 | 18.09 | 12.79 | 17.80 | 2.57 | 2.34 | 0.10 |
| LR35 | 18.09 | 12.79 | 17.80 | 2.57 | 2.31 | 0.10 |
| Avg. | 17.81 | 12.59 | 17.54 | 2.57 | 2.30 | 0.10 |

Table 3.7: Spectrum and time series parameters for total (= incident + reflected) waves at WG1 location for 35 runs of LR test.

| Run | H_{mo} (cm) | H_{rms} (cm) | H_s (cm) | T_p (s) | T_s (s) | R |
|------|---------------|----------------|------------|-----------|-----------|------|
| LR1 | 17.86 | 12.63 | 17.79 | 2.57 | 2.33 | 0.14 |
| LR2 | 17.51 | 12.38 | 17.10 | 2.57 | 2.32 | 0.12 |
| LR3 | 17.55 | 12.41 | 17.44 | 2.57 | 2.32 | 0.11 |
| LR4 | 17.08 | 12.08 | 16.94 | 2.57 | 2.32 | 0.10 |
| LR5 | 17.10 | 12.09 | 16.80 | 2.57 | 2.31 | 0.10 |
| LR6 | 17.22 | 12.17 | 17.03 | 2.57 | 2.34 | 0.10 |
| LR7 | 17.27 | 12.21 | 16.90 | 2.57 | 2.31 | 0.10 |
| LR8 | 17.20 | 12.16 | 17.02 | 2.57 | 2.33 | 0.09 |
| LR9 | 17.21 | 12.17 | 17.00 | 2.57 | 2.32 | 0.10 |
| LR10 | 17.08 | 12.08 | 16.99 | 2.57 | 2.35 | 0.10 |
| LR11 | 17.24 | 12.19 | 17.18 | 2.57 | 2.33 | 0.09 |
| LR12 | 17.26 | 12.20 | 17.02 | 2.57 | 2.31 | 0.10 |
| LR13 | 17.23 | 12.19 | 17.06 | 2.57 | 2.32 | 0.10 |
| LR14 | 17.25 | 12.20 | 16.98 | 2.57 | 2.33 | 0.10 |
| LR15 | 17.23 | 12.18 | 17.00 | 2.57 | 2.34 | 0.10 |
| LR16 | 17.21 | 12.17 | 17.03 | 2.57 | 2.31 | 0.10 |
| LR17 | 17.15 | 12.13 | 17.19 | 2.57 | 2.34 | 0.10 |
| LR18 | 17.91 | 12.67 | 17.67 | 2.57 | 2.34 | 0.10 |
| LR19 | 18.04 | 12.76 | 17.75 | 2.57 | 2.34 | 0.10 |
| LR20 | 18.06 | 12.77 | 17.63 | 2.57 | 2.31 | 0.10 |
| LR21 | 18.05 | 12.76 | 17.89 | 2.57 | 2.31 | 0.10 |
| LR22 | 18.10 | 12.80 | 17.69 | 2.57 | 2.31 | 0.10 |
| LR23 | 18.04 | 12.76 | 17.89 | 2.57 | 2.33 | 0.10 |
| LR24 | 17.85 | 12.63 | 17.70 | 2.57 | 2.32 | 0.10 |
| LR25 | 17.98 | 12.71 | 17.69 | 2.57 | 2.33 | 0.10 |
| LR26 | 17.97 | 12.71 | 17.83 | 2.57 | 2.35 | 0.10 |
| LR27 | 17.94 | 12.69 | 17.70 | 2.57 | 2.33 | 0.10 |
| LR28 | 17.97 | 12.70 | 17.72 | 2.57 | 2.33 | 0.10 |
| LR29 | 17.93 | 12.68 | 17.77 | 2.57 | 2.33 | 0.10 |
| LR30 | 17.73 | 12.54 | 17.42 | 2.57 | 2.32 | 0.10 |
| LR31 | 17.89 | 12.65 | 17.70 | 2.57 | 2.34 | 0.10 |
| LR32 | 17.88 | 12.64 | 17.50 | 2.57 | 2.33 | 0.10 |
| LR33 | 17.91 | 12.66 | 17.80 | 2.57 | 2.31 | 0.10 |
| LR34 | 17.96 | 12.70 | 17.69 | 2.57 | 2.30 | 0.10 |
| LR35 | 17.96 | 12.70 | 17.82 | 2.57 | 2.33 | 0.10 |
| Avg. | 17.62 | 12.46 | 17.41 | 2.57 | 2.33 | 0.10 |

$H_{mo}/\sqrt{2}$. T_p is the wave period associated with the largest wave energy (reciprocal of the frequency at the peak of the wave frequency spectrum). The values of H_s and T_s are derived from the measured time series of the free-surface elevation via the zero-upcrossing method which separates individual waves in the time series. The average height of the highest one third of the waves in the time series is the significant wave height H_s and the average period of the highest one third of the waves is T_s .

The wave maker input was the same irregular wave signal for all runs in this experiment. The variability in measured offshore parameters between runs of the same test is small and indicates an acceptable level of repeatability. The disparities between respective HR and LR parameters due to the 8 cm water depth difference were small. This facilitates comparisons between the two tests.

For the HR test average (indicated by angle brackets) incident wave height values were $\langle H_{mo} \rangle = 18.15$, $\langle H_{rms} \rangle = 12.84$, and $\langle H_s \rangle = 17.91 \text{ cm}$ compared to $\langle H_{mo} \rangle = 17.81$, $\langle H_{rms} \rangle = 12.59$, and $\langle H_s \rangle = 17.54 \text{ cm}$ for the LR test. Spectral peak period values were constant in every run of both tests ($T_p = 2.57 \text{ s}$). T_s was slightly less than T_p and shows a little more variation ($\pm 0.07 \text{ s}$) with an overall average value of 2.30 s for HR and 2.33 s for LR. The reflection coefficient, R , had an average value of 0.11 (HR) and 0.10 (LR) but varied slightly in each test from higher (0.14) to lower (0.10) values which can be attributed to the flattening of the ridge.

3.2.2 Setup, Wave Height, and Wet Probability

Wave setup, wave height, and wet probability are statistical values computed from the recorded free-surface elevation time series at the WG1-WG8 locations. Free-surface elevation at any cross-shore location is given by

$$\eta(t) = h(t) + z_b(t) \quad (3.2)$$

where the free-surface elevation $\eta(t)$ and the bottom elevation $z_b(t)$ are in reference to $z = 0$ (SWL) and $h(t)$ is the time dependent local water depth ($h \geq 0$).

The mean free-surface elevation, $\bar{\eta}$, its standard deviation, σ_η , and the wet probability, P_w , are the statistical properties computed for all eight gauge locations. The standard deviation σ_η is related to the significant wave height $H_{mo} = 4\sigma_\eta$. The mean free-surface elevation $\bar{\eta}$ for each WG record is the setup ($\bar{\eta} > 0$) or setdown ($\bar{\eta} < 0$) with respect to SWL at that cross-shore location in the flume. The overbar indicates time averaging during the wet duration during which the bottom of the wave gauge location is submerged in water. The associated wet probability, P_w , indicates the likelihood of that bottom location to be submerged in water at any given time during a run and is obtained as

$$P_w = \frac{J_{wet}}{J} \quad (3.3)$$

where J is the total number of data points in the recorded free-surface elevation time series and J_{wet} represents the number of data points for which the gauge at that location is considered to be submerged in water. For cross-shore locations in the intermittently wet and dry zone the water depth of the wave uprush and downrush can be very small, which makes the determination of the exact wet duration and wet probability rather difficult. A procedure for obtaining free-surface elevation from wave gauges located in that region is explained by Figlus et al. (2009). Only

WG7 and WG8 are affected in the present experiment and are analyzed further in Section 3.2.4.

The analysis of the data from gauges WG1-WG6 is a straightforward linear conversion from measured voltage to free-surface elevation $\eta(t)$ with zero reading at SWL and wet probability of $P_w = 1$ since $J_{wet} = J$ in Equation (3.3). Tables 3.8 and 3.9 list the $\bar{\eta}$ values for every run in test HR and LR, respectively. Setdown was consistently observed in all runs for WG1 through WG4 whereas WG5 through WG8 always showed setup. The only exception was run HR1 for WG6 with a negative outlier value of $\bar{\eta} = -0.15\text{ cm}$. The distinct change from setdown to setup between WG4 and WG5 indicates that a majority of the waves broke in this region as confirmed by visual observation.

Table 3.8: Mean free-surface elevation $\bar{\eta}$ (cm) at 8 wave gauge locations for 10 runs of HR test.

| Run | WG1 | WG2 | WG3 | WG4 | WG5 | WG6 | WG7 | WG8 |
|------|-------|-------|-------|-------|------|-------|------|------|
| HR1 | -0.30 | -0.29 | -0.23 | -0.40 | 0.08 | -0.15 | 6.33 | 5.37 |
| HR2 | -0.37 | -0.05 | -0.05 | -0.17 | 0.23 | 0.01 | 5.21 | 5.53 |
| HR3 | -0.09 | -0.07 | -0.01 | -0.14 | 0.26 | 0.09 | 3.62 | 5.35 |
| HR4 | -0.13 | -0.07 | -0.13 | -0.22 | 0.24 | 0.10 | 2.71 | 5.02 |
| HR5 | -0.04 | -0.03 | -0.01 | -0.14 | 0.28 | 0.24 | 2.38 | 4.92 |
| HR6 | -0.08 | -0.05 | 0.02 | -0.11 | 0.33 | 0.39 | 2.33 | 4.84 |
| HR7 | -0.07 | -0.04 | -0.01 | -0.11 | 0.30 | 0.32 | 1.99 | 4.94 |
| HR8 | -0.06 | -0.01 | -0.01 | -0.12 | 0.05 | 0.29 | 1.78 | 4.71 |
| HR9 | -0.05 | -0.04 | 0.02 | -0.10 | 0.33 | 0.41 | 1.67 | 4.61 |
| HR10 | -0.04 | -0.03 | -0.04 | -0.12 | 0.29 | 0.35 | 1.67 | 4.39 |

The mean water level $\bar{\eta}$ deviated within $\pm 4\text{ mm}$ from SWL for WG1-6 whereas WG7 and WG8 were affected by $z_b(t)$ in Equation (3.2). Fluctuations between runs may be due to various reasons. Even though care was taken to always keep the SWL

Table 3.9: Mean free-surface elevation $\bar{\eta}$ (cm) at 8 wave gauge locations for 35 runs of LR test.

| Run | WG1 | WG2 | WG3 | WG4 | WG5 | WG6 | WG7 | WG8 |
|------|-------|-------|-------|-------|------|------|------|------|
| LR1 | -0.19 | -0.12 | -0.15 | -0.24 | 0.61 | 0.59 | 5.11 | 5.63 |
| LR2 | -0.12 | -0.04 | -0.05 | -0.11 | 0.64 | 0.70 | 7.18 | 7.21 |
| LR3 | -0.12 | -0.11 | -0.11 | -0.10 | 0.65 | 0.75 | 7.01 | 7.20 |
| LR4 | -0.12 | -0.05 | -0.05 | -0.10 | 0.66 | 0.81 | 5.95 | 6.25 |
| LR5 | -0.14 | -0.08 | -0.07 | -0.09 | 0.63 | 0.84 | 5.83 | 6.10 |
| LR6 | -0.07 | -0.05 | -0.08 | -0.10 | 0.64 | 0.85 | 5.92 | 6.03 |
| LR7 | -0.15 | -0.09 | -0.07 | -0.12 | 0.63 | 0.85 | 5.93 | 6.00 |
| LR8 | -0.10 | -0.09 | -0.12 | -0.11 | 0.61 | 0.81 | 5.42 | 5.81 |
| LR9 | -0.09 | -0.11 | -0.11 | -0.14 | 0.56 | 0.79 | 4.98 | 5.51 |
| LR10 | -0.09 | -0.05 | -0.08 | -0.12 | 0.56 | 0.82 | 4.59 | 5.26 |
| LR11 | -0.11 | -0.12 | -0.11 | -0.14 | 0.59 | 0.81 | 4.44 | 5.05 |
| LR12 | -0.10 | -0.10 | -0.13 | -0.09 | 0.59 | 0.81 | 4.24 | 4.78 |
| LR13 | -0.10 | -0.14 | -0.12 | -0.14 | 0.59 | 0.82 | 4.10 | 4.70 |
| LR14 | -0.14 | -0.10 | -0.12 | -0.08 | 0.60 | 0.81 | 3.99 | 4.60 |
| LR15 | -0.12 | -0.12 | -0.11 | -0.12 | 0.58 | 0.82 | 3.99 | 4.46 |
| LR16 | -0.12 | -0.11 | -0.10 | -0.13 | 0.57 | 0.80 | 3.90 | 4.39 |
| LR17 | -0.11 | -0.10 | -0.11 | -0.14 | 0.57 | 0.78 | 3.72 | 4.26 |
| LR18 | -0.13 | -0.08 | -0.11 | -0.09 | 0.64 | 0.84 | 3.59 | 4.12 |
| LR19 | -0.12 | -0.11 | -0.10 | -0.14 | 0.64 | 0.84 | 3.66 | 4.01 |
| LR20 | -0.15 | -0.10 | -0.11 | -0.12 | 0.60 | 0.83 | 3.52 | 3.96 |
| LR21 | -0.14 | -0.07 | -0.11 | -0.15 | 0.59 | 0.83 | 3.51 | 4.01 |
| LR22 | -0.10 | -0.09 | -0.11 | -0.17 | 0.61 | 0.79 | 3.38 | 3.90 |
| LR23 | -0.10 | -0.06 | -0.11 | -0.13 | 0.64 | 0.79 | 3.17 | 3.94 |
| LR24 | -0.13 | -0.10 | -0.13 | -0.19 | 0.61 | 0.81 | 3.12 | 4.01 |
| LR25 | -0.12 | -0.11 | -0.12 | -0.13 | 0.62 | 0.81 | 3.11 | 3.99 |
| LR26 | -0.12 | -0.09 | -0.11 | -0.15 | 0.60 | 0.79 | 3.03 | 4.01 |
| LR27 | -0.12 | -0.10 | -0.11 | -0.01 | 0.61 | 0.80 | 2.87 | 4.10 |
| LR28 | -0.10 | -0.11 | -0.12 | -0.15 | 0.61 | 0.78 | 2.85 | 4.09 |
| LR29 | -0.11 | -0.10 | -0.12 | -0.13 | 0.62 | 0.75 | 2.84 | 4.22 |
| LR30 | -0.13 | -0.14 | -0.10 | -0.10 | 0.60 | 0.78 | 2.64 | 4.27 |
| LR31 | -0.12 | -0.11 | -0.12 | -0.08 | 0.62 | 0.79 | 2.64 | 4.47 |
| LR32 | -0.10 | -0.08 | -0.16 | -0.10 | 0.61 | 0.77 | 2.55 | 4.75 |
| LR33 | -0.11 | -0.10 | -0.11 | -0.11 | 0.61 | 0.75 | 2.50 | 5.06 |
| LR34 | -0.14 | -0.11 | -0.11 | -0.14 | 0.61 | 0.78 | 2.47 | 5.20 |
| LR35 | -0.10 | -0.11 | -0.10 | -0.13 | 0.61 | 0.73 | 2.37 | 5.52 |

constant, slight variations on the order of 1 mm at the beginning and during a run may have occurred. During runs with significant wave overtopping the recirculation system (Section 2.4.1) pumped water back into the flume to maintain a constant SWL. In addition, the WG accuracy is estimated to be on the order of 1 mm .

WG7 and WG8 were initially located inside the runnel and experienced a much larger variation in $\bar{\eta}$ over the course of the two tests due to ridge migration and runnel water level changes. During the 10 runs of the HR test $\bar{\eta}$ decreased from 6.33 to 1.67 cm (Table 3.8) at the WG7 location and from 5.37 to 4.39 cm at the WG8 location. Since the ridge migration during LR was much slower, the change in $\bar{\eta}$ values happened much slower as well (Table 3.9). For WG7, after an increase from LR1 (5.11 cm) to LR2 (7.18 cm), $\bar{\eta}$ decreased to a value of 2.37 cm in run LR35. Ridge crest elevation and runnel water level (RWL) are the reasons for this evolution. WG8 remained inside the runnel for almost the entire test. Values range from a maximum of 7.21 cm during LR2 to a minimum of 3.90 cm during LR22. The maximum occurred in run LR2 rather than LR1 since water ponded in the runnel during LR1 was retained in run LR2 because the ridge crest remained high during LR2. The minimum was observed right after the crest elevation z_c reached its low point (Table 3.3) followed by a subsequent steady increase due to the increasing bottom elevation at the location of WG8 until the end of the LR test.

Tables 3.10, and 3.11 show the standard deviation, σ_η , at all WG locations for every run. σ_η is an indicator for wave height ($H_{mo} = 4\sigma_\eta$) and decreases after wave breaking. This explains the significant drop in values between the locations of WG4 and WG5 since most waves broke before reaching WG5. In the region of the ridge-runnel system (WG7 and WG8) σ_η was further reduced due to the small water depth in the wet and dry zone.

It has to be noted that the statistical mean and standard deviation of the free-surface elevation presented in Tables 3.8 through 3.11 refer to data points within the

Table 3.10: Standard deviation σ_η (cm) of the free-surface elevation at 8 wave gauge locations for 10 runs of HR test.

| Run | WG1 | WG2 | WG3 | WG4 | WG5 | WG6 | WG7 | WG8 |
|------|------|------|------|------|------|------|------|------|
| HR1 | 4.43 | 4.45 | 4.62 | 4.43 | 3.06 | 3.22 | 1.11 | 1.19 |
| HR2 | 4.42 | 4.42 | 4.58 | 4.50 | 2.99 | 3.19 | 1.14 | 0.62 |
| HR3 | 4.50 | 4.51 | 4.59 | 4.52 | 3.04 | 3.25 | 1.39 | 0.73 |
| HR4 | 4.49 | 4.50 | 4.60 | 4.51 | 3.01 | 3.28 | 1.40 | 0.85 |
| HR5 | 4.51 | 4.52 | 4.62 | 4.53 | 3.01 | 3.19 | 1.49 | 0.91 |
| HR6 | 4.49 | 4.50 | 4.60 | 4.55 | 3.01 | 3.16 | 1.56 | 0.80 |
| HR7 | 4.49 | 4.50 | 4.60 | 4.54 | 3.02 | 3.09 | 1.64 | 0.81 |
| HR8 | 4.47 | 4.48 | 4.59 | 4.49 | 2.94 | 3.06 | 1.76 | 0.95 |
| HR9 | 4.48 | 4.51 | 4.57 | 4.46 | 3.00 | 3.07 | 1.82 | 1.34 |
| HR10 | 4.48 | 4.50 | 4.59 | 4.48 | 2.97 | 3.02 | 1.95 | 1.54 |

wet duration only, to be consistent with the averaging procedure used in the model CSHORE for the wet and dry zone in Chapter 4. The wet probability according to Equation (3.3) is tabulated in Tables 3.12 and 3.13 for WG1-8. Only WG7 and WG8 were located in the intermittently wet and dry zone during some runs with P_w less than unity.

In the HR test the wet probability for WG7 was slightly below unity during HR1-HR3 as the ridge migrated past the gauge. WG8 was affected by the merger of the migrating ridge and runnel starting in run HR5. Towards the end of the HR test WG8 was simply located in the swash zone on the sloping beach with wet probabilities below unity. The lowest value for the HR test was $P_w = 0.78$ (HR9) which still suggests a 78% likelihood of submergence at any given time in that run.

For the LR test WG7 for LR1-LR4 was completely submerged in the runnel. Starting in run LR5 P_w for WG7 dropped slightly below unity as the ridge crest passed by. After the passage of the ridge crest P_w values continued to increase and

Table 3.11: Standard deviation σ_η (cm) of the free-surface elevation at 8 wave gauge locations for 35 runs of LR test.

| Run | WG1 | WG2 | WG3 | WG4 | WG5 | WG6 | WG7 | WG8 |
|------|------|------|------|------|------|------|------|------|
| LR1 | 4.46 | 4.49 | 4.55 | 4.26 | 2.45 | 2.39 | 2.07 | 2.27 |
| LR2 | 4.37 | 4.39 | 4.44 | 4.17 | 2.34 | 2.25 | 0.54 | 0.52 |
| LR3 | 4.38 | 4.41 | 4.46 | 4.17 | 2.27 | 2.26 | 0.48 | 0.38 |
| LR4 | 4.27 | 4.29 | 4.37 | 4.02 | 2.18 | 2.17 | 0.63 | 0.49 |
| LR5 | 4.27 | 4.29 | 4.38 | 4.03 | 2.17 | 2.09 | 0.55 | 0.47 |
| LR6 | 4.30 | 4.33 | 4.41 | 4.02 | 2.17 | 2.05 | 0.52 | 0.48 |
| LR7 | 4.31 | 4.34 | 4.41 | 4.01 | 2.15 | 2.04 | 0.63 | 0.55 |
| LR8 | 4.30 | 4.33 | 4.39 | 4.00 | 2.14 | 2.03 | 0.70 | 0.59 |
| LR9 | 4.30 | 4.33 | 4.40 | 4.00 | 2.14 | 2.02 | 0.80 | 0.63 |
| LR10 | 4.27 | 4.28 | 4.37 | 4.00 | 2.19 | 2.02 | 0.83 | 0.64 |
| LR11 | 4.31 | 4.32 | 4.42 | 3.99 | 2.20 | 2.03 | 0.87 | 0.70 |
| LR12 | 4.31 | 4.31 | 4.41 | 4.00 | 2.19 | 2.02 | 0.92 | 0.73 |
| LR13 | 4.30 | 4.31 | 4.41 | 3.98 | 2.20 | 2.03 | 0.92 | 0.76 |
| LR14 | 4.31 | 4.32 | 4.41 | 4.01 | 2.16 | 2.01 | 0.96 | 0.81 |
| LR15 | 4.30 | 4.31 | 4.41 | 4.04 | 2.18 | 2.02 | 0.91 | 0.84 |
| LR16 | 4.30 | 4.31 | 4.41 | 4.00 | 2.18 | 2.02 | 0.89 | 0.86 |
| LR17 | 4.28 | 4.30 | 4.39 | 3.99 | 2.18 | 2.00 | 0.91 | 0.86 |
| LR18 | 4.47 | 4.51 | 4.50 | 4.24 | 2.37 | 2.06 | 0.87 | 0.75 |
| LR19 | 4.51 | 4.54 | 4.54 | 4.26 | 2.37 | 2.05 | 0.88 | 0.76 |
| LR20 | 4.51 | 4.54 | 4.53 | 4.24 | 2.39 | 2.08 | 0.88 | 0.77 |
| LR21 | 4.51 | 4.54 | 4.53 | 4.23 | 2.40 | 2.07 | 0.87 | 0.79 |
| LR22 | 4.52 | 4.55 | 4.53 | 4.22 | 2.39 | 2.07 | 0.86 | 0.80 |
| LR23 | 4.51 | 4.55 | 4.53 | 4.23 | 2.39 | 2.06 | 0.87 | 0.81 |
| LR24 | 4.46 | 4.48 | 4.49 | 4.25 | 2.41 | 2.05 | 0.88 | 0.81 |
| LR25 | 4.49 | 4.52 | 4.51 | 4.23 | 2.42 | 2.07 | 0.90 | 0.80 |
| LR26 | 4.49 | 4.51 | 4.51 | 4.19 | 2.44 | 2.05 | 0.92 | 0.80 |
| LR27 | 4.48 | 4.51 | 4.51 | 4.20 | 2.43 | 2.07 | 0.93 | 0.80 |
| LR28 | 4.49 | 4.51 | 4.51 | 4.20 | 2.43 | 2.07 | 0.95 | 0.80 |
| LR29 | 4.48 | 4.52 | 4.51 | 4.22 | 2.44 | 2.06 | 0.98 | 0.81 |
| LR30 | 4.43 | 4.44 | 4.46 | 4.19 | 2.39 | 2.06 | 1.01 | 0.77 |
| LR31 | 4.47 | 4.48 | 4.50 | 4.23 | 2.40 | 2.08 | 1.03 | 0.78 |
| LR32 | 4.47 | 4.48 | 4.50 | 4.18 | 2.42 | 2.09 | 1.05 | 0.77 |
| LR33 | 4.47 | 4.49 | 4.50 | 4.19 | 2.41 | 2.10 | 1.08 | 0.80 |
| LR34 | 4.49 | 4.50 | 4.51 | 4.16 | 2.41 | 2.09 | 1.11 | 0.85 |
| LR35 | 4.49 | 4.50 | 4.51 | 4.17 | 2.42 | 2.10 | 1.14 | 0.82 |

approached unity at the end of the LR test. P_w for WG8 was unity until LR33 due to its placement at the landward end of the runnel. Once the runnel disappeared completely in runs LR34 and LR35, P_w was reduced. Minimum wet probabilities during LR are 0.89 (LR6) and 0.63 (LR35) for WG7 and WG8, respectively. These relatively high wet probabilities are partly due to water ponding in the runnel.

Table 3.12: Wet probability P_w at 8 wave gauge locations for 10 runs of HR test.

| Run | WG1 | WG2 | WG3 | WG4 | WG5 | WG6 | WG7 | WG8 |
|------|------|------|------|------|------|------|------|------|
| HR1 | 1.00 | 1.00 | 1.00 | 1.00 | 1.00 | 1.00 | 0.91 | 1.00 |
| HR2 | 1.00 | 1.00 | 1.00 | 1.00 | 1.00 | 1.00 | 0.80 | 1.00 |
| HR3 | 1.00 | 1.00 | 1.00 | 1.00 | 1.00 | 1.00 | 0.95 | 1.00 |
| HR4 | 1.00 | 1.00 | 1.00 | 1.00 | 1.00 | 1.00 | 1.00 | 1.00 |
| HR5 | 1.00 | 1.00 | 1.00 | 1.00 | 1.00 | 1.00 | 1.00 | 0.98 |
| HR6 | 1.00 | 1.00 | 1.00 | 1.00 | 1.00 | 1.00 | 1.00 | 0.85 |
| HR7 | 1.00 | 1.00 | 1.00 | 1.00 | 1.00 | 1.00 | 1.00 | 0.85 |
| HR8 | 1.00 | 1.00 | 1.00 | 1.00 | 1.00 | 1.00 | 1.00 | 0.79 |
| HR9 | 1.00 | 1.00 | 1.00 | 1.00 | 1.00 | 1.00 | 1.00 | 0.78 |
| HR10 | 1.00 | 1.00 | 1.00 | 1.00 | 1.00 | 1.00 | 1.00 | 0.83 |

Table 3.13: Wet probability P_w at 8 wave gauge locations for 35 runs of LR test.

| Run | WG1 | WG2 | WG3 | WG4 | WG5 | WG6 | WG7 | WG8 |
|------|------|------|------|------|------|------|------|------|
| LR1 | 1.00 | 1.00 | 1.00 | 1.00 | 1.00 | 1.00 | 1.00 | 1.00 |
| LR2 | 1.00 | 1.00 | 1.00 | 1.00 | 1.00 | 1.00 | 1.00 | 1.00 |
| LR3 | 1.00 | 1.00 | 1.00 | 1.00 | 1.00 | 1.00 | 1.00 | 1.00 |
| LR4 | 1.00 | 1.00 | 1.00 | 1.00 | 1.00 | 1.00 | 1.00 | 1.00 |
| LR5 | 1.00 | 1.00 | 1.00 | 1.00 | 1.00 | 1.00 | 0.95 | 1.00 |
| LR6 | 1.00 | 1.00 | 1.00 | 1.00 | 1.00 | 1.00 | 0.89 | 1.00 |
| LR7 | 1.00 | 1.00 | 1.00 | 1.00 | 1.00 | 1.00 | 0.92 | 1.00 |
| LR8 | 1.00 | 1.00 | 1.00 | 1.00 | 1.00 | 1.00 | 0.92 | 1.00 |
| LR9 | 1.00 | 1.00 | 1.00 | 1.00 | 1.00 | 1.00 | 0.92 | 1.00 |
| LR10 | 1.00 | 1.00 | 1.00 | 1.00 | 1.00 | 1.00 | 0.90 | 1.00 |
| LR11 | 1.00 | 1.00 | 1.00 | 1.00 | 1.00 | 1.00 | 0.93 | 1.00 |
| LR12 | 1.00 | 1.00 | 1.00 | 1.00 | 1.00 | 1.00 | 0.93 | 1.00 |
| LR13 | 1.00 | 1.00 | 1.00 | 1.00 | 1.00 | 1.00 | 0.93 | 1.00 |
| LR14 | 1.00 | 1.00 | 1.00 | 1.00 | 1.00 | 1.00 | 0.96 | 1.00 |
| LR15 | 1.00 | 1.00 | 1.00 | 1.00 | 1.00 | 1.00 | 0.97 | 1.00 |
| LR16 | 1.00 | 1.00 | 1.00 | 1.00 | 1.00 | 1.00 | 0.97 | 1.00 |
| LR17 | 1.00 | 1.00 | 1.00 | 1.00 | 1.00 | 1.00 | 0.97 | 1.00 |
| LR18 | 1.00 | 1.00 | 1.00 | 1.00 | 1.00 | 1.00 | 0.98 | 1.00 |
| LR19 | 1.00 | 1.00 | 1.00 | 1.00 | 1.00 | 1.00 | 0.98 | 1.00 |
| LR20 | 1.00 | 1.00 | 1.00 | 1.00 | 1.00 | 1.00 | 0.98 | 1.00 |
| LR21 | 1.00 | 1.00 | 1.00 | 1.00 | 1.00 | 1.00 | 0.99 | 1.00 |
| LR22 | 1.00 | 1.00 | 1.00 | 1.00 | 1.00 | 1.00 | 0.99 | 1.00 |
| LR23 | 1.00 | 1.00 | 1.00 | 1.00 | 1.00 | 1.00 | 0.99 | 1.00 |
| LR24 | 1.00 | 1.00 | 1.00 | 1.00 | 1.00 | 1.00 | 0.99 | 1.00 |
| LR25 | 1.00 | 1.00 | 1.00 | 1.00 | 1.00 | 1.00 | 0.98 | 1.00 |
| LR26 | 1.00 | 1.00 | 1.00 | 1.00 | 1.00 | 1.00 | 0.99 | 1.00 |
| LR27 | 1.00 | 1.00 | 1.00 | 1.00 | 1.00 | 1.00 | 0.98 | 1.00 |
| LR28 | 1.00 | 1.00 | 1.00 | 1.00 | 1.00 | 1.00 | 0.99 | 1.00 |
| LR29 | 1.00 | 1.00 | 1.00 | 1.00 | 1.00 | 1.00 | 0.98 | 1.00 |
| LR30 | 1.00 | 1.00 | 1.00 | 1.00 | 1.00 | 1.00 | 0.98 | 1.00 |
| LR31 | 1.00 | 1.00 | 1.00 | 1.00 | 1.00 | 1.00 | 0.99 | 1.00 |
| LR32 | 1.00 | 1.00 | 1.00 | 1.00 | 1.00 | 1.00 | 0.98 | 1.00 |
| LR33 | 1.00 | 1.00 | 1.00 | 1.00 | 1.00 | 1.00 | 0.98 | 1.00 |
| LR34 | 1.00 | 1.00 | 1.00 | 1.00 | 1.00 | 1.00 | 0.98 | 0.82 |
| LR35 | 1.00 | 1.00 | 1.00 | 1.00 | 1.00 | 1.00 | 0.99 | 0.63 |

3.2.3 Wave Spectra

Wave power spectra are computed applying Fast Fourier Transforms (FFT) to the measured free-surface elevation time series of each wave record with sampling frequency 20 Hz. Since WG7 and WG8 data are affected by changing runnel water level these data have been detrended using 20-s mean values before applying FFT. Matlab's `pwelch` function with a 600 point window overlap is used to obtain smooth one-sided wave frequency spectrum plots. Figure 3.6 shows the power spectral density $S (cm^2 s)$ as a function of frequency for several time series of the HR test recorded at WG1, WG7, and WG8. WG7 and WG8 were located at $x = 18.52$ and $19.46 m$, respectively, as shown in Figure 2.4. A similar compilation of results is presented in Figure 3.7 for the LR test. Panel columns represent the same WG location and panel rows represent the same test run. Runs have been chosen to indicate the different stages of spectral evolution. Each of the two figures compares the offshore (WG1) wave frequency spectra to the spectra measured at the WG7 and WG8 locations. The different spectral shapes are linked to the evolution of the ridge-runnel system and its effect on wave breaking and low-frequency wave generation, the frequency of waves overtopping over the ridge crest and the resulting wave motion in the runnel.

The offshore frequency spectrum remains essentially constant throughout each test (WG1) with a single peak at 0.39 Hz (red dotted vertical line) corresponding to the peak wave period $T_p = 2.57 s$. In general, WG7 and WG8 spectra show reduced peak density by one or two orders of magnitude compared to the offshore peak density. The peak frequency signature is still detectable during all runs except for HR9 (WG8) and LR34 (WG7 and WG8) where fewer waves actually reached the gauges located above SWL. The shift of the spectral peak to about 0.1 Hz observed to different degrees in all WG7 and WG8 panels also results from the fact that fewer incident waves reached the gauge location partly due to the ridge

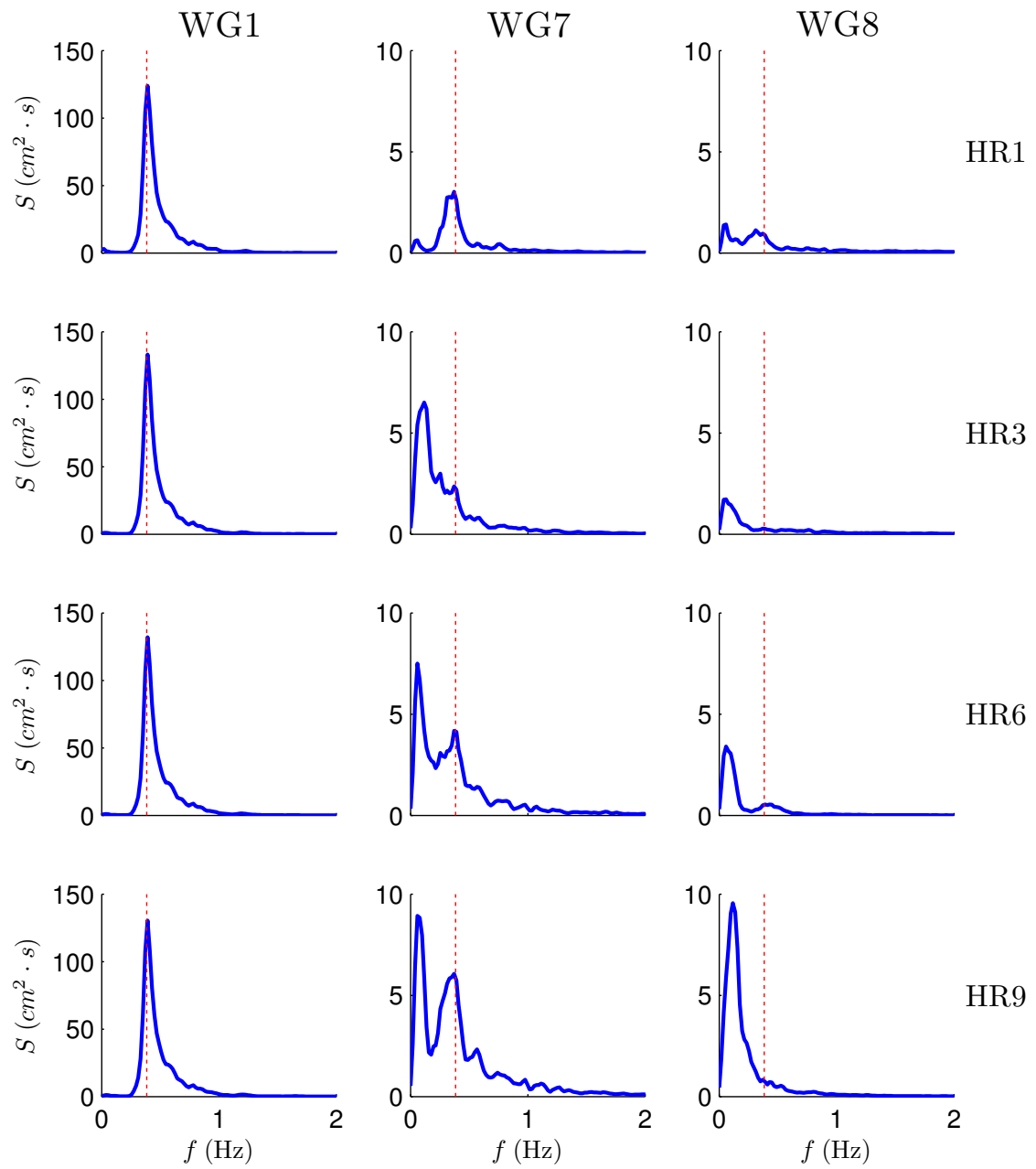


Figure 3.6: Measured power spectral density for HR test. Spectra are shown for 4 runs at the locations of WG1, WG7, and WG8.

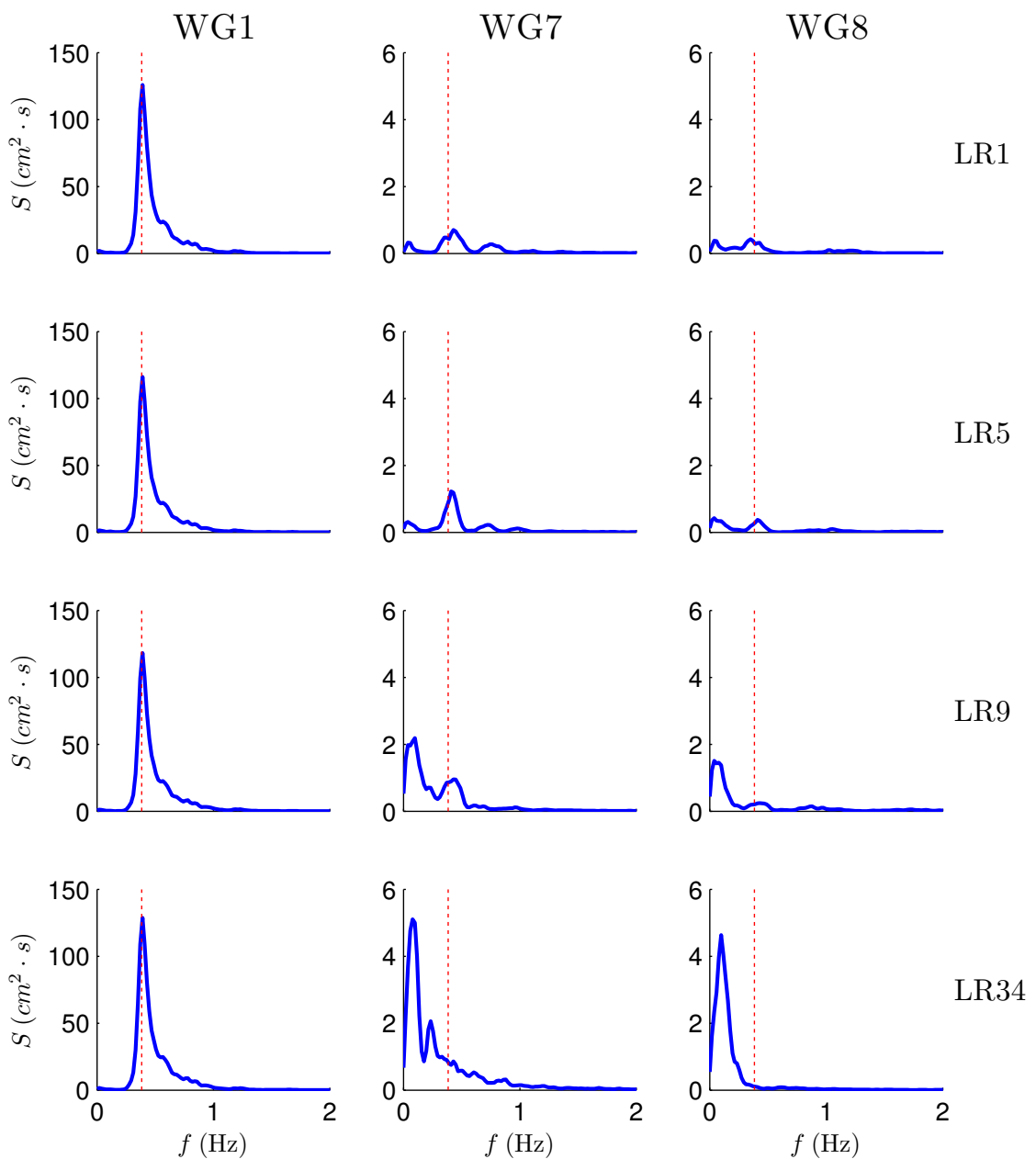


Figure 3.7: Measured power spectral density for LR test. Spectra are shown for 4 runs at the locations of WG1, WG7, and WG8.

blocking small waves and partly due to the landward attenuation of irregular wave runup.

The main difference between the HR and LR spectra is the speed at which the shift to lower frequencies occurs. For example, the WG7 spectrum during HR1 is similar to the WG7 spectrum at LR5 since in both cases the ridge crest reached the WG7 location (see Tables 3.2 and 3.3). Comparing the spectra of WG7 for HR9 and LR34, which are both close to the end of their respective tests, reveals noticeable differences between HR and LR test. While the HR9 spectrum still retains a good portion of the wave energy at the offshore peak frequency, the LR34 spectrum does not show a peak at that frequency. The difference may be explained by the relative location of WG7 with respect to SWL during those two runs. During HR9, WG7 was located below SWL, whereas during HR34 it was located above SWL. The distinctive features of the WG7 and WG8 measurements are highlighted in the following section.

3.2.4 Wet and Dry Gauges

The migrating ridge-runnel system shifts the location of the ponded water and the intermittently wet and dry zone of the profile. Wave gauges WG7 and WG8 fixed at their respective cross-shore locations allowed for tracking of free-surface elevation, runnel water level, and bottom profile elevation.

Figures 3.8 and 3.9 give an overview of the hydrodynamics and morphology changes encountered by WG7 (top panels) and WG8 (bottom panels) during the entire HR and LR tests. The horizontal axis is the test duration in seconds and the vertical axis is the elevation above SWL in meters. Measured free-surface elevation $\eta(t)$ is split up into wet duration and dry duration. The wet duration signal is shown as a dark blue fluctuating signal with integers denoting run numbers HR1-HR10 and LR1-LR35, respectively. The dry duration signal indicates the bottom elevation and is represented by green dots. The initial 20-s ramp-up period is removed from all

runs. Yellow diamonds represent the mean free-surface elevations during the wet duration in each run whose values are listed in Tables 3.8 and 3.9.

In order to place the dry duration measurements in perspective, the measured bottom elevation at each gauge location is plotted as red circles. Red lines interpolate profile measurements from the laser line scanner and dry duration elevations from the wave gauge records match well. Estimates for runnel water level (RWL) obtained by spline interpolation of $\eta(t)$ are presented as cyan colored dashed lines for WG7 and WG8. The spline boundary condition at $t = 0$ is set to zero since the initial RWL is equal to SWL. Rapid RWL increase is characteristic for the first run (Phase 1) in both HR and LR tests and is apparent in the WG7 and WG8 records.

For the HR test (Figure 3.8), RWL peaked in the middle of HR1 when the runnel was completely filled by wave overtopping. At this point the ridge crest elevation was already reduced to half its original height of 0.1 m and the ridge migrated onshore near WG7. Further ridge crest reduction lowered the RWL. After HR1, WG7 was on the seaward ridge slope. Starting in HR4, WG7 was submerged always with no dry duration. At the end of HR5 the runnel was filled in with sand (see Figure 3.2). This can be observed in the WG8 time series where the measured bottom elevations (red circles) match up with the gauge's measured dry duration (green dots). During HR6-HR8 multiple outliers in the WG8 record had to be removed, which explains the reduced wave peaks in those three runs. The outliers were caused by several high wave crests hitting the gauge.

The slower rate of morphological changes in the LR test lead to different data for WG7 and WG8 (Figure 3.9). RWL peaked at the end of LR2 since the ridge crest elevation actually increased slightly (5.5 mm) during LR2 (Table 3.3). WG7 was located in the ponded water area until the ridge crest moved past its location in LR5 during which the WG7 record included dry durations and $P_w = 0.95$ in Table 3.13. Once WG7 was situated on the seaward ridge slope, the profile lowering

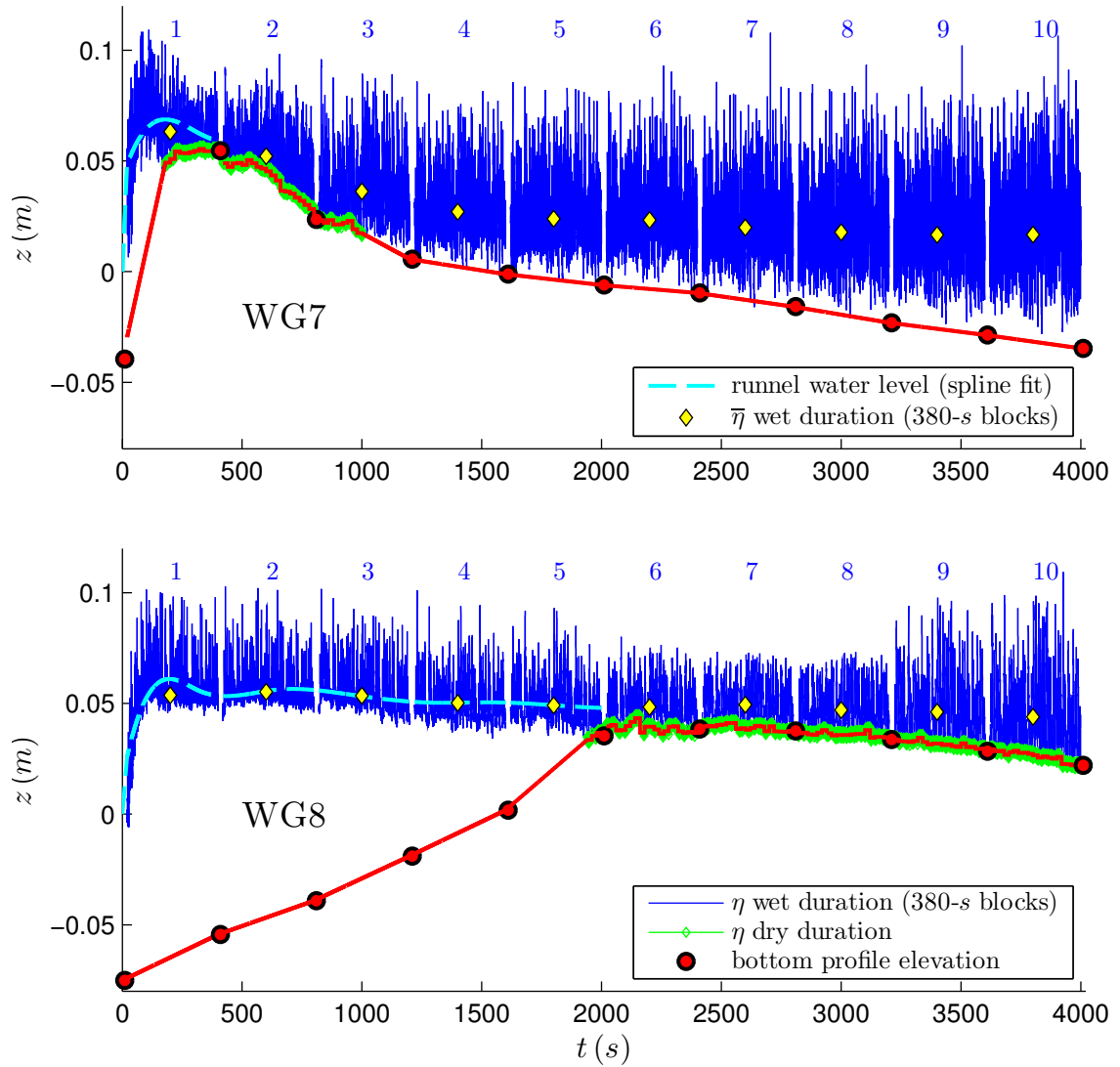


Figure 3.8: Measured free-surface elevation, runnel water level, and bottom elevation at WG7 ($x = 18.52$ m) and WG8 ($x = 19.46$ m) locations for 10 runs of HR test. Initially both gauges are located inside the runnel with water level equal to SWL. The initial 20-s ramp-up period in every run has been removed to create a gap between successive runs.

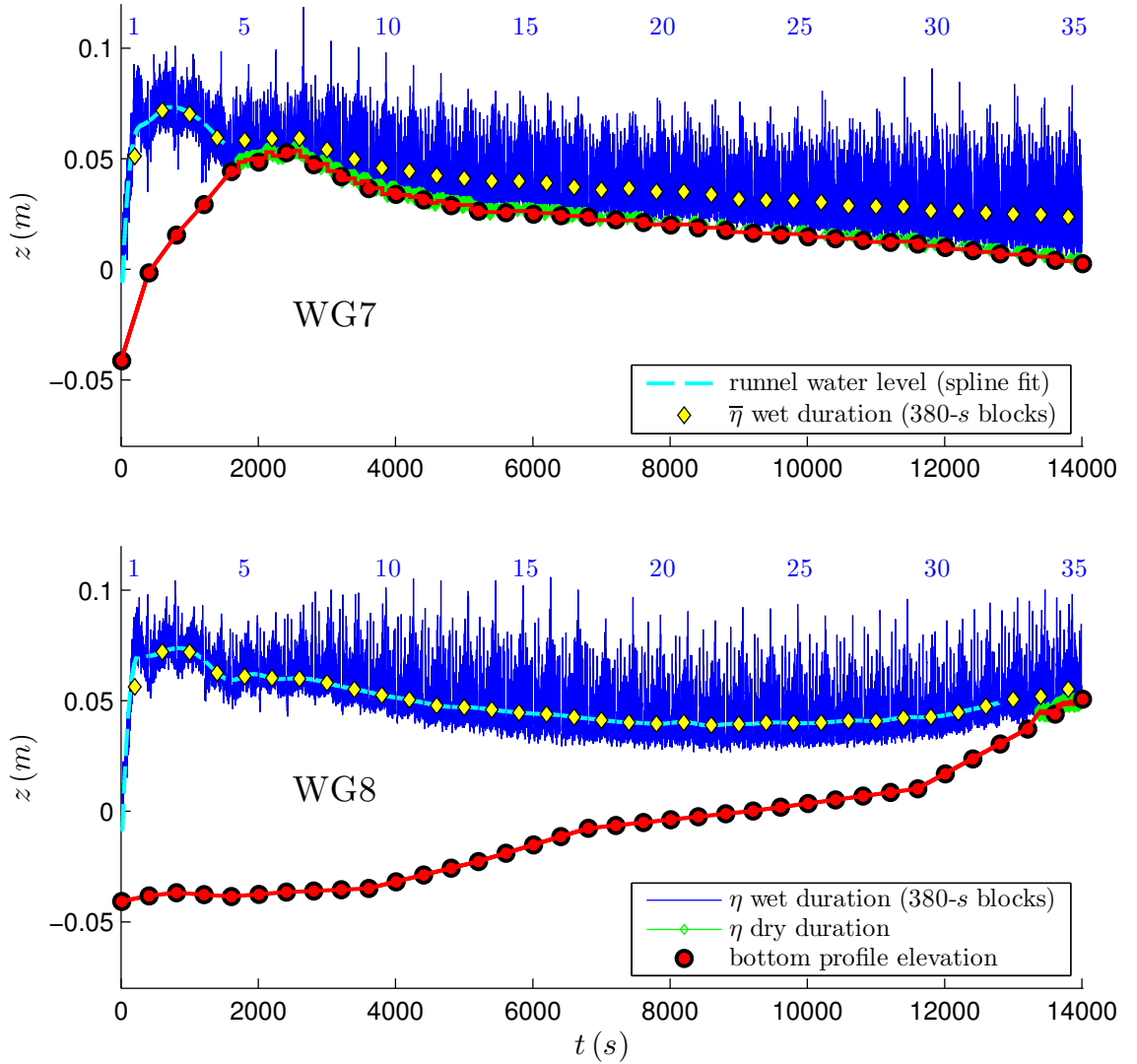


Figure 3.9: Measured free-surface elevation, runnel water level, and bottom elevation at WG7 ($x = 18.52\text{ m}$) and WG8 ($x = 19.46\text{ m}$) locations for 35 runs of LR test. Initially both gauges are located inside the runnel with water level equal to SWL. The initial 20-s ramp-up period in every run has been removed to create a gap between two successive runs.

was gradual until the end of LR test. The mean free-surface elevation $\bar{\eta}$ in the wet duration (yellow diamonds) shows two peaks for WG7. One in LR2 with the maximum RWL and one in LR7 with the gauge being at the ridge crest. WG8 was able to track the RWL until LR33 at the end of Phase 2 in Table 3.1.

In summary, the data of WG7 and WG8 combined with the profile data are useful in interpreting the strong interactions between the wave action and evolving bottom profile.

3.3 Velocity Measurements

Fluid velocity data was recorded using acoustic Doppler velocimeters (ADV). For the HR and LR tests two ADV sensors co-located with WG5 (ADV1) and WG8 (ADV2) were deployed in every run with sampling volumes positioned according to Table 2.3. ADV1 measured three velocity components seaward of the ridge-runnel system as shown in Figure 2.4. Its elevation above the local bottom guaranteed for measurements well outside the bottom boundary layer with enough clearance to prevent possible scouring near the probe tip. In addition, the distance from the free surface minimized the possible effects of entrained air bubbles on the measurements. ADV2 was situated near the landward end of the runnel to obtain velocities in the runnel and in front of the vertical wall after the runnel disappeared. The vertical elevation of its side-looking probe tip was adapted to the changing bottom elevation to maintain a sufficient level of clearance ($> 1\text{ cm}$) from the sand bottom. ADV locations were chosen according to measured profile changes and RWL during a series of preliminary tests (Gralher, 2010) so as to avoid burial under sand during a run. The chosen measurement locations are assumed to give a reasonable representation of the depth-averaged velocities in shallow water.

Since the ridge-runnel migration speed was significantly slower in the LR test than in the HR test, an additional Nortek Vectrino ADV was co-located with WG7 to measure fluid velocities in the vicinity of the ridge crest. As seen in the top panel of Figure 3.9 this WG7 position was located in the intermittently wet and dry zone for most of the runs. The measurements were affected by bubble entrainment and emergence of the side-looking probe tip. Nevertheless, some useful velocity information has been extracted from the Vectrino time series.

3.3.1 3D ADV

The mean and standard deviation of the measured cross-shore (u), along-shore (v), and vertical (w) components of the velocity field for the 10 runs in the

HR test are given in Table 3.14. The mean and standard deviation of only the measured cross-shore and alongshore components are presented in Table 3.15 for the 35 runs in the LR test, since the vertical component was not measured. The cross-shore velocity component u is dominant as expected in this two-dimensional wave flume experiment. The mean cross-shore velocity \bar{u} is always negative indicating the presence of an offshore return (undertow) current as observed in previous velocity measurements in the same wave flume. Kobayashi et al. (2005) showed vertical distributions of the measured mean cross-shore velocity \bar{u} at various locations under similar conditions. The measured vertical variations of \bar{u} were not very large under the irregular waves in their experiment.

In the HR test the measured values for \bar{u} ranged from -4.72 (HR5) to -3.65 cm/s (HR1) with standard deviations between 16.96 (HR5) and 18.03 cm/s (HR1). The mean cross-shore velocities \bar{u} were slightly larger in magnitude for the LR test with the smaller water depth. Values for \bar{u} ranged from -5.14 (LR12) to -3.68 cm/s (LR25) with standard deviations, σ_u , between 15.48 (LR30) and 17.31 cm/s (LR1). The values for the longshore turbulent velocity and vertical wave-induced and turbulent velocity were one order of magnitude smaller than the cross-shore velocity (Tables 3.14 and 3.15). Averages of the velocity parameters for the entire test are given at the bottom of the two tables. The differences of \bar{u} and σ_u for the two tests are similar in magnitude to the variations among the runs in each test.

Table 3.14: Velocity (cm/s) parameters measured with 3D ADV ($x = 14.9\text{ m}$, $z = -2d/3$) for 10 runs of HR test.

| Run | \bar{u} | σ_u | \bar{v} | σ_v | \bar{w} | σ_w |
|------|-----------|------------|-----------|------------|-----------|------------|
| HR1 | -3.65 | 18.03 | -0.59 | 3.17 | -0.36 | 3.42 |
| HR2 | -4.28 | 17.68 | -0.35 | 2.99 | -0.16 | 3.54 |
| HR3 | -4.59 | 16.96 | -0.30 | 2.92 | -0.48 | 3.66 |
| HR4 | -3.91 | 17.19 | 0.10 | 2.88 | -0.22 | 3.26 |
| HR5 | -4.72 | 16.96 | -0.79 | 2.70 | -0.47 | 2.94 |
| HR6 | -4.03 | 17.05 | 0.22 | 2.85 | -0.61 | 3.23 |
| HR7 | -3.82 | 17.24 | 0.18 | 2.83 | -0.34 | 3.20 |
| HR8 | -4.88 | 17.29 | -0.25 | 2.78 | -0.44 | 2.96 |
| HR9 | -4.39 | 17.50 | -0.30 | 3.07 | -0.28 | 3.15 |
| HR10 | -4.36 | 17.64 | -0.50 | 2.83 | -0.36 | 3.62 |
| Avg. | -4.26 | 17.35 | -0.26 | 2.90 | -0.37 | 3.30 |

Table 3.15: Velocity (cm/s) parameters measured with 3D ADV ($x = 14.9\ m$, $z = -2d/3$) for 35 runs of LR test.

| Run | \bar{u} | σ_u | \bar{v} | σ_v |
|------|-----------|------------|-----------|------------|
| LR1 | -4.95 | 17.31 | -0.52 | 3.34 |
| LR2 | -4.76 | 16.79 | -1.38 | 2.94 |
| LR3 | -4.94 | 16.42 | -0.13 | 2.72 |
| LR4 | -4.56 | 16.37 | -0.34 | 2.91 |
| LR5 | -4.34 | 16.11 | -0.23 | 2.92 |
| LR6 | -5.03 | 16.03 | -0.07 | 3.07 |
| LR7 | -4.56 | 15.86 | -0.22 | 3.04 |
| LR8 | -4.92 | 15.77 | -0.39 | 2.84 |
| LR9 | -4.55 | 15.86 | -0.19 | 2.78 |
| LR10 | -4.62 | 15.59 | -0.46 | 2.88 |
| LR11 | -4.46 | 15.71 | -0.79 | 2.80 |
| LR12 | -5.14 | 15.70 | -0.21 | 3.01 |
| LR13 | -4.47 | 15.69 | -0.07 | 2.92 |
| LR14 | -4.19 | 15.95 | 0.04 | 3.11 |
| LR15 | -4.35 | 15.96 | -0.52 | 2.94 |
| LR16 | -4.63 | 15.74 | -0.80 | 2.86 |
| LR17 | -4.60 | 15.92 | -0.05 | 2.92 |
| LR18 | -4.23 | 15.67 | -0.10 | 2.75 |
| LR19 | -4.18 | 15.79 | -0.37 | 2.83 |
| LR20 | -4.42 | 15.84 | -0.52 | 2.89 |
| LR21 | -4.77 | 15.90 | -0.45 | 2.80 |
| LR22 | -4.21 | 15.88 | -0.27 | 2.81 |
| LR23 | -3.73 | 15.93 | 0.13 | 2.84 |
| LR24 | -4.09 | 15.74 | -0.61 | 2.93 |
| LR25 | -3.68 | 16.01 | -0.28 | 2.97 |
| LR26 | -4.02 | 15.96 | -0.76 | 3.05 |
| LR27 | -4.23 | 15.86 | -0.09 | 2.87 |
| LR28 | -4.92 | 15.60 | -0.31 | 2.79 |
| LR29 | -4.13 | 15.66 | -0.14 | 2.81 |
| LR30 | -4.61 | 15.48 | 0.10 | 2.87 |
| LR31 | -4.47 | 15.54 | -0.08 | 2.78 |
| LR32 | -4.09 | 15.69 | 0.10 | 2.96 |
| LR33 | -4.79 | 15.73 | -0.02 | 2.88 |
| LR34 | -4.47 | 15.59 | 0.13 | 2.94 |
| LR35 | -4.15 | 15.78 | -0.15 | 2.86 |
| Avg. | -4.47 | 15.90 | -0.29 | 2.90 |

3.3.2 2D ADV

The 2D ADV (ADV2) was deployed in this experiment to obtain information on horizontal velocity components inside the runnel or in front of the wall. Tables 3.16 and 3.17 list the local bottom elevation (z_b) at the beginning of each run, the vertical coordinate of the measuring volume (z_{ADV}), the fraction of submergence duration (D_w), and the cross-shore and longshore velocity parameters, \bar{u} , σ_u , \bar{v} , and σ_v for each run of the HR and LR tests. The submergence fraction D_w is similar to the wet probability P_w given by Equation (3.3) where P_w is based on the submergence of the local bottom.

Table 3.16: Location of local bottom (z_b), location of instrument measuring volume (z_{ADV}), submergence fraction (D_w) and velocity parameters measured with 2D ADV ($x = 19.46\text{ m}$) for 10 runs of HR test.

| Run | z_b (cm) | z_{ADV} (cm) | D_w (-) | \bar{u} (cm/s) | σ_u (cm/s) | \bar{v} (cm/s) | σ_v (cm/s) |
|------|---------------|-------------------|--------------|---------------------|----------------------|---------------------|----------------------|
| HR1 | -5.44 | -3.76 | 1.00 | 3.00 | 7.07 | -1.64 | 2.71 |
| HR2 | -3.92 | -2.72 | 1.00 | 0.67 | 5.71 | -0.48 | 2.09 |
| HR3 | -1.90 | -0.92 | 1.00 | -1.30 | 6.71 | -1.50 | 3.13 |
| HR4 | 0.18 | 1.10 | 1.00 | -0.58 | 8.18 | 0.33 | 3.39 |
| HR5 | 3.54 | 4.18 | 0.78 | 0.05 | 11.76 | 0.44 | 3.69 |
| HR6 | 3.85 | 4.54 | 0.58 | 3.18 | 26.05 | 0.56 | 4.04 |
| HR7 | 3.75 | 4.85 | 0.51 | 4.90 | 27.36 | 0.09 | 5.05 |
| HR8 | 3.37 | 4.75 | 0.43 | 8.62 | 25.85 | -0.11 | 5.21 |
| HR9 | 2.84 | 4.37 | 0.49 | 5.01 | 26.66 | 0.47 | 4.98 |
| HR10 | 2.20 | 3.84 | 0.57 | 2.28 | 28.00 | 0.26 | 5.03 |
| Avg. | 0.85 | 2.02 | 0.74 | 2.58 | 17.34 | -0.16 | 3.93 |

The vertical elevation of the measurement volume was approximately 1/2 of

the runnel water depth below the RWL. After the runnel disappearance z_{ADV} was about 1 cm above the local sand bottom at the end of each run (z_b) as anticipated from the preliminary tests. During these runs the probe was only intermittently submerged under waves rushing up and down the beach face. Velocity data recorded during times when the synchronized WG7 free-surface elevation fell below z_{ADV} were eliminated. The parameter D_w denotes the fraction of data points of the entire 380-s time series for which the measuring volume was submerged. D_w ranges from unity for complete submergence to zero for complete emergence. Statistical velocity parameters are only computed for values recorded during the submergence. D_w is used to interpret the statistical velocity results because $D_w < 1$ implies no velocity measurement in the zone below z_{ADV} even when water was present above the local bottom.

For HR the mean cross-shore and longshore velocities measured inside the runnel (HR1-HR4) fluctuated between positive (onshore) and negative (offshore) with relatively small magnitudes (possibly within the measurement uncertainty for \bar{u} and \bar{v}) compared to ADV1. The mean velocity \bar{u} was affected by wave overtopping over the ridge crest and onshore overtopping flow over the back wall as well as offshore return flow over the ridge. The standard deviations remained below 10 cm/s (σ_u) and 4 cm/s (σ_v), respectively (Table 3.16). Only HR1 indicated a relatively strong mean onshore current ($\bar{u} = 3 \text{ cm/s}$), possibly related to the initial water ponding in the runnel during the first run (Table 3.1). As the overtopping flow rate decreased after the runnel was filled up, the mean cross-shore velocity inside the runnel became very small.

After the runnel disappearance in the HR test, the ADV was located about 1 cm above the beach surface. The wet fraction D_w decreased to approximately 50%. The mean velocity \bar{u} became positive (onshore) and increased significantly to a maximum in HR8 of 8.62 cm/s. The standard deviation, σ_u increased to a

Table 3.17: 2D ADV velocity parameters ($x = 19.46$ m) for 35 runs of LR test.

| Run | z_b (cm) | z_{ADV} (cm) | D_w (-) | \bar{u} (cm/s) | σ_u (cm/s) | \bar{v} (cm/s) | σ_v (cm/s) |
|------|---------------|-------------------|--------------|---------------------|----------------------|---------------------|----------------------|
| LR1 | -3.82 | -1.08 | 1.00 | 0.00 | 3.43 | -0.99 | 1.68 |
| LR2 | -3.68 | -0.82 | 1.00 | -0.16 | 2.55 | -0.67 | 0.92 |
| LR3 | -3.77 | -0.47 | 1.00 | -0.18 | 2.34 | -0.65 | 0.85 |
| LR4 | -3.85 | -0.40 | 1.00 | -0.21 | 2.64 | -0.71 | 1.52 |
| LR5 | -3.76 | -0.40 | 1.00 | -0.06 | 2.82 | -1.14 | 1.15 |
| LR6 | -3.66 | -0.40 | 1.00 | 0.06 | 2.68 | -1.07 | 1.38 |
| LR7 | -3.60 | -0.40 | 1.00 | -0.31 | 3.08 | -0.50 | 0.91 |
| LR8 | -3.55 | -0.40 | 1.00 | -0.40 | 3.10 | -1.13 | 1.11 |
| LR9 | -3.49 | -0.40 | 1.00 | -0.47 | 3.17 | -1.01 | 1.24 |
| LR10 | -3.19 | -0.40 | 1.00 | -0.43 | 2.99 | -0.67 | 1.24 |
| LR11 | -2.88 | -0.40 | 1.00 | -0.64 | 3.12 | 0.52 | 1.69 |
| LR12 | -2.58 | -0.29 | 1.00 | -0.68 | 3.14 | 0.49 | 1.90 |
| LR13 | -2.27 | -0.29 | 1.00 | -0.80 | 3.08 | -0.69 | 2.02 |
| LR14 | -1.90 | 0.71 | 1.00 | -0.61 | 3.44 | -1.90 | 2.03 |
| LR15 | -1.52 | 0.71 | 1.00 | 0.07 | 3.62 | -1.47 | 2.32 |
| LR16 | -1.15 | 0.71 | 1.00 | 0.02 | 3.60 | -1.17 | 2.21 |
| LR17 | -0.77 | 0.71 | 1.00 | -0.23 | 3.67 | -1.36 | 2.21 |
| LR18 | -0.64 | 2.21 | 1.00 | -0.14 | 4.27 | -1.39 | 2.60 |
| LR19 | -0.51 | 2.21 | 1.00 | -0.57 | 4.05 | -0.65 | 1.92 |
| LR20 | -0.38 | 2.21 | 1.00 | -0.44 | 4.54 | -0.78 | 2.30 |
| LR21 | -0.25 | 2.21 | 1.00 | -0.86 | 4.63 | -0.20 | 2.64 |
| LR22 | -0.12 | 2.21 | 1.00 | -0.82 | 4.71 | -0.79 | 2.99 |
| LR23 | 0.02 | 2.21 | 1.00 | -0.95 | 5.09 | -0.89 | 2.70 |
| LR24 | 0.18 | 2.21 | 1.00 | -0.24 | 4.98 | -0.41 | 2.71 |
| LR25 | 0.35 | 2.21 | 1.00 | -0.46 | 5.27 | 0.06 | 2.88 |
| LR26 | 0.52 | 2.21 | 1.00 | -0.76 | 5.26 | -0.10 | 3.32 |
| LR27 | 0.68 | 2.21 | 1.00 | -0.66 | 5.47 | -0.68 | 2.71 |
| LR28 | 0.85 | 2.21 | 1.00 | -0.79 | 5.43 | 0.12 | 3.16 |
| LR29 | 1.02 | 2.21 | 1.00 | -0.86 | 5.68 | -0.33 | 3.01 |
| LR30 | 1.69 | 2.71 | 1.00 | -1.10 | 6.08 | 0.07 | 3.47 |
| LR31 | 2.37 | 2.71 | 1.00 | -1.24 | 6.17 | 0.52 | 3.35 |
| LR32 | 3.04 | 3.41 | 1.00 | -0.88 | 7.02 | 0.09 | 2.63 |
| LR33 | 3.72 | 4.41 | 0.83 | 0.40 | 15.06 | 0.16 | 3.86 |
| LR34 | 4.39 | 4.41 | 0.97 | -1.27 | 15.25 | 0.32 | 3.41 |
| LR35 | 5.07 | 5.91 | 0.23 | -4.27 | 21.38 | -0.01 | 4.90 |
| Avg. | -0.78 | 1.34 | 0.97 | -0.60 | 5.22 | -0.54 | 2.31 |

value of 28 cm/s in HR10. Wave uprush and downrush on the beach face occurred for $D_w < 1$. The uprush portion of the fluid velocity may have been measured more frequently because the downrush was mostly associated with very small water depths. In addition, wave overtopping of the wall reduced the amount of water contributing to downrush. These onshore velocities may have contributed to the measured net onshore sediment transport in this test.

Velocities in the runnel during LR were easier to measure due to the slower morphological changes. Table 3.17 shows that ADV2 was submerged inside the runnel during runs LR1-LR32 ($D_w = 1$). For most of these runs \bar{u} was slightly negative with magnitudes rarely exceeding 1 cm/s . These low negative velocities inside the runnel may be related to a return flow inside the runnel because no wave overtopping of the wall occurred. The standard deviation σ_u remained fairly low between 2.34 and 7.02 cm/s during LR1-LR32. The longshore velocities were relatively small as was the case with the 3D ADV.

For runs LR33-LR35 ($D_w < 1$), ADV2 was not inside the runnel any more and the values of \bar{u} and σ_u changed in manners similar to the HR test. However, contrary to HR, the mean cross-shore velocity in the last two LR runs was negative, indicating offshore return flow in front of the vertical wall with no overtopping.

3.3.3 Vectrino

The Vectrino was only used during the LR test. Its cross-shore position remained constant next to WG7 while its vertical position was adjusted with respect to the changing sand bottom. The instrument recorded high frequency (200 Hz) 3D velocity data in the vicinity of the migrating ridge crest. The extremely small water depth during instrument submergence and the extended dry durations made the data analysis tedious. The measured vertical velocity (w) in the small water depth was found to be unreliable and is excluded in the following. Nevertheless, valuable information on velocity statistics could be extracted from the measurements during the 35 LR wave runs.

Table 3.18 lists the bottom and measurement volume elevation, submergence fraction, and mean and standard deviation of the horizontal velocity components. In addition, the measurement fraction D_m is introduced. This parameter supplements the fraction D_w and is defined as the fraction of data points with reliable measurements among the entire data points in each time series. By definition $D_m < D_w$. Since the Vectrino recorded at a 10 times higher frequency than ADV1 and ADV2 with a smaller measuring volume, it was more susceptible to outliers caused by entrained bubbles. However, these outliers were easier to detect due to their apparent noise-like signature as shown later in this section. D_m was calculated using the remaining velocity data points after all outliers were eliminated. Only the reliable velocity data were used to compute the velocity statistics presented in Table 3.18.

D_w was less than unity in LR1 due to the initial vertical position of the Vectrino above RWL=SWL. At the end of LR4 z_{ADV} was practically level with the ridge crest and D_w decreased from unity during LR2 and LR3. The length of the dry durations increased as the ridge migrated past WG7, resulting in the noticeable reduction of D_w . The percentage of useful data (D_m) dropped to 10%

Table 3.18: Vectrino velocity parameters ($x = 18.52$ m) for 35 runs of LR test.

| Run | z_b (cm) | z_{ADV} (cm) | D_w (-) | D_m (-) | \bar{u} (cm/s) | σ_u (cm/s) | \bar{v} (cm/s) | σ_v (cm/s) |
|------|---------------|-------------------|--------------|--------------|---------------------|----------------------|---------------------|----------------------|
| LR1 | -0.2 | 1.9 | 0.89 | 0.78 | -0.1 | 6.3 | 2.0 | 3.5 |
| LR2 | 1.5 | 2.8 | 1.00 | 0.91 | -0.7 | 5.3 | 1.3 | 2.7 |
| LR3 | 2.9 | 4.5 | 1.00 | 0.83 | -0.7 | 6.2 | 0.4 | 2.5 |
| LR4 | 4.4 | 4.9 | 0.94 | 0.61 | -2.0 | 7.6 | -0.9 | 2.8 |
| LR5 | 4.8 | 5.4 | 0.81 | 0.64 | -4.6 | 9.0 | 0.8 | 2.8 |
| LR6 | 5.3 | 5.8 | 0.52 | 0.35 | -5.4 | 13.0 | 0.3 | 3.2 |
| LR7 | 4.7 | 6.3 | 0.23 | 0.14 | -6.2 | 24.7 | 1.1 | 4.6 |
| LR8 | 4.2 | 5.7 | 0.23 | 0.10 | -3.8 | 26.8 | 0.0 | 5.4 |
| LR9 | 3.6 | 5.2 | 0.28 | 0.12 | 2.8 | 20.6 | 0.0 | 5.0 |
| LR10 | 3.4 | 4.6 | 0.37 | 0.28 | -7.1 | 23.5 | -0.5 | 5.3 |
| LR11 | 3.1 | 4.6 | 0.32 | 0.22 | 0.1 | 22.1 | -1.7 | 5.9 |
| LR12 | 2.9 | 4.1 | 0.46 | 0.32 | -4.5 | 16.9 | -2.6 | 5.8 |
| LR13 | 2.6 | 4.1 | 0.41 | 0.31 | -1.6 | 18.6 | -3.0 | 5.8 |
| LR14 | 2.6 | 3.6 | 0.58 | 0.46 | -5.3 | 22.5 | -3.5 | 5.4 |
| LR15 | 2.5 | 3.6 | 0.62 | 0.51 | -6.5 | 20.9 | -3.5 | 5.2 |
| LR16 | 2.4 | 3.6 | 0.57 | 0.44 | -6.0 | 20.6 | -2.3 | 5.1 |
| LR17 | 2.4 | 3.6 | 0.48 | 0.37 | -2.3 | 21.5 | -0.4 | 5.4 |
| LR18 | 2.2 | 3.4 | 0.52 | 0.42 | -3.0 | 23.1 | 1.0 | 5.2 |
| LR19 | 2.1 | 3.2 | 0.63 | 0.52 | -5.7 | 19.2 | -0.6 | 4.6 |
| LR20 | 2.0 | 3.2 | 0.56 | 0.45 | -4.3 | 19.5 | -1.9 | 5.0 |
| LR21 | 1.9 | 3.2 | 0.54 | 0.43 | -3.3 | 19.5 | -1.6 | 5.1 |
| LR22 | 1.8 | 3.2 | 0.49 | 0.39 | -2.0 | 21.8 | -1.8 | 5.4 |
| LR23 | 1.6 | 3.2 | 0.39 | 0.29 | 0.5 | 21.7 | -1.5 | 5.6 |
| LR24 | 1.6 | 2.6 | 0.65 | 0.52 | -5.9 | 20.3 | -1.7 | 5.2 |
| LR25 | 1.5 | 2.6 | 0.64 | 0.52 | -5.3 | 21.1 | -1.6 | 5.3 |
| LR26 | 1.4 | 2.5 | 0.68 | 0.53 | -5.8 | 19.3 | -2.2 | 5.9 |
| LR27 | 1.3 | 2.5 | 0.59 | 0.47 | -4.2 | 20.7 | -0.6 | 5.4 |
| LR28 | 1.2 | 2.5 | 0.58 | 0.45 | -3.8 | 22.0 | -0.7 | 5.3 |
| LR29 | 1.1 | 2.2 | 0.69 | 0.54 | -7.6 | 20.9 | -0.2 | 5.2 |
| LR30 | 1.0 | 2.1 | 0.62 | 0.48 | -5.4 | 18.4 | -0.4 | 5.2 |
| LR31 | 0.8 | 2.1 | 0.62 | 0.47 | -7.9 | 20.3 | -0.4 | 5.3 |
| LR32 | 0.7 | 1.8 | 0.70 | 0.53 | -7.7 | 17.7 | -0.0 | 4.9 |
| LR33 | 0.6 | 1.8 | 0.68 | 0.49 | -7.4 | 17.7 | 0.7 | 4.4 |
| LR34 | 0.4 | 1.8 | 0.66 | 0.49 | -9.0 | 21.3 | -0.3 | 5.0 |
| LR35 | 0.3 | 1.8 | 0.62 | 0.45 | -9.4 | 22.8 | 0.9 | 4.6 |
| Avg. | 2.2 | 3.5 | 0.59 | 0.45 | -4.32 | 18.7 | -0.7 | 4.8 |

during LR8 when the Vectrino was directly above the ridge crest. As the ridge crest moved further onshore, z_{ADV} was lowered and D_m increased again to values around 50% at the end of LR. The mean cross-shore velocity was predominantly directed offshore with values ranging from 0.5 to -9.4 cm/s . The largest offshore currents were detected at the end of the LR test after the runnel disappeared. σ_u increased from values below 10 cm/s with the Vectrino situated landward of the ridge crest to values in excess of 20 cm/s seaward of the ridge crest. The longshore mean velocity component was significantly lower than its cross-shore counterpart for most runs. The longshore turbulent velocity represented by σ_v remained fairly constant around 5 cm/s .

Figure 3.10 shows measured time series of free-surface elevation η and cross-shore velocity u at the locations of WG5, WG7, and WG8 during LR1. Free-surface elevation is displayed as magenta lines with corresponding ordinates on the left side of each panel. Dark blue lines denote velocity measurements after outliers are filtered out. ADV1 (top panel) and ADV2 (bottom panel) were submerged during the entire run with no outliers. The Vectrino outliers are shown in the middle panel as cyan colored lines. The bulk of the outliers occurs during the runnel filling when the Vectrino was above the RWL. The dashed magenta line in the middle panel denotes z_{ADV} of the Vectrino in LR1. The velocity data were regarded to be unreliable for the duration of η_7 at WG7 being lower than the Vectrino z_{ADV} .

The cross-shore velocity measured by ADV1 is in phase with the free-surface elevation. The ridge-runnel system creates a different situation for the Vectrino and ADV2 measurements in the very shallow water. Figure 3.11 displays a 30-s synchronized window of the cross-shore velocity (top panel) and the WG7 free-surface elevation η_7 (bottom panel) during LR10. Only the dark blue velocity data passed the applied quality control and is used for the analysis for Table 3.18. Three filters make up the quality control. The first is represented by the dashed blue

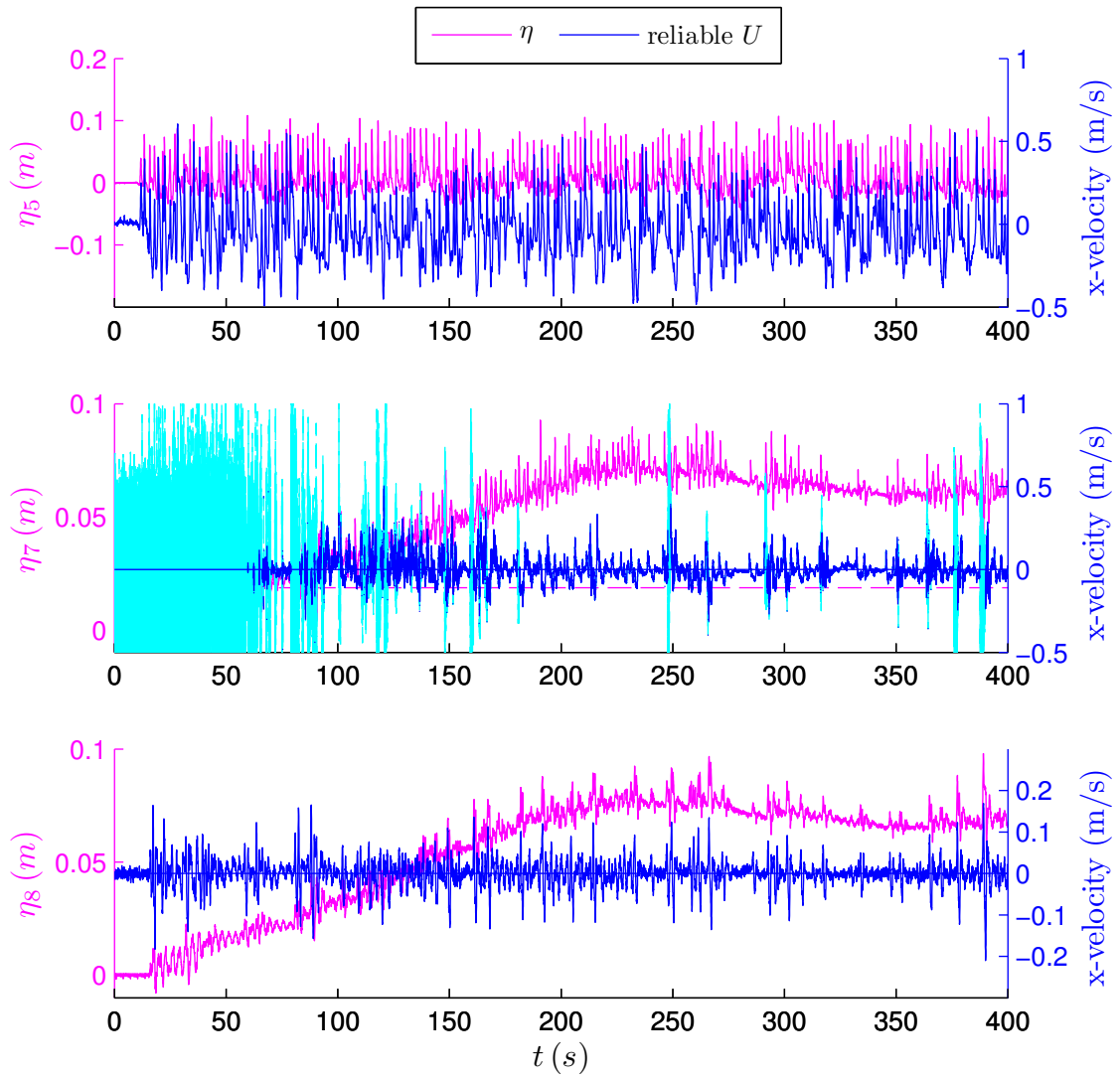


Figure 3.10: Measured free-surface elevation (magenta) and reliable cross-shore velocity component (blue) at the three locations of WG5 (top), WG7 (middle) and WG8 (bottom) during LR1. The WG7 and WG8 records show the increase in RWL. Velocity outliers are cyan colored and occur mostly during the initial filling of the tunnel when the velocity probe was not submerged.

cut-off line in the bottom panel. Velocity data recorded during the free-surface elevation at that location being below the elevation of the probe is filtered out. The data is also passed through two acceleration filters testing for absolute velocity gradients between individual data points and between adjacent groups of data points (red lines). If the group value lies above a specified cut-off (dashed red line) the respective data points are filtered out. It should be noted that these two acceleration filters are fairly arbitrary but appear to remove the visually detected outliers for this velocity data set.

The remaining data still retains the characteristic signature of overtopping flow and return current over the ridge. In Figure 3.11 several wave overtopping (onshore velocity) events were followed by the offshore return flow out of the runnel (negative velocity in the top panel) where the return flow in the small water depth tends to cause emergence of the velocity probe.

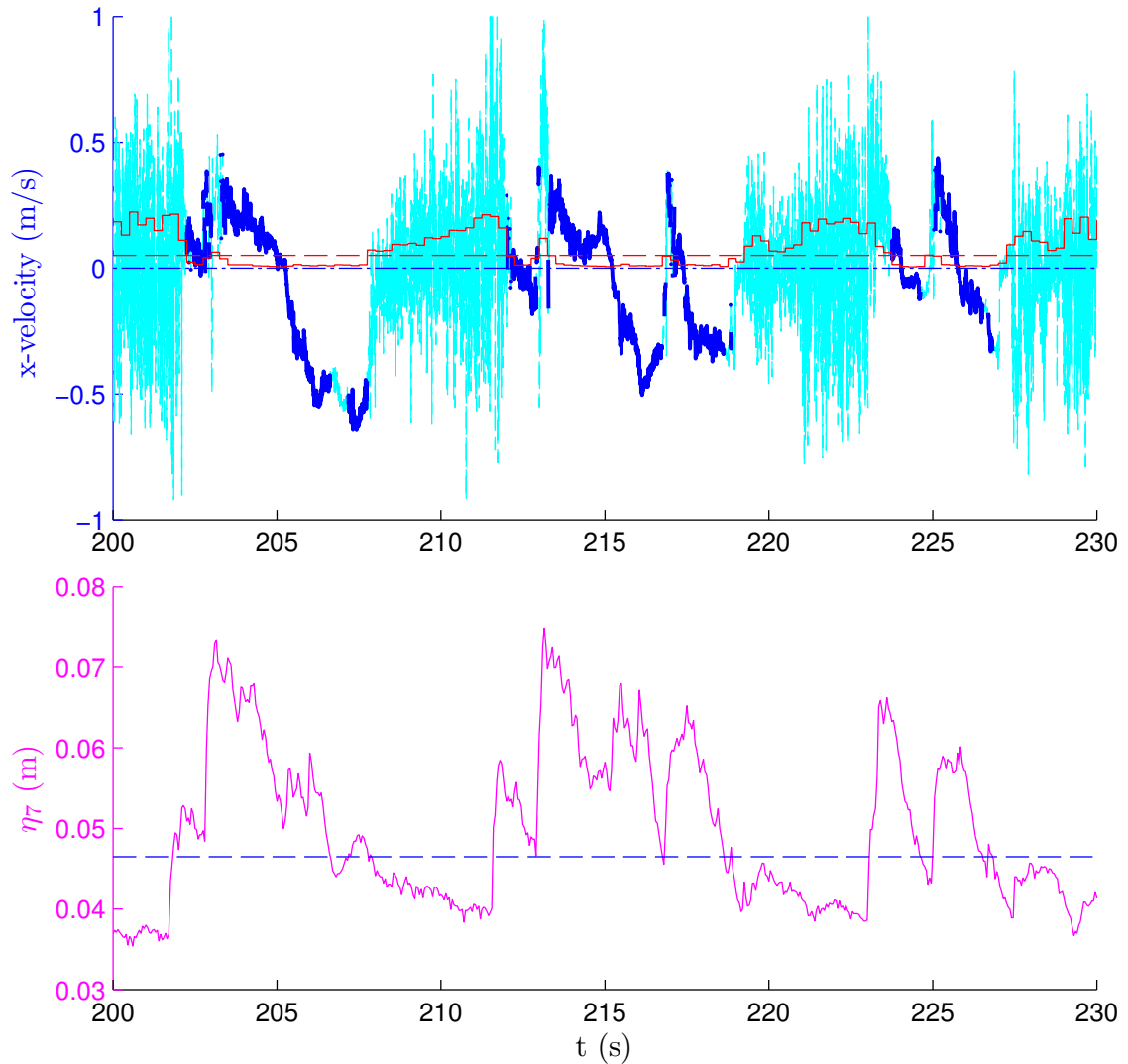


Figure 3.11: Example (30 s) of measured Vectrino cross-shore velocity (top) and WG7 free-surface elevation (bottom) during LR10. After filtering is applied, only the velocity data colored in dark-blue are retained for statistical analysis. The dashed red line is the cut-off for the acceleration filter (solid red line). The blue dashed line in the bottom panel denotes the Vectrino z_{ADV} . If η_7 drops below this line, the corresponding cross-shore velocity is discarded.

Chapter 4

NUMERICAL MODEL CSHORE

This chapter describes the main components of the time-averaged cross-shore model CSHORE (Kobayashi et al., 2010). The following sections explain the mathematical formulation of the combined wave and current model in CSHORE and the extension of the computation domain to the wet and dry zone of the bottom profile using a probabilistic approach. Furthermore, the sediment transport formulas used in CSHORE are presented. Ponded water in runnels affects hydrodynamics and sediment transport. The new CSHORE version includes the option to incorporate the ponded water effects if a ridge-runnel system is present.

4.1 Combined Wave and Current Model in the Wet Zone

The time-averaged cross-shore numerical model developed by Kobayashi et al. (2009) is extended here to include wave and current interactions in order to account for the onshore water flux due to wave overtopping. In the following, use is made of linear wave and current theory (e.g., Mei, 1989). The impermeable bottom elevation $z_b(x)$, the still water level S above $z = 0$, and the measured values of T_p , $\bar{\eta}$, and σ_η at $x = 0$ outside the surf zone for each test are specified as input. The still water level was constant and $S = 0$ in the present experiment. The computation marches landward to predict the cross-shore variations of $\bar{\eta}$ and σ_η and the wave overtopping rate q_m at the landward end of the computation domain as shown in Figure 4.1. The landward limit of the wet zone is the upper limit of the mean water level (MWL) located at x_r . The wet and dry zone is explained in the next section.

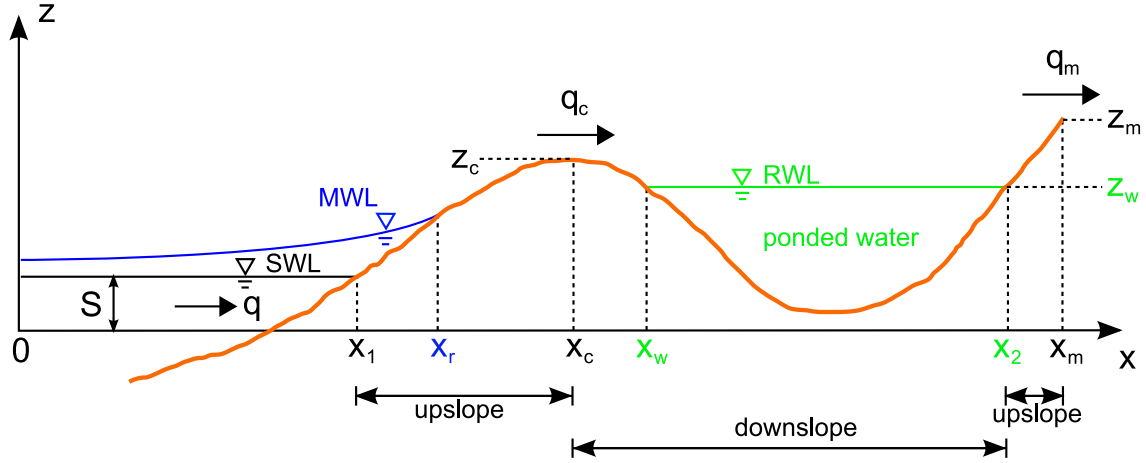


Figure 4.1: CSHORE definition sketch including the transition from wet model ($x < x_r$) to wet and dry model ($x > x_1$) and water ponding ($x_w < x < x_2$) with runnel water level (RWL) at $z = z_w$ where the ridge crest and the landward end point are located at (x_c, z_c) and (x_m, z_m) , respectively.

The time-averaged continuity equation for the impermeable bottom requires that the time-averaged cross-shore volume flux q is constant and equal to the rate q_c over the emerged ridge crest. The current velocity felt by waves is given by q/\bar{h} where \bar{h} = mean water depth given by $\bar{h} = (S + \bar{\eta} - z_b)$ in the wet zone where the overbar denotes time averaging. The representative wave period for irregular waves is assumed to be the spectral peak period T_p . The dispersion relation for linear waves in the presence of the current q/\bar{h} is expressed as

$$\omega = kg \tanh(k\bar{h}) ; \quad \omega + k q / \bar{h} = \omega_p \quad (4.1)$$

where ω = intrinsic angular frequency; k = wave number; g = gravitational acceleration; and ω_p = absolute angular frequency given by $\omega_p = 2\pi/T_p$. The wave period T for waves moving with the current q/\bar{h} is given by $T = 2\pi/\omega$. Equation (4.1) can be solved iteratively to obtain k and ω for known ω_p , \bar{h} , and q . The phase velocity

C and the group velocity C_g are given by

$$C = \omega/k ; \quad C_g = \frac{C}{2} \left[1 + \frac{2k\bar{h}}{\sinh(2k\bar{h})} \right] \quad (4.2)$$

The effect of the current in Equation (4.1) becomes important in very shallow water where the current q/\bar{h} may become as large as the phase velocity.

The cross-shore fluid velocity is represented by the depth-averaged velocity U whose probability distribution is assumed to be Gaussian. The mean and standard deviation of U are denoted by \bar{U} and σ_U . Linear progressive wave theory in finite depth is used to obtain

$$\sigma_U = C \frac{\sigma_\eta}{\bar{h}} ; \quad \frac{g\sigma_\eta^2}{C} + \bar{h}\bar{U} = q \quad (4.3)$$

where $g\sigma_\eta^2/C$ is the onshore volume flux induced by waves. The relations in Equation (4.3) are used to obtain σ_U and \bar{U} for known C , \bar{h} , σ_η , and $q = q_c$. The time-averaged return flow velocity \bar{U} is negative (offshore) and the wave overtopping rate q_c (onshore) reduces the return flow velocity. The rate q_c is estimated in the wet and dry zone.

The time-averaged momentum equation is written as

$$\frac{d}{dx} \left(S_{xx} + \frac{\rho q^2}{\bar{h}} \right) + \rho g \bar{h} \frac{d\bar{\eta}}{dx} + \tau_b = 0 \quad (4.4)$$

with

$$S_{xx} = \rho g \sigma_\eta^2 \left(2 \frac{C_g}{C} - \frac{1}{2} \right) ; \quad \tau_b = \frac{1}{2} \rho f_b \sigma_U^2 G_2 \quad (4.5)$$

where S_{xx} = cross-shore radiation stress; ρ = fluid density; τ_b = time-averaged bottom shear stress; f_b = bottom friction factor which is allowed to vary spatially; and G_2 = analytical function of \bar{U}/σ_U given by Kobayashi et al. (2007). The computed results are not sensitive for f_b of the order of 0.01 and use is made of $f_b = 0.015$

as in Kobayashi et al. (2009) who compared the previous version of CSHORE with two dune erosion tests conducted in the same sand tank as in the presented experiment. Chapter 6 presents some further justification for the adopted friction factor. Equation (4.4) mainly determines the cross-shore variation of $\bar{\eta}$.

In order to predict the cross-shore variation of σ_η , in the presence of the volume flux q , the wave action equation is expressed as

$$\frac{d}{dx} \left(\frac{F_x}{\omega} \right) = - \frac{D_B + D_f}{\omega} \quad (4.6)$$

with

$$F_x = \rho g \sigma_\eta^2 \left(C_g + \frac{q}{h} \right) ; \quad D_B = \frac{\rho g a_B Q H_B^2}{4T} ; \quad D_f = \frac{1}{2} \rho f_b \sigma_U^3 G_3 \quad (4.7)$$

where F_x = cross-shore wave energy flux including the effect of q ; D_B and D_f = energy dissipation rate per unit horizontal area due to wave breaking and bottom friction, respectively; a_B = empirical parameter introduced by Kobayashi et al. (2007) to account for the effect of the bottom slope on D_B ; Q = fraction of breaking waves given by Battjes and Stive (1985); H_B = breaker height for the estimation of D_B ; and G_3 = analytical function of \bar{U}/σ_U given by Kobayashi et al. (2007). The current effect on wave breaking is simply accounted for in Equation (4.7) using the wave period T obtained from Equation (4.1). Likewise, the equations for a_B and H_B given by Kobayashi et al. (2007) are modified to use the wave number k obtained from Equation (4.1).

The landward marching computation using Equations (4.1) - (4.7) is continued as long as the computed \bar{h} and σ_η are positive but terminated at the landward end of the emerged crest located at $x = x_c$. This end location of the computation is denoted as x_r . For the emerged crest shown in Figure 4.1, this location is on the seaward slope of the ridge where \bar{h} is less than 1 cm. It is noted that ponding

does not occur if the ridge crest is submerged and water can flow freely between the runnel and the surf zone on the seaward ridge slope. Equations (4.1) - (4.7) based on linear Gaussian wave theory are not valid in the zone which is not always wet. A probabilistic model is developed for this intermittently wet and dry zone.

4.2 Probabilistic Model for Wet and Dry Zone with Ponded Water

The time-averaged cross-shore continuity and momentum equations are derived from the nonlinear shallow-water wave equations. The time-averaged equations by Kobayashi et al. (1989) are modified to allow the possibility of a ponded water zone. The bottom profile in the wet and dry zone may be made up of upslope and downslope sections as indicated in Figure 4.1. If the ponding option is active, the ponded water zone ($x_w < x < x_2$) is determined by the intersection of the runnel water level (RWL) with the bottom profile. The seaward (x_w) and landward (x_2) limits of the ponded water zone are required to satisfy $x_c \leq x_w < x_2 \leq x_m$ where x_c and x_m are the cross-shore locations of the ridge crest and the landward limit of the computation domain. Ponded water is allowed to flow out if the RWL exceeds the bottom elevation z_c at $x = x_c$ or z_m at $x = x_m$. If ponded water is ignored in the wet and dry zone, x_w does not exist and x_2 is taken at the cross-shore location of a dry trough of a subaerial beach to separate the downslope and upslope zones.

For the zone of non-ponded water, the time-averaged volume flux q is constant and the continuity equation reads

$$\frac{dq}{dx} = 0 ; \quad q = \overline{hU} \quad (4.8)$$

where h and U = instantaneous water depth and depth-averaged cross-shore velocity, respectively. In the trough of a ridge-runnel system where ponded water is present,

the continuity equation is expressed as

$$\frac{dq}{dx} = -\frac{dz_w}{dt} \quad \text{for } x_w < x < x_2 \quad (4.9)$$

where t is the time associated with ponding and z_w is the ponded water level assumed to be horizontal (independent of x) and depends on t only. Then, q varies linearly with x because of Equation (4.9). On the other hand, the momentum equation is expressed as

$$\frac{d}{dx} \left(h \bar{U}^2 + \frac{g}{2} \bar{h}^2 \right) = -g \frac{dz_b}{dx} \bar{h} - \frac{1}{2} f_b |\bar{U}| \bar{U} \quad (4.10)$$

The instantaneous water depth h at given x is described probabilistically rather than in the time domain. Kobayashi et al. (1998) analyzed the probability distributions of the free surface elevations measured in the shoaling, surf and swash zones. The measured probability distributions were shown to be in agreement with the exponential gamma distribution which reduces to the Gaussian distribution offshore and the exponential distribution in the lower swash zone. The assumption for the Gaussian distribution has simplified the model based on Equations (4.1) - (4.7) in the wet zone significantly.

The assumption of the exponential distribution is made here to simplify the model in the wet and dry zone. The probability density function $f(h)$ is expressed as

$$f(h) = \frac{P_w^2}{\bar{h}} \exp \left(-P_w \frac{h}{\bar{h}} \right) \quad \text{for } h > 0 \quad (4.11)$$

with

$$P_w = \int_0^\infty f(h) dh ; \quad \bar{h} = \int_0^\infty h f(h) dh \quad (4.12)$$

where P_w = wet probability for the water depth $h > 0$; and \bar{h} = mean water depth for the wet duration. The dry probability of $h = 0$ is equal to $(1 - P_w)$. The mean water depth for the entire duration is equal to $P_w \bar{h}$. The overbar in Equations (4.8)

and (4.10) indicates averaging for the wet duration only. The free surface elevation $(\eta - \bar{\eta})$ above MWL is equal to $(h - \bar{h})$. The standard deviations of η and h are the same and given by

$$\frac{\sigma_\eta}{\bar{h}} = \left(\frac{2}{P_w} - 2 + P_w \right)^{0.5} \quad (4.13)$$

which yields $\sigma_\eta = \bar{h}$ for $P_w = 1$. This equality was supported by the depth measurements in the lower swash zone by Kobayashi et al. (1998) who assumed $P_w = 1$ in Equation (4.11).

The cross-shore velocity U may be related to the depth h in the wet and dry zone and expressed as

$$U = \alpha \sqrt{gh} + U_s \quad (4.14)$$

where α = positive constant; and U_s = steady velocity which is allowed to vary with x . The steady velocity U_s is included to account for offshore return flow on the seaward slope and the downward velocity increase on the landward slope. Holland et al. (1991) measured the bore speed and flow depth on a barrier island using video techniques and obtained $\alpha \simeq 2$ where the celerity and fluid velocity of the bore are assumed to be approximately the same. Tega and Kobayashi (1996) computed wave overtopping of dunes using the nonlinear shallow-water wave equations and showed $\alpha \simeq 2$ for the computed U and h . As a result, $\alpha = 2$ was used as a first approximation for the prediction of wave overtopping of fixed coastal structures (Kobayashi et al., 2010). However, a value of $\alpha = 1.6$ is adapted for sandy beaches to improve the agreement with measured overtopping and overwash rates for three laboratory dune overwash tests (Figlus et al., 2010). Using Equations (4.11) and (4.14), the mean \bar{U} and standard deviation σ_U of the cross-shore velocity U can be expressed as

$$\bar{U} = \frac{\sqrt{\pi}}{2} \alpha (P_w g \bar{h})^{0.5} + P_w U_s \quad (4.15)$$

$$\sigma_U^2 = \alpha^2 g \bar{h} - 2 (\bar{U} - U_s) (\bar{U} - P_w U_s) + P_w (\bar{U} - U_s)^2 \quad (4.16)$$

Equation (4.14) is substituted into Equations (4.8) and (4.10) which are averaged for the wet duration using Equation (4.11). The volume flux q is given by

$$q = \frac{3\sqrt{\pi}\alpha}{4} \bar{h} \left(\frac{g \bar{h}}{P_w} \right)^{0.5} + U_s \bar{h} \quad (4.17)$$

If no ponded water is present, q does not vary with x and is assumed to be equal to the volume flux q_o at the highest elevation point in the wet and dry zone where $U_s = 0$ is assumed. The rate q_o is the wave overtopping rate of impermeable coastal structures and dunes. In case of ponding, q depends on the cross-shore location because of Equation (4.9) and is expressed as

$$\begin{aligned} q &= q_c && \text{for } 0 \leq x \leq x_w \\ q &= q_c - \left(\frac{x-x_w}{x_2-x_w} \right) (q_c - q_m) && \text{for } x_w \leq x \leq x_2 \\ q &= q_m && \text{for } x_2 \leq x \leq x_m \end{aligned} \quad (4.18)$$

where q_c and q_m are the volume flux q given by Equation (4.17) with $U_s = 0$ at $x = x_c$ and x_m , respectively. The ponded water level z_w is predicted using Equations (4.9) and (4.18) which yields

$$\frac{dz_w}{dt} = \frac{q_c - q_m}{x_2 - x_w} \quad (4.19)$$

Equation (4.19) is solved using a finite difference method in time t . It is necessary to allow overflow at $x = x_c$ if $z_c < z_m$ and at $x = x_m$ if $z_c > z_m$ (see Figure 4.1). The water level z_w computed using Equation (4.19) is adjusted if the ponded water overflows. If $z_c < z_m$ and the computed $z_w > z_c$, the computed z_w and q_c are adjusted to be equal to z_c and q_m , respectively, because the overflow occurs at the ridge crest and U_s is not zero at $x = x_c$. If $z_c > z_m$ and the computed $z_w > z_m$, the computed z_w and q_m are adjusted to be equal to z_m and q_c , respectively, because the overflow occurs at the landward end and U_s is not zero at $x = x_m$. It is noted that for the case of no water ponding, Equations (4.18) and (4.19) are not used because

both q_c and q_m are equal to the wave overtopping rate q_o .

After lengthy algebra, the momentum equation (4.10) is expressed as

$$\frac{d}{dx} \left(B \frac{g \bar{h}^2}{P_w} + \frac{q^2}{\bar{h}} \right) = -g \frac{dz_b}{dx} \bar{h} - \frac{f_b}{2} \alpha^2 g \bar{h} G_b(r) \quad (4.20)$$

with the following assumption in the ponded water zone

$$\frac{dz_b}{dx} = \frac{dz_w}{dx} = 0 \quad \text{for } x_w \leq x \leq x_2 \quad (4.21)$$

where

$$B = \left(2 - \frac{9\pi}{16} \right) \alpha^2 + 1 ; \quad r = \frac{3\sqrt{\pi}}{4} \frac{U_s \bar{h}}{q - U_s \bar{h}} \quad (4.22)$$

The parameter B is related to the momentum flux term on the left hand side of Equation (4.10). Equation (4.21) for the ponded water zone is based on the assumption that the ponded horizontal ($\frac{dz_w}{dx} = 0$) water surface acts like a fixed bottom for water flowing over the ridge crest. This assumption is reasonable for a relatively narrow water surface because of limited mixing in the narrow pond. The function $G_b(r)$ in Equation (4.20) is given by

$$\begin{aligned} G_b(r) &= 1 + \sqrt{\pi} r + r^2 && \text{for } r \geq 0 \\ G_b(r) &= 2 \exp(-r^2) - r^2 - 1 + \sqrt{\pi} r [2 \operatorname{erf}(r) + 1] && \text{for } r < 0 \end{aligned} \quad (4.23)$$

where erf is the error function. The function G_b increases monotonically with the increase of r and $G_b = 0$ and 1 for $r = -0.94$ and 0.0. For $r < -1.5$, $G_b \simeq -(1 + \sqrt{\pi} r + r^2)$.

Equations (4.17) and (4.20) are used to predict the cross-shore variation of \bar{h} and U_s where σ_η , \bar{U} , and σ_U are computed using Equations (4.13), (4.15) and (4.16), respectively. It is necessary to estimate the wet probability P_w empirically. To simplify the integration of Equation (4.20), the following formula is adopted for

the upslope zones of the profile ($x_1 \leq x \leq x_c$ and $x_2 \leq x \leq x_m$):

$$P_w = \left[(1 + A_1) \left(\frac{\bar{h}_1}{\bar{h}} \right)^n - A \left(\frac{\bar{h}_1}{\bar{h}} \right)^3 \right]^{-1} ; \quad A = \frac{q^2}{Bg(\bar{h}_1)^3} ; \quad A_1 = \frac{q_1^2}{Bg(\bar{h}_1)^3} \quad (4.24)$$

where \bar{h}_1 and q_1 = mean water depth and volume flux, respectively, at the location of $x = x_1$ where $P_w = 1$; n = empirical parameter for P_w ; A and A_1 = parameters related to the rates q and q_1 , respectively, normalized by the depth \bar{h}_1 where water is present always. The transition from the wet ($P_w = 1$ always) zone to the wet and dry ($P_w < 1$) zone may be taken at $x_1 = x_{SWL}$ where x_{SWL} is the cross-shore location of the still water shoreline of an emerged crest as shown in Figure 4.1. Equation (4.24) is assumed to be valid on the upward slopes in the region of $x_1 \leq x \leq x_c$ and $x_2 \leq x \leq x_m$.

Integration of Equation (4.20) for P_w given by Equation (4.24) yields the following two equations for the two upslope regions. For the upward slope starting from $\bar{h} = \bar{h}_1$ at $x = x_1$, $\bar{h}(x)$ is given by

$$B_n (1 + A_1) \bar{h}_1 \left[\left(\frac{\bar{h}_1}{\bar{h}} \right)^{n-1} - 1 \right] = z_b(x) - z_b(x_1) + \frac{\alpha^2}{2} \int_{x_1}^x f_b G_b dx \quad (4.25)$$

For the upward slope starting from $\bar{h} = \bar{h}_2$ at $x = x_2$, $\bar{h}(x)$ can be shown to be expressed as

$$B_n (1 + A_1) \bar{h}_1 \left(\frac{\bar{h}_1}{\bar{h}_2} \right)^{n-1} \left[\left(\frac{\bar{h}_2}{\bar{h}} \right)^{n-1} - 1 \right] = z_b(x) - z_b(x_2) + \frac{\alpha^2}{2} \int_{x_2}^x f_b G_b dx \quad (4.26)$$

where $B_n = B(2 - n)/(n - 1)$; and $z_b(x)$ = bottom elevation at the cross-shore location x . If no downward slope exists in the region of $x_1 \leq x \leq x_m$, Equations (4.25) and (4.26) become the same because $x_2 = x_1$ and $\bar{h}_2 = \bar{h}_1$. The mean water depth \bar{h} at given x is computed by solving Equations (4.25) or (4.26) iteratively

where the function G_b given by Equation (4.23) depends on r defined in Equation (4.22). The empirical parameter n is taken to be in the range of $1 < n < 2$ so that $B_n > 0$. Kobayashi et al. (2010) calibrated n using 107 tests on wave overtopping of a dike in the form of $n = 1.01 + 0.98 [\tanh(A_o)]^{0.3}$ where $1.01 \leq n \leq 1.99$ and $A_o = \frac{q_o^2}{Bg(\bar{h}_1)^3}$ with q_o = volume flux at $x = x_1$ which equals q_c unless the landward end, where $q = q_m$, controls the volume flux at $x = x_1$ and causes $q_o = q_c = q_m$ as explained below Equation (4.19).

On the downward slope in the region of $x_c < x < x_2$, the wet probability P_w is assumed to be given by

$$P_w^{-1} = P_c^{-1} + \frac{q_c^2 - q^2}{Bg\bar{h}^3} \quad (4.27)$$

where P_c and q_c are the computed wet probability P_w and volume flux q at $x = x_c$. Substituting Equation (4.27) into Equation (4.20) and integrating the resulting equation from x_c to x , the mean depth $\bar{h}(x)$ is expressed as

$$\frac{\bar{h}}{\bar{h}_c} - 1 + \frac{P_c q_c^2}{4gB\bar{h}_c^3} \left[\left(\frac{\bar{h}_c}{\bar{h}} \right)^2 - 1 \right] = \frac{P_c}{2B\bar{h}_c} \left[z_b(x_c) - \tilde{z} - \frac{\alpha^2}{2} \int_{x_c}^x f_b G_b dx \right] \quad (4.28)$$

with

$$\begin{aligned} \tilde{z} &= z_b(x) && \text{for } x_c \leq x \leq x_w \\ \tilde{z} &= z_w && \text{for } x_w \leq x \leq x_2 \end{aligned} \quad (4.29)$$

where \bar{h}_c is the computed mean depth at $x = x_c$. In the ponded water zone water is assumed to flow above the ponded water level z_w instead of the bottom elevation z_b as indicated in Equation (4.21). As a result, the mean water level above the datum $z = 0$ is given by $(\bar{h} + z_w)$ where \bar{h} is the computed depth in the zone of $x_w \leq x \leq x_2$. The mean water depth above the local bottom is equal to $(\bar{h} + z_w - z_b)$. The computed wet probability P_w may be regarded as the ratio between the duration of wave action and the total duration. For the comparison with the wave gauge data, use is made of $P_w = 1$ for $x_w \leq x \leq x_2$ because it is difficult to separate the duration of wave

action from the submerged wave gauge data.

The landward marching computation of \bar{h} , σ_η , \bar{U} , and σ_U is initiated using the wet model from the seaward boundary $x = 0$ to the landward limit located at $x = x_r$. The water volume flux q_o at $x = x_1$ discussed in relation to the empirical parameter n below Equation (4.26) is taken as zero for the first iteration. The landward marching computation is continued using the wet and dry model from the location of $x = x_1$ where $\bar{h} = \bar{h}_1$ to the landward end of the computation domain or until the mean depth \bar{h} becomes less than the median sand diameter d_{50} which was 0.18 mm in this experiment. The rate q_o is computed using the computed volume flux in the wet and dry zone. This landward computation is repeated until the difference between the computed and assumed values of q_o is less than 1%. This convergence for q_o is normally obtained after several iterations. The computed values of \bar{h} , σ_η , \bar{U} , and σ_U by the two different models in the overlapping zone of $x_{SWL} < x < x_r$ (see Figure 4.1) are averaged to smooth the transition from the wet zone to the wet and dry zone.

4.3 Sediment Transport Model

The above time-averaged probabilistic model provides the hydrodynamic input required for the following sediment transport model. For the prediction of sediment transport on beaches, the effect of a roller on the steep front of a breaking wave is included in the combined wave and current model based on Equations (4.1) - (4.7) because the roller effect increases the offshore return current and improves the agreement of the measured and computed profile evolutions (Kobayashi et al., 2008). For coastal structures with steeper slopes, the roller effect does not necessarily improve the accuracy of the predicted wave overtopping rate probably because the roller does not develop over a relatively short distance on the steep slope. The equation of roller energy is used to compute the cross-shore variations of the roller

volume flux and its energy dissipation rate D_r in the same way as in the computation of dune erosion made by Kobayashi et al. (2009) for the case of no overwash and no water ponding.

Kobayashi et al. (2010) compared CSHORE with 207 tests for wave overtopping and overflow on fixed levees as well as 8 data sets for dune profile evolution with no or minor overwash. The agreement was mostly within a factor 2. However, their version of CSHORE underpredicted the major overwash events that occurred during the overwash experiment (Figlus et al., 2009). The computed values of the bedload transport rate q_b and the suspended load transport rate q_s indicated that suspended load was dominant when major overwash occurred. Consequently, the formula for q_s was modified for wave overwash (Figlus et al., 2009). In the following, the sediment transport formulas proposed by Kobayashi et al. (2008) for the wet zone are summarized and modified for the wet and dry zone including water ponding.

The probability P_b of sediment movement under the Gaussian velocity U in the wet zone is estimated assuming that the sediment movement occurs when the absolute value of the instantaneous bottom shear stress exceeds the critical shear stress corresponding to the critical Shields parameter of 0.05. The probability P_s of sediment suspension is estimated assuming that sediment suspension occurs when the turbulent velocity associated with the instantaneous energy dissipation rate due to bottom friction exceeds the sediment fall velocity. If the estimated P_s exceeds P_b , use is made of $P_s = P_b$ to ensure that sediment suspension occurs only when sediment movement occurs.

The time-averaged bedload transport rate q_b is expressed as

$$q_b = b P_b G_s \sigma_U^3 / [g (s - 1)] \quad (4.30)$$

where b = empirical bedload parameter; G_s = empirical function of the bottom slope

S_b and the upper limit 0.63 of the sand slope; and s = sediment specific gravity. The bedload parameter b has been calibrated to be in the range of 0.001 - 0.004 using available water tunnel and flume tests on horizontal bottoms for which $G_s = 1$. The computed profile evolutions and transport rates presented in the following are based on $b = 0.002$ (Kobayashi et al., 2009) but are not very sensitive to b because suspended load is computed to be dominant.

The time-averaged cross-shore suspended sediment transport rate q_s is expressed as

$$q_s = (a\bar{U} + a_o U_a) V_s \quad (4.31)$$

with

$$U_a = \frac{q_a}{\bar{h}} \quad (4.32)$$

$$V_s = P_s V_{Bf} (1 + S_b^2)^{0.5} \quad (4.33)$$

$$V_{Bf} = \frac{e_B D_r + e_f D_f}{\rho g (s - 1) w_f} \quad (4.34)$$

where a = suspended load parameter of the order of 0.2 under the action of waves and wave-induced currents; a_o = empirical overwash parameter with $a_o = 0$ corresponding to the case of no or minor overwash; U_a = onshore current due to the volume flux q_a due to wave overtopping, which is significant only in the zone of very small water depth \bar{h} ; V_s = suspended sediment volume per unit horizontal area; V_{Bf} = potential suspended sediment volume on a horizontal bottom when $P_s = 1$; e_B and e_f = suspension efficiencies for the energy dissipation rates D_r and D_f , previously calibrated as $e_B = 0.005$ and $e_f = 0.01$; and w_f = sediment fall velocity. If water ponding is not included, the volume flux q_a is the wave overtopping rate q_o estimated as q with $U_s = 0$ at the highest point in the wet and dry zone as explained in relation to Equation (4.17).

Equations (4.30) and (4.31) are proposed for the wet zone seaward of the mean water shoreline located at $x = x_r$ in Figure 4.1. For the wet and dry zone

added to the present version of CSHORE, the probability density function $f(h)$ of the instantaneous water depth h is assumed to be exponential and given by Equation (4.11). The instantaneous velocity U in the wet and dry zone is assumed to be expressed by Equation (4.14). Consequently, the sediment transport in the wet and dry zone is modified because of the different hydrodynamics.

The probability P_b of sediment movement is obtained for the probability distribution of U based on Equations (4.11) and (4.14). The movement of sediment particles represented by the median diameter d_{50} is assumed to occur when the instantaneous bottom shear stress given by $0.5 \rho f_b U^2$ exceeds the critical shear stress $\rho g (s-1) d_{50} \psi_c$ with the critical Shields parameter $\psi_c = 0.05$. The probability P_b of sediment movement is then the same as the probability of $|U| > U_{cb}$ with $U_{cb} = [2g(s-1)d_{50}\psi_c f_b^{-1}]^{0.5}$ and is given by

$$P_b = P_w \quad \text{for } U_s > U_{cb} \quad (4.35)$$

$$P_b = P_w \exp \left[-\frac{P_w (U_{cb} - U_s)^2}{\alpha^2 g \bar{h}} \right] \quad \text{for } |U_s| \leq U_{cb} \quad (4.36)$$

$$P_b = P_w \left\{ 1 - \exp \left[-\frac{P_w (U_{cb} + U_s)^2}{\alpha^2 g \bar{h}} \right] + \exp \left[-\frac{P_w (U_{cb} - U_s)^2}{\alpha^2 g \bar{h}} \right] \right\} \quad \text{for } -U_s > U_{cb} \quad (4.37)$$

where the upper limit of P_b is the wet probability P_w because no sediment movement occurs during the dry duration. On the other hand, sediment suspension is assumed to occur when the instantaneous turbulent velocity estimated as $(f_b/2)^{1/3}|U|$ exceeds the sediment fall velocity w_f . The probability P_s of sediment suspension is then the same as the probability of $|U| > U_{cs}$ where $U_{cs} = w_f(2/f_b)^{1/3}$. The probability P_s is given by Equations (4.35) - (4.37) with U_{cb} replaced by U_{cs} .

The bedload transport rate q_b is estimated using Equation (4.30) where the parameter b in the wet and dry zone is chosen so that the values of q_b computed for the two different zones are the same at the still water shoreline located at $x = x_{SWL}$.

The suspended sediment transport rate q_s is estimated using Equation (4.31). The potential suspended sediment volume V_{Bf} in the wet and dry zone is assumed to be constant and chosen so that the suspended sediment volume V_s given by Equation (4.33) is continuous at $x = x_{SWL}$. The assumption of constant V_{Bf} may be reasonable because suspended sediment in the swash zone tends to remain suspended. The suspended sediment volume V_s per unit horizontal area normally decreases landward because the probability P_s of sediment suspension is limited by the wet probability P_w which decreases landward.

Ponded water acts as a small settling basin for sediment transported over the ridge crest. Sediment contained in the overtopping flow settles into the ponded water in the runnel. Offshore flow over the ridge occurs if the runnel is full but the offshore flow contains less sediment. This transport asymmetry promotes landward ridge migration as observed in the ridge-runnel experiment. If the ponding option is activated, this transport asymmetry is taken into account by introducing an exponential reduction factor in the net sediment transport rate to reduce sediment transport inside the runnel and cause deposition near the seaward end of the runnel. The reduction factor due to ponded water is simply expressed as

$$R_p(x) = \exp\left(-\frac{x - x_w}{L_d}\right) ; \quad L_d = \frac{x_2 - x_w}{a_o} \quad \text{for } x > x_w \quad (4.38)$$

where the deposition length scale L_d is related to the width $(x_2 - x_w)$ of the ponded water surface. The overwash parameter a_o used in Equation (4.31) is adopted as an empirical parameter for L_d to reduce the number of empirical parameters. The reduction factor is applied to the bedload and suspended load transport rates (q_b , q_s), the probabilities of sediment movement and sediment suspension (P_b , P_s) and the volume of suspended sediment (V_s) in the zone of $x > x_w$ where q_b is proportional to P_b and q_s is proportional to V_s which is proportional to P_s . For the case of no ponded water, the appropriate volume flux q_a in Equation (4.32) is taken as the

wave overtopping rate q_o over a sand dune. For the case of a ridge with a runnel in front of a foreshore or a vertical wall, the appropriate volume flux q_a is not straightforward. Use is made of $q_a = q_d$ with $U_s = 0$ at $x = x_c$ in Equation (4.17) for the ridge-dominant zone of $x < x_2$ and $q_a = q_m$ at $x = x_m$ for the zone of $x > x_2$ dominated by the volume flux at the landward end. For the case of no offshore overflow over the ridge crest, q_d equals the volume flux q_c over the ridge crest. The use of $q_a = q_d$ instead of $q_a = q_c$ is based on visual observation during the ridge-runnel experiment where offshore overflow over the ridge crest carried little suspended sediment offshore. It should be stated that the modifications of the sediment transport model for the ponded water are empirical but necessary to mimic the complicated sediment dynamics.

Finally, the cross-shore sediment transport rates q_s and q_b computed for the wet zone and the wet and dry zone are averaged in the overlapping zone of $x_{SWL} \leq x \leq x_r$ for the smooth transition between the two zones. The landward limit of the computation is taken as the location of the mean water depth $\bar{h} = d_{50}$ or the landward end of the computation domain. The continuity equation of bottom sediment is solved numerically to obtain the bottom elevation at the next time level (Kobayashi et al., 2009). This computation procedure is repeated starting from the initial bottom profile until the end of each profile evolution computation. The computation time is on the order of 10^{-3} of the profile evolution time.

Chapter 5

COMPARISON OF NUMERICAL MODEL WITH RIDGE-RUNNEL EXPERIMENT

This chapter shows the comparison of CSHORE with the collected experimental data (Chapter 3). Input parameters for CSHORE are discussed briefly before the comparison of the hydrodynamics, profile evolution, wave overtopping and overwash rates.

5.1 Input Parameters

The numerical model CSHORE (Chapter 4) is used to predict hydrodynamic variables, profile evolution, overtopping, and overwash rates measured in the experiment. Input parameters are listed in Table 5.1. They are the same as those used by Kobayashi et al. (2009) except for the breaker ratio parameter γ which is reduced from 0.8 to 0.6 to improve the agreement between the measured and computed free surface standard deviation σ_η . This reduction of γ may be related to the gentler beach slope in the present experiment. Comparison is made with detailed laboratory measurements of free-surface elevations at 70 cross-shore locations over a barred beach profile (Boers, 1996) in a similar sand-bed wave flume as shown in Figure 5.1 where the agreement is better for $\gamma = 0.6$. In addition, the empirical parameter a_o given in Equation (4.31) needs to be specified as input. Calibration of a_o for the present experiment using the measured profile evolution, the measured overtopping rate q_m and the overwash rate $q_{bs} = (q_b + q_s)$ at the vertical wall has yielded a value of $a_o = 3.3$ for both the HR and LR test.

Uniform nodal spacing ($\Delta x = 2\text{ cm}$) is used and the bottom elevation at the landward end of the computation domain (vertical wall crest) is fixed for the computations. Apart from the parameters listed in Table 5.1, numerical model input includes the initial bottom elevation $z_b(x)$ for each test and the measured values of T_p , $\bar{\eta}$, and σ_η in each run at $x = 0$ corresponding to the location of WG1 in the experiment.

Table 5.1: CSHORE input parameters for ridge-runnel experiment.

| Parameter | Value | Description |
|-----------------|---------|--|
| Δx | 0.02 m | cross-shore nodal spacing |
| γ | 0.6 | breaker parameter |
| d_{50} | 0.18 mm | median sand diameter |
| w_f | 0.02 m | fall velocity |
| s | 2.6 | specific gravity |
| e_B | 0.005 | breaking wave efficiency |
| e_f | 0.01 | bottom friction efficiency |
| a | 0.2 | suspended load parameter for slope $S_b = 0$ |
| a_o | 3.3 | overtopping parameter (calibrated for HR and LR) |
| $\tan(\varphi)$ | 0.63 | limiting sand slope |
| b | 0.002 | bedload parameter |

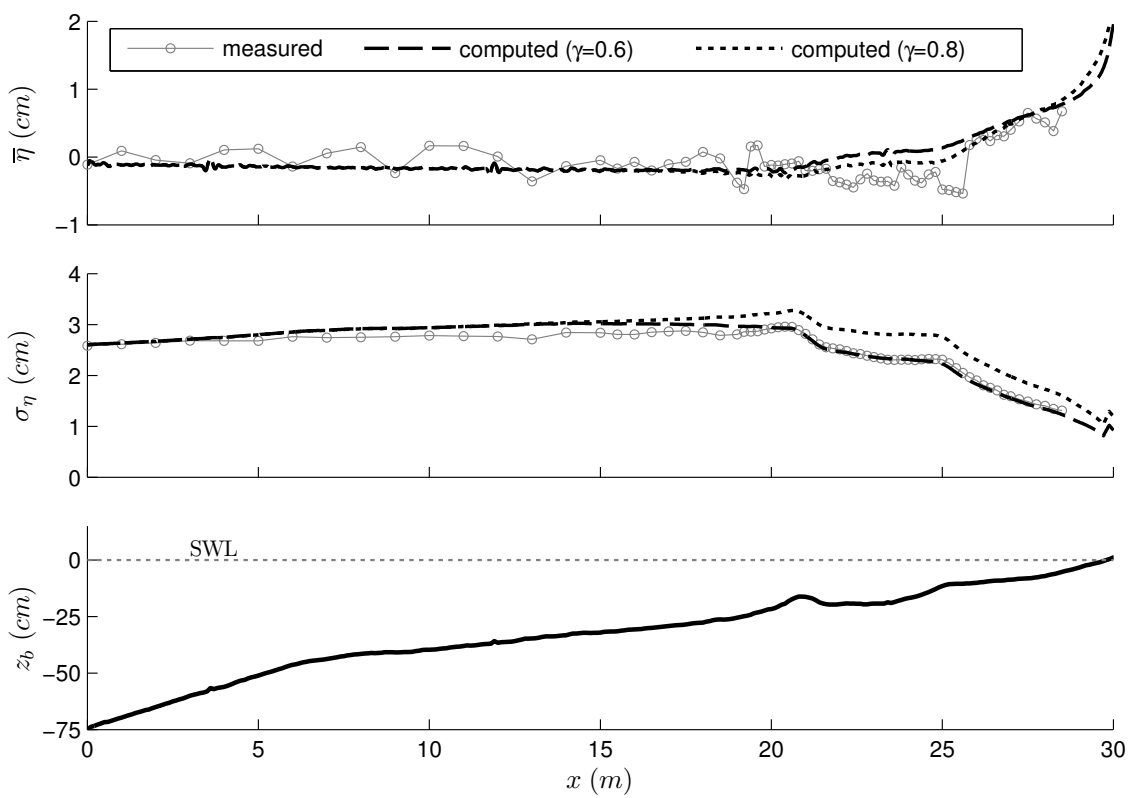


Figure 5.1: Comparison of CSHORE with detailed hydrodynamic measurements over a barred sand beach in a wave flume (Boers, 1996). The standard deviation σ_η is better predicted for $\gamma = 0.6$.

5.2 Hydrodynamics

Measured cross-shore variations of $\bar{\eta}$, σ_η , \bar{U} , σ_U , and P_w (Tables 3.8 - 3.18) are compared to CSHORE results for all 45 runs comprising tests HR and LR. The CSHORE input option *IPOND* can be set to 1 or 0 depending on whether ponded water should be included in the CSHORE computation (*IPOND* = 1) or not (*IPOND* = 0). The option of *IPOND* = 1 is added in the present version of CSHORE. The calibrated value of $a_o = 3.3$ is used for the hydrodynamic comparisons. It should be stated that the measured and computed cross-shore variations of the hydrodynamic variables in the ridge and runnel zone are strongly affected by the beach profile evolutions described in Section 5.3.

Two general types of figures are employed to give a complete picture of the numerical comparisons and to show the differences between the two *IPOND* computation options. Evolution figures illustrate changes over time for all the runs in an entire test (*IPOND* = 1) with individual runs identified by color ranging from green (first run) to red (final run). The initial computed variation at time $t = 0$ is also displayed (black dashed line) to indicate the computed results on the initial profile. Circles represent measured values during each 400-s run and solid lines denote computed values at the end of each run for the entire computation domain ($x = 0 - 19.9\text{ m}$).

Individual run figures display measured and computed values for 3 specific runs in the zone of $x > 14\text{ m}$ to allow for more detailed comparison in the nearshore region. Focus lies on the difference between the two computation options *IPOND* = 1 and 0 as indicated by red dashed and blue dotted lines, respectively. The 3 displayed runs are HR1, HR4, and HR10 for the HR test and LR2, LR13, and LR35 for the LR test to represent the beginning, middle, and end of the respective test. The integer next to HR or LR indicates the run number.

5.2.1 Free-Surface Elevation

Figure 5.2 shows the comparison of $\bar{\eta}$ and σ_η for all 10 runs of the HR test where the bottom two panels are simply a zoomed replica of the top two panels in the region of major profile evolution ($x > 14m$). Since the measured values of $\bar{\eta}$, σ_η , and T_p at $x = 0$ are specified as the boundary conditions for each run, the agreement between measured and computed values at wave gauges WG1-WG3 is excellent. Even the computed values at WG4 and WG5 in the breaker zone match the measured ones very well. The slight undulations in the computed results between the WG3 and WG4 locations are due to minor numerical oscillations and disappear if larger grid spacing such as 5 cm is used. The narrow grid spacing of 2 cm is necessary to resolve the hydrodynamics and profile evolution in the ridge-runnel zone.

WG6 is located on the seaward slope of the ridge initially. The mean of the free-surface elevation there is slightly overpredicted while its standard deviation (significant wave height $H_{mo} = 4\sigma_\eta$) is slightly underpredicted. Being situated inside the runnel at the beginning of the HR test, WG7 and WG8 records are affected by changes in the runnel water level (RWL) and the bottom elevation (z_b) as well as by the wet duration because of the averaging during the wet duration only. Measured values for $\bar{\eta}$ above SWL (datum $z = 0$) are initially above 5 cm but decrease as the continuously lowered ridge crest (and lowered RWL) migrates onshore. Measured values of σ_η decrease in landward direction during the presence of the ridge and afterwards due to dissipation on the beach slope. The computed $\bar{\eta}$ values at WG7 are well within the measured range but slightly below the measured values at WG8. The undulation in the computed $\bar{\eta}$ between WG6 and WG7 is caused by the undulation of the computed beach profile. Computed σ_η is close to the measurements and reproduces the decrease from WG6 to WG8 fairly well, especially after the ridge-runnel system has disappeared. The black dashed lines verify that the model is

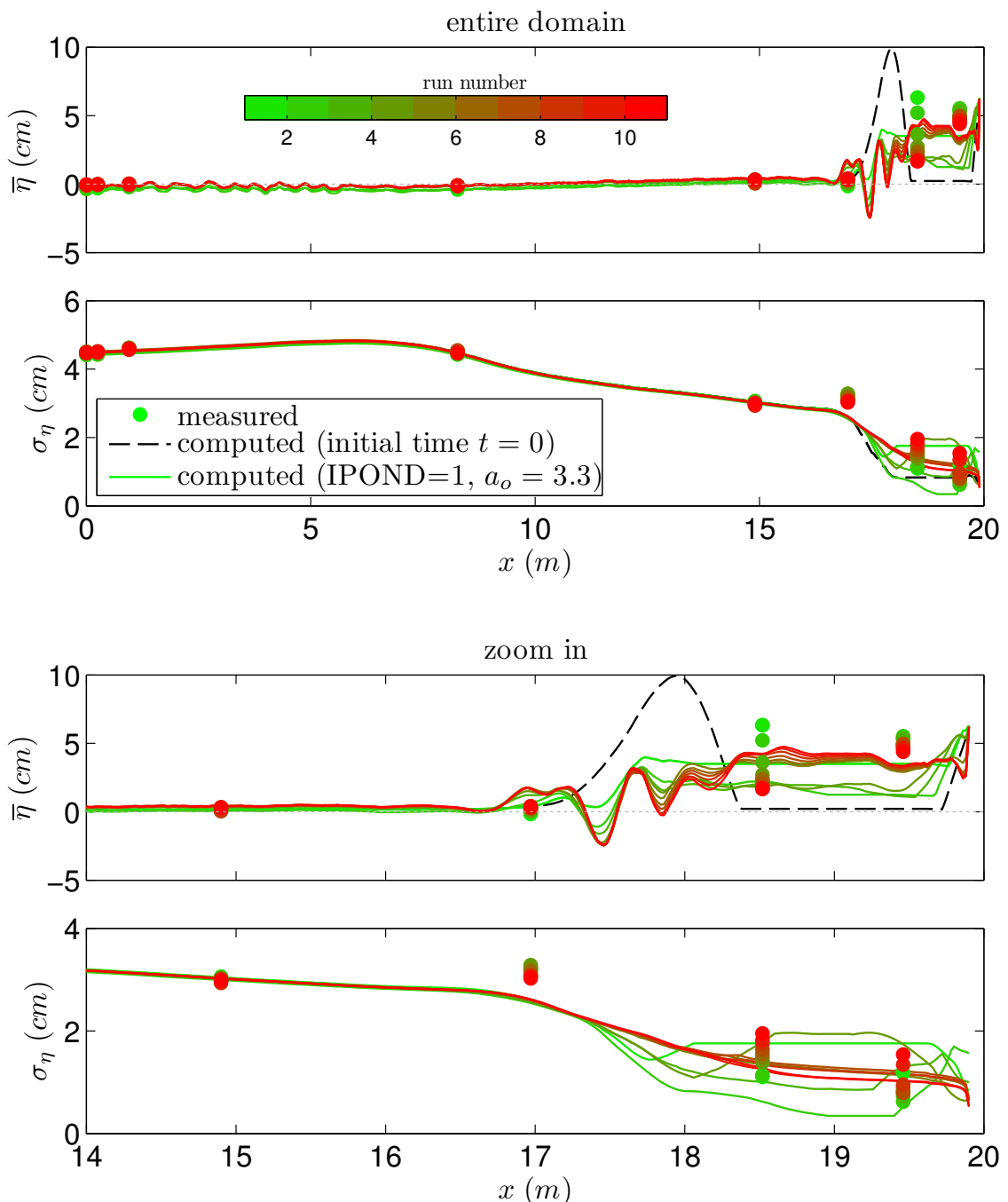


Figure 5.2: Measured and computed $\bar{\eta}$, and σ_η for all 10 runs of the HR test.

initiated with RWL=SWL in the first run. The errors in the comparison are mostly due to difficulties in modeling the exact ridge-runnel profile evolution over an entire test. Despite this fact, the overall agreement of measured and computed $\bar{\eta}$ and σ_η is reasonable at all WG locations.

Figures 5.3, and 5.4 give a closer look at $\bar{\eta}$ and σ_η during 3 individual HR runs and elucidate the effect of the numerical water ponding routine. Since the hydrodynamic computation tends to follow the bottom profile for $IPOND = 0$, the ridge-runnel signature is visible in the computed results of $\bar{\eta}$. For $IPOND = 1$ the model results after the initial run are somewhat closer to the measured values. Both computation options represent the cross-shore distribution of wave height (Figure 5.4) reasonably in view of the extremely rapid profile changes which make the accurate prediction of hydrodynamics rather challenging.

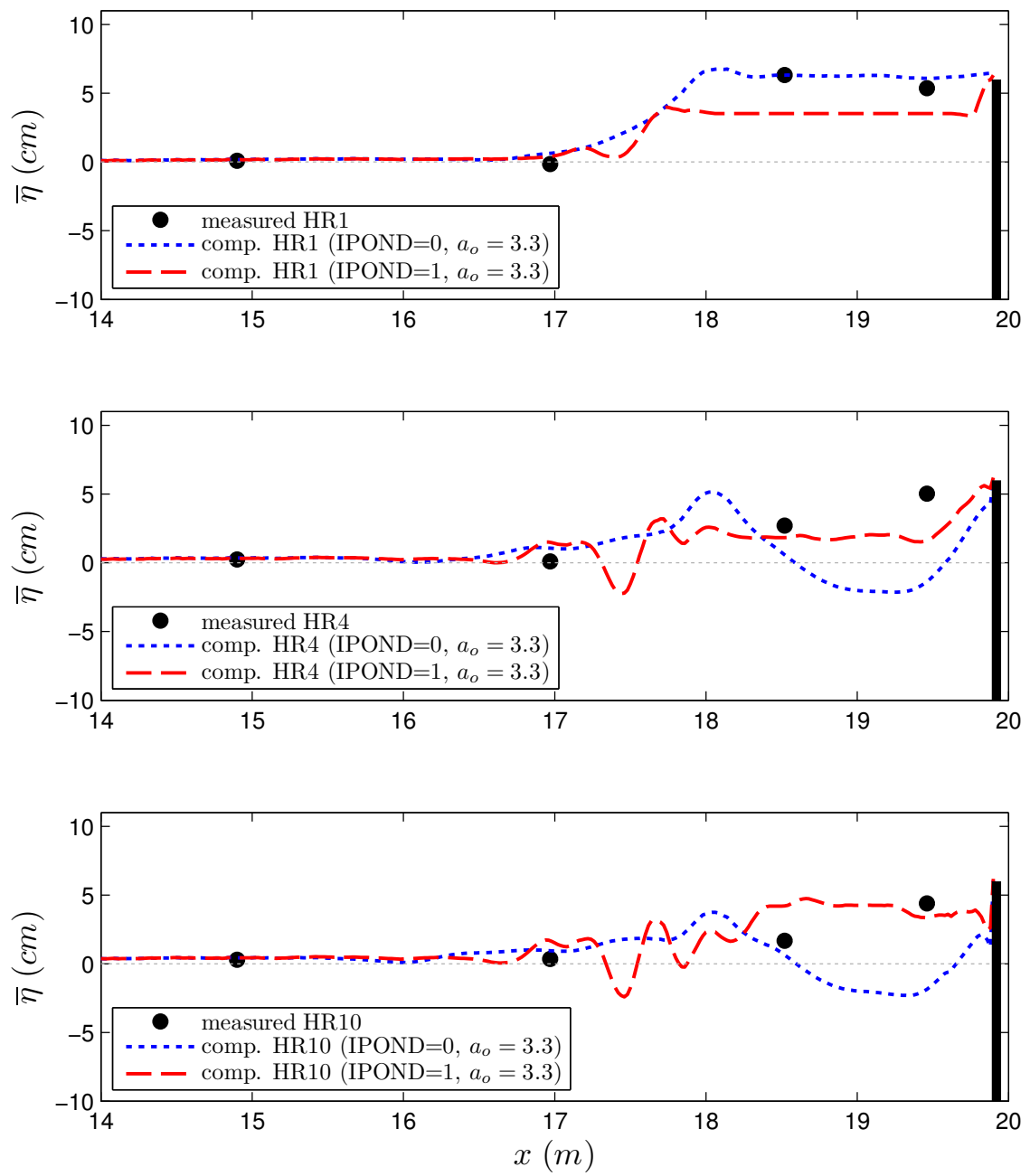


Figure 5.3: Measured and computed $\bar{\eta}$ for 3 runs of the HR test.

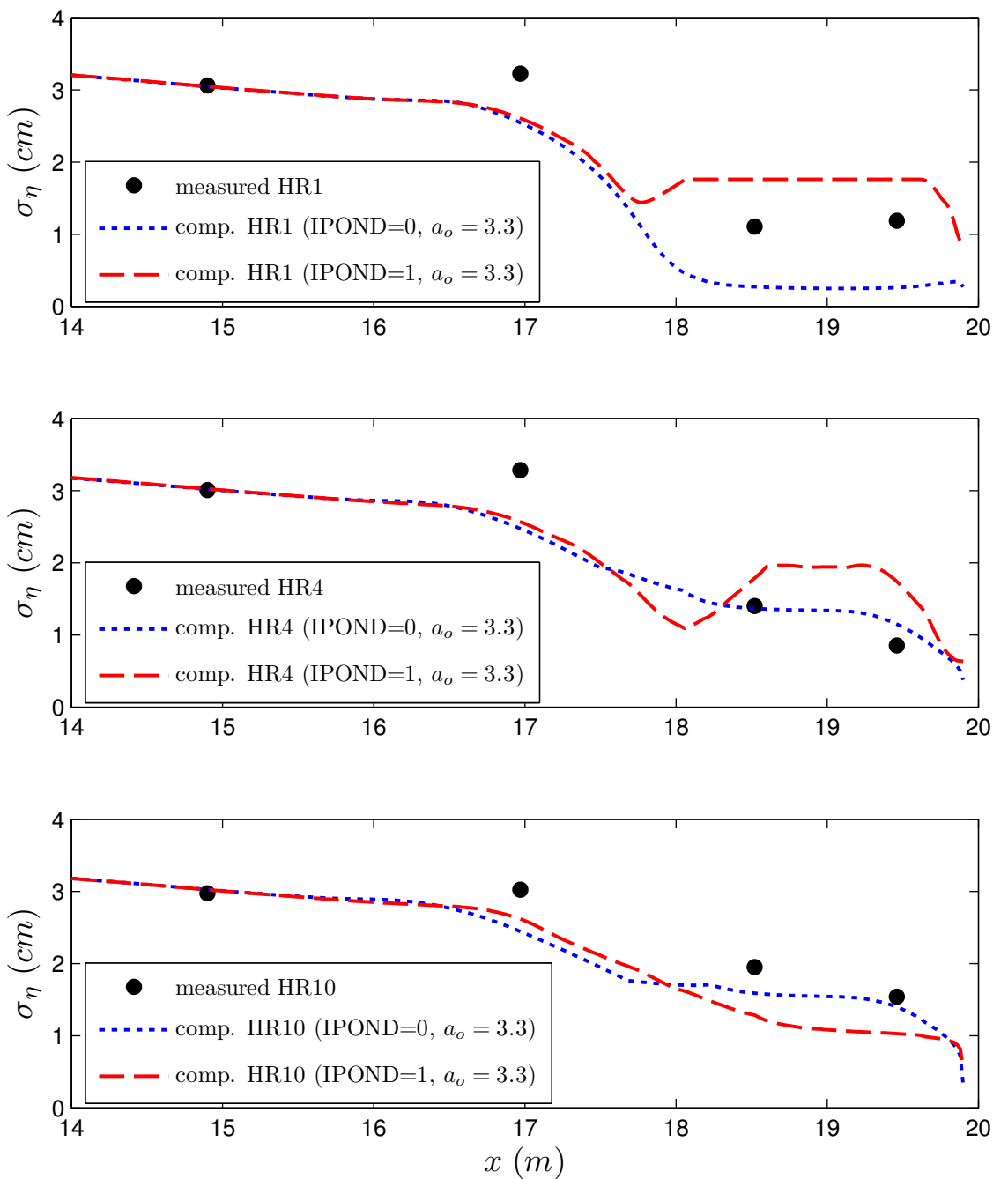


Figure 5.4: Measured and computed σ_η for 3 runs of the HR test.

The free-surface elevation $\bar{\eta}$ and its standard deviation σ_η during all 35 runs of the LR test are shown in Figure 5.5 for the entire computation domain (top panels) and the zoomed nearshore region (bottom panels). Since the offshore water level was 8 cm lower compared to HR, the zone of irregular wave breaking was shifted seaward of WG4 which was inside the surf zone. Setup ($\bar{\eta} > 0$) is predicted very well for WG4-WG6. The computed mean water level in the ridge-runnel region at WG7 and WG8 also matches the measured values well despite the profile changes. The computed wave height, represented by σ_η , is slightly underpredicted at WG4-WG6. The computed σ_η values are in the range of measured values but fluctuate between 1 and 3 cm among all the runs. The relatively large measured σ_η values at WG7 and WG8 during LR1 are due to the large RWL change during LR1 which made it difficult to separate the mean and fluctuating components.

Figure 5.6 reveals that the mean water level in the zone of ridge migration is much better represented for $IPOND = 1$ compared to $IPOND = 0$. The computed σ_η values do not differ significantly for the two computation options and represent the measured values reasonably well for the three runs shown in Figure 5.7.

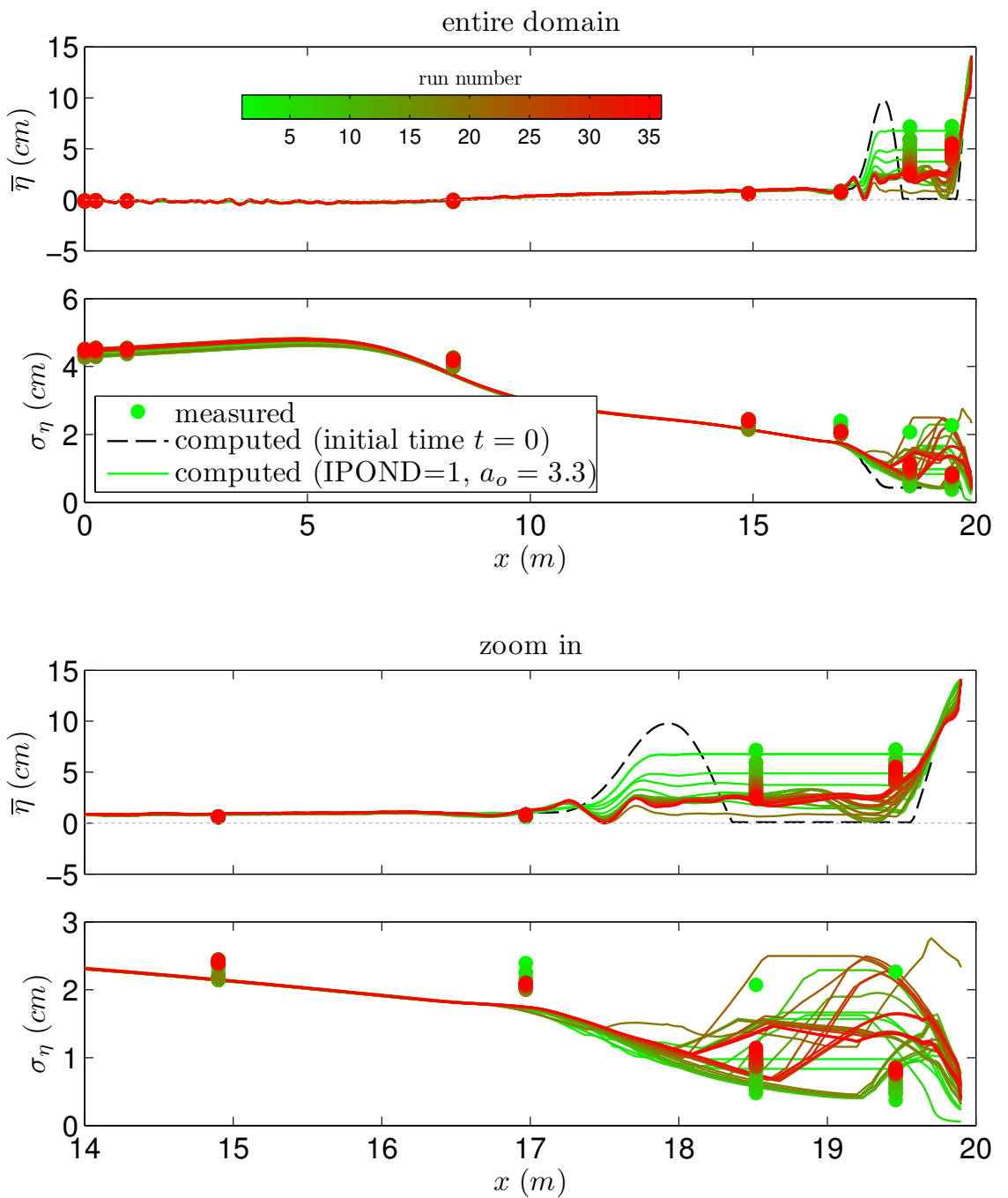


Figure 5.5: Measured and computed $\bar{\eta}$, and σ_η for all 35 runs of the LR test.

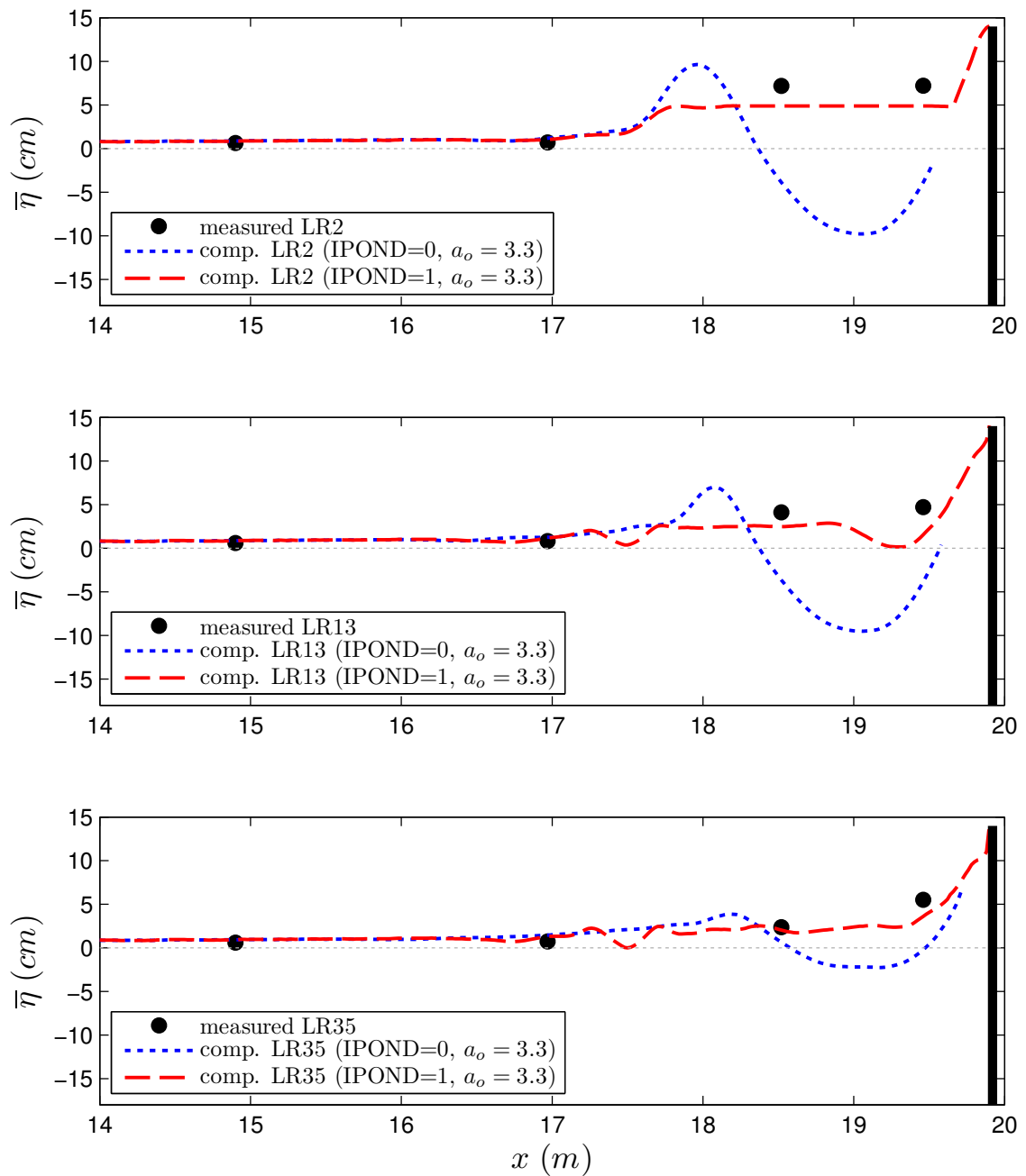


Figure 5.6: Measured and computed $\bar{\eta}$ for 3 runs of the LR test.

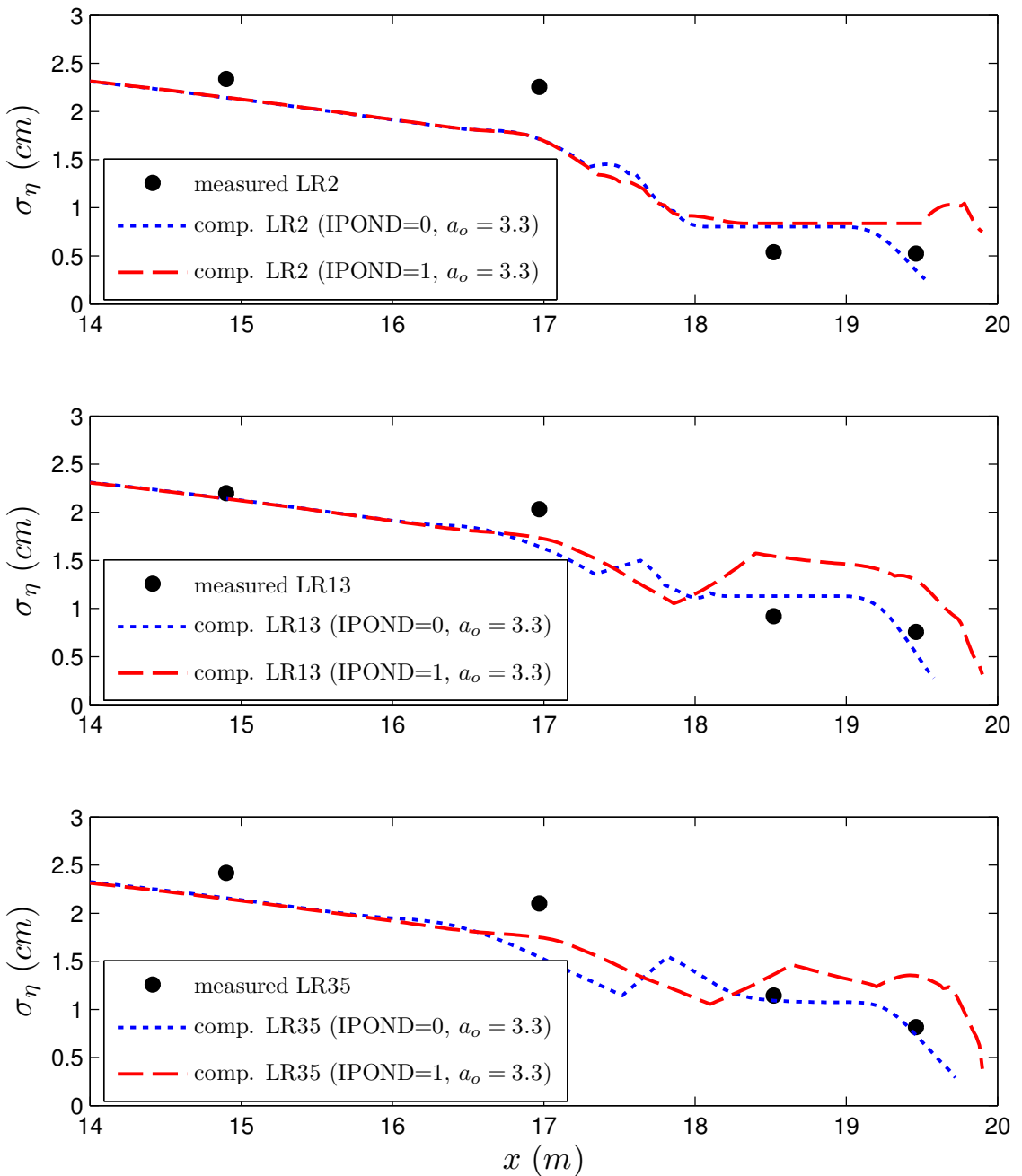


Figure 5.7: Measured and computed σ_η for 3 runs of the LR test.

5.2.2 Cross-Shore Velocity

Figure 5.8 shows the evolution of the mean and standard deviation of the measured cross-shore velocity component u at the two ADV instrument locations for every run of the HR test as circles. The exact locations of the measurement volumes are listed in Table 2.3. In addition, the computed cross-shore distribution of the mean \bar{U} and standard deviation σ_U of the depth-averaged cross-shore velocity U landward of $x = 14 m$ are plotted as solid lines.

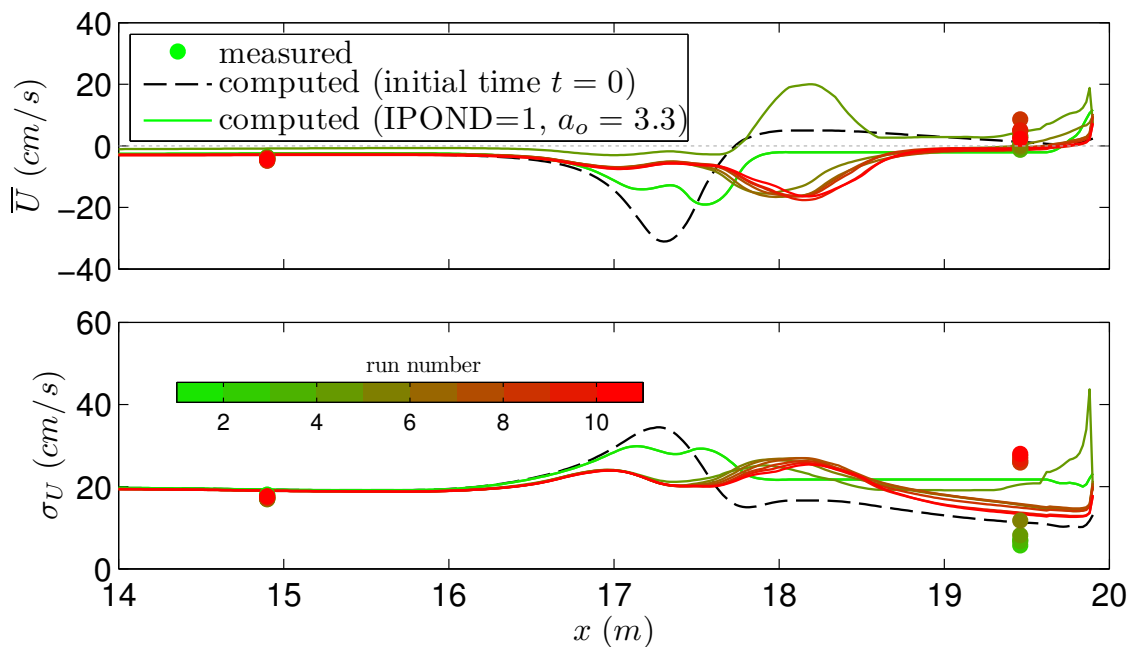


Figure 5.8: Measured (circles) and computed (lines) mean and standard deviation of the cross-shore velocity U for all 10 runs of the HR test. Colors range from green (initial run) to red (final run) to indicate changes over time.

The figure shows that the measured values of \bar{U} and σ_U at the location of ADV1 at the foot of the ridge ($x = 14.90 m$) are in good agreement with the computed results for all runs with only slight overprediction of the offshore return current in certain runs. These small differences may be attributed to the fact that the measurements represent only a single point in the vertical velocity profile at 2/3

of the local water depth below SWL. The computed cross-shore velocities at the location of ADV2 ($x = 19.46\text{ m}$) represent the measurements fairly closely. Velocity sign changes in the ridge-runnel region from negative (offshore) to positive (onshore) are related to rapid onshore ridge migration and runnel filling. After the runnel is smoothed out during HR5, computed \bar{U} values are slightly negative on the order of -1 cm/s whereas measured values are slightly positive as listed in Table 3.16. The submergence fraction D_w in those runs is approximately 50%. The very small measured and computed velocities may not be accurate.

Measured σ_U values at $x = 19.46\text{ m}$ vary between 5.7 cm/s (HR2) and 28.0 cm/s (HR10) with a distinct jump after HR5 due to the disappearance of the runnel. The computed values are within the measured range but do not show the pronounced jump found in the measured data values. This difference may be related to the difference between the measured and computed velocities because the computed U is based on the velocity above the runnel water level for $IPOND = 1$.

The differences between the computed and measured \bar{U} and σ_U for the two computation options $IPOND = 1$ and $IPOND = 0$ are presented for 3 runs of the HR test in Figures 5.9 and 5.10, respectively. The positive computed \bar{U} values at the wall ($x = 19.90\text{ m}$) for $IPOND = 1$ (red dashed lines) are related to the overtopping flow in the HR test. The middle panel of Figure 5.9 (HR4) also shows the sign change in computed \bar{U} ($IPOND = 1$) from negative to positive due to overtopping flow over the ridge with very small water depths. For $IPOND = 0$, \bar{U} remains negative throughout the test due to no ponded water and reduced wave overtopping.

In Figure 5.10 the main difference between $IPOND = 1$ and $IPOND = 0$ is visible in run HR1 where the large σ_U values in the runnel for $IPOND = 1$ are the standard deviation of the velocity U above RWL for the duration of wave action. This artificial definition of the computed U makes it difficult to interpret physically.

The evolution of the measured and computed velocity parameters \bar{U} and σ_U for all 35 runs of the LR test is displayed in Figure 5.11. Measured results from the Vectrino ($x = 18.52\text{ m}$) complement the results obtained from ADV1 ($x = 14.90\text{ m}$) and ADV2 ($x = 19.46\text{ m}$). The offshore return current measured by ADV1 with an average value of -4.5 cm/s (Table 3.15) over all 35 runs is reproduced well numerically. Computed mean cross-shore velocities in the ridge-runnel zone are predominantly offshore directed with a minimum value of -30 cm/s in run LR22 because the computed wave overtopping rate over the wall is very small or zero for the LR test.

The computed σ_U values shown in the bottom panel of Figure 5.11 fluctuate between 10 and 40 cm/s which is close to the range of the measured values at the Vectrino location but exceeds the range of values measured at the ADV2 location.

The comparison between the $IPOND = 1$ and $IPOND = 0$ computation results and the measured data for three runs of the LR test (Figure 5.12) shows that both model options perform reasonably well in simulating the mean current in the ridge-runnel area but only $IPOND = 1$ yields a sign change from offshore to on-shore current on the seaward ridge slope (LR2, top panel). Small negative (offshore) velocities were measured inside the runnel during the LR test with no overtopping over the wall. After the ridge-runnel system was smoothed out the offshore velocities at the Vectrino and ADV2 locations increased in magnitude. These increased negative values are modeled well with either of the two CSHORE computation options for water ponding as shown for LR35 in the bottom panel of Figure 5.12

The computed standard deviation of the cross-shore velocity component increases for both computation options as the waves approach the seaward edge of the ridge. Increased σ_U values indicate larger orbital wave velocities in the wet zone and up and downrush velocities in the wet and dry zone on the ridge slope.

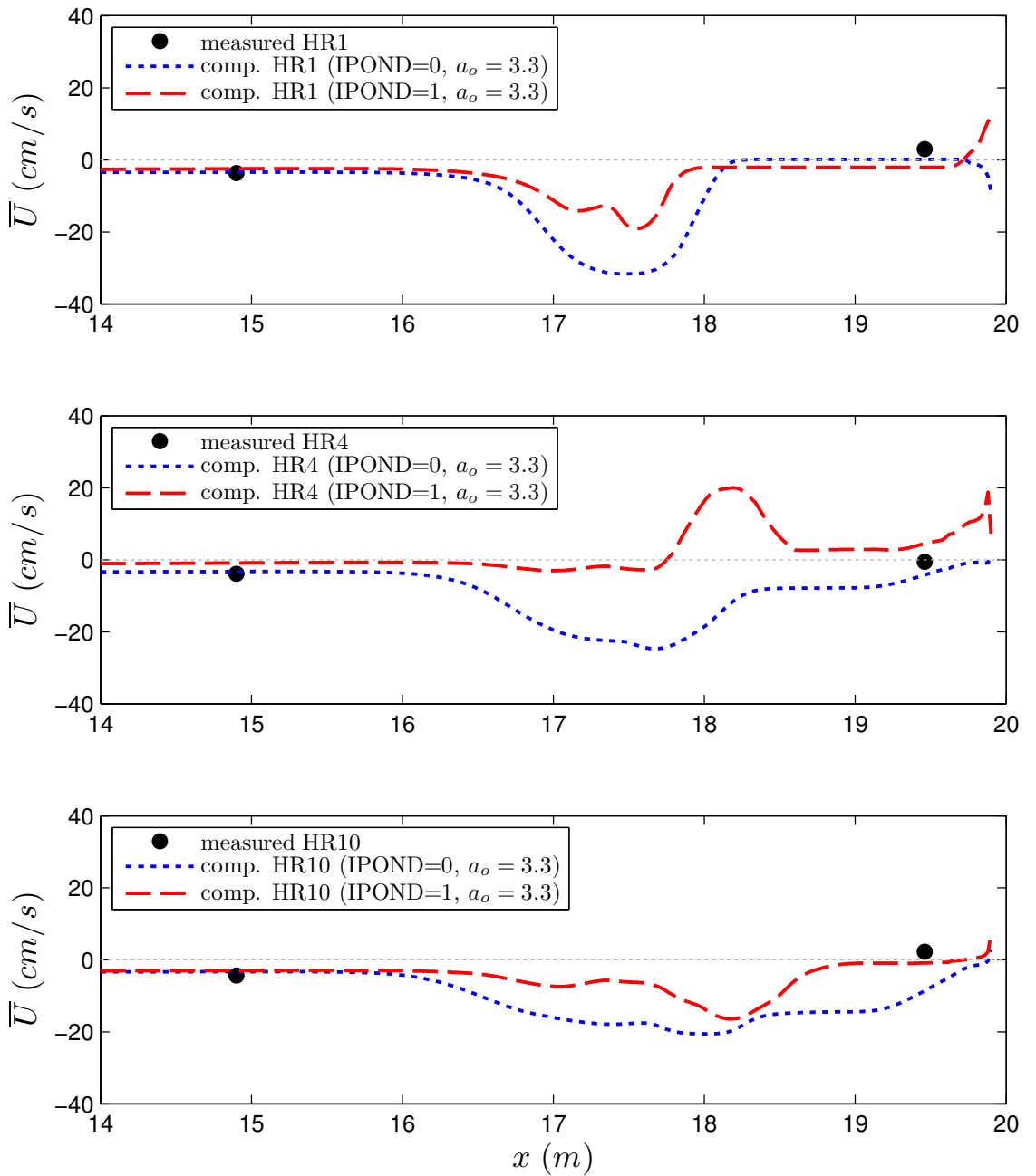


Figure 5.9: Measured (circles) and computed (lines) mean cross-shore velocity \bar{U} for 3 runs of the HR test. The measured velocities are point measurements and are assumed to correspond to the computed depth-averaged velocities. The results for the two computation options $IPOND = 1$ and $IPOND = 0$ are shown as red dashed and blue dotted lines, respectively.

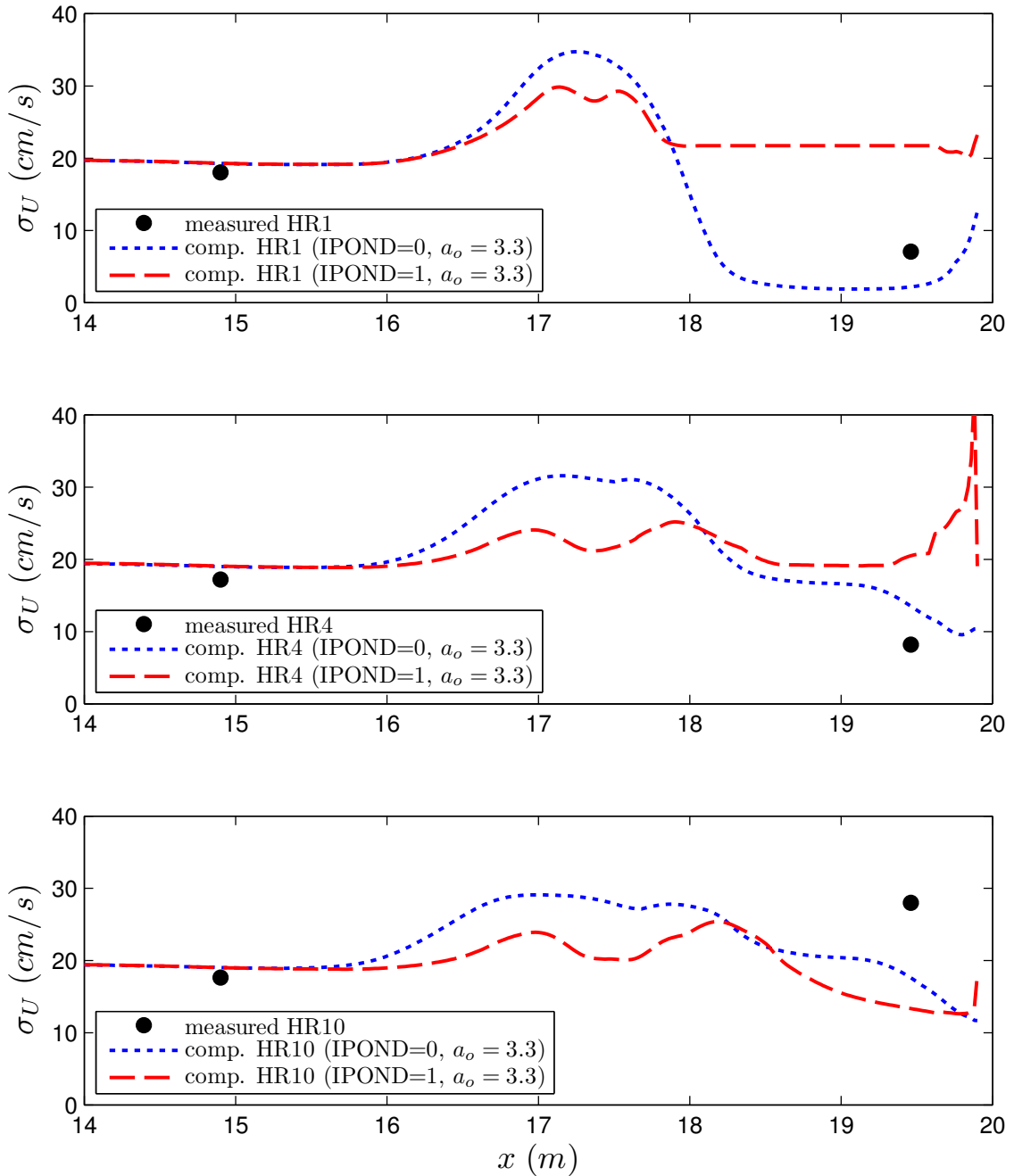


Figure 5.10: Measured (circles) and computed (lines) standard deviation σ_U for 3 runs of the HR test. The results for the two computation options $IPOND = 1$ and $IPOND = 0$ are shown as red dashed and blue dotted lines, respectively.

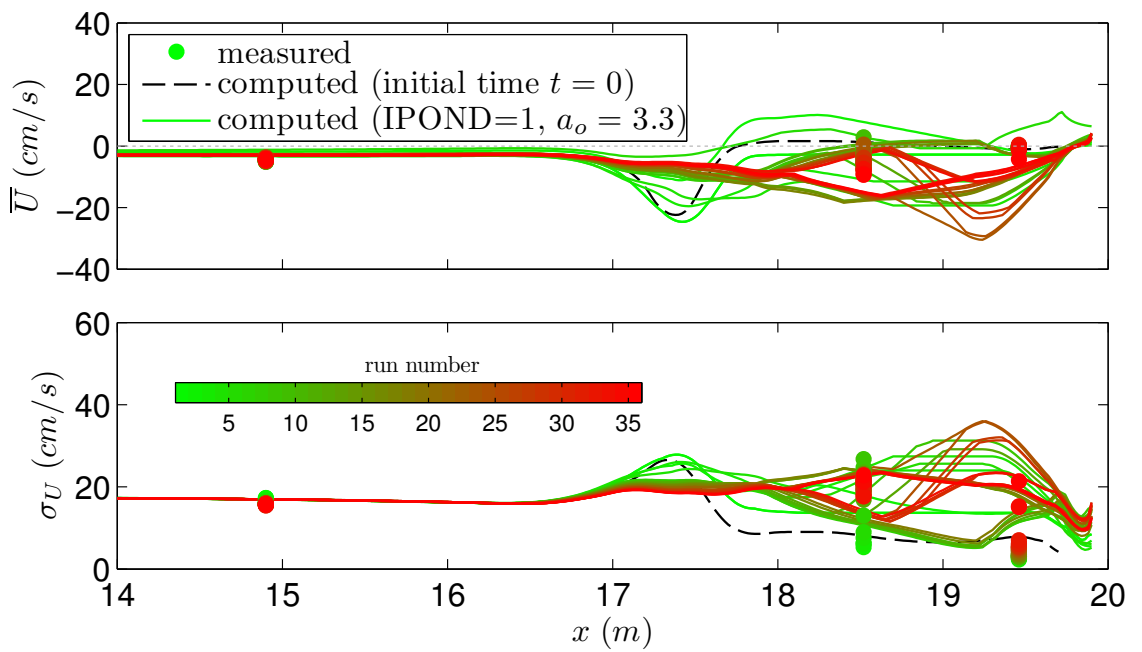


Figure 5.11: Measured (circles) and computed (lines) mean and standard deviation of the cross-shore velocity U for all 35 runs of the LR test. Colors range from green (initial run) to red (final run) to indicate changes over time.

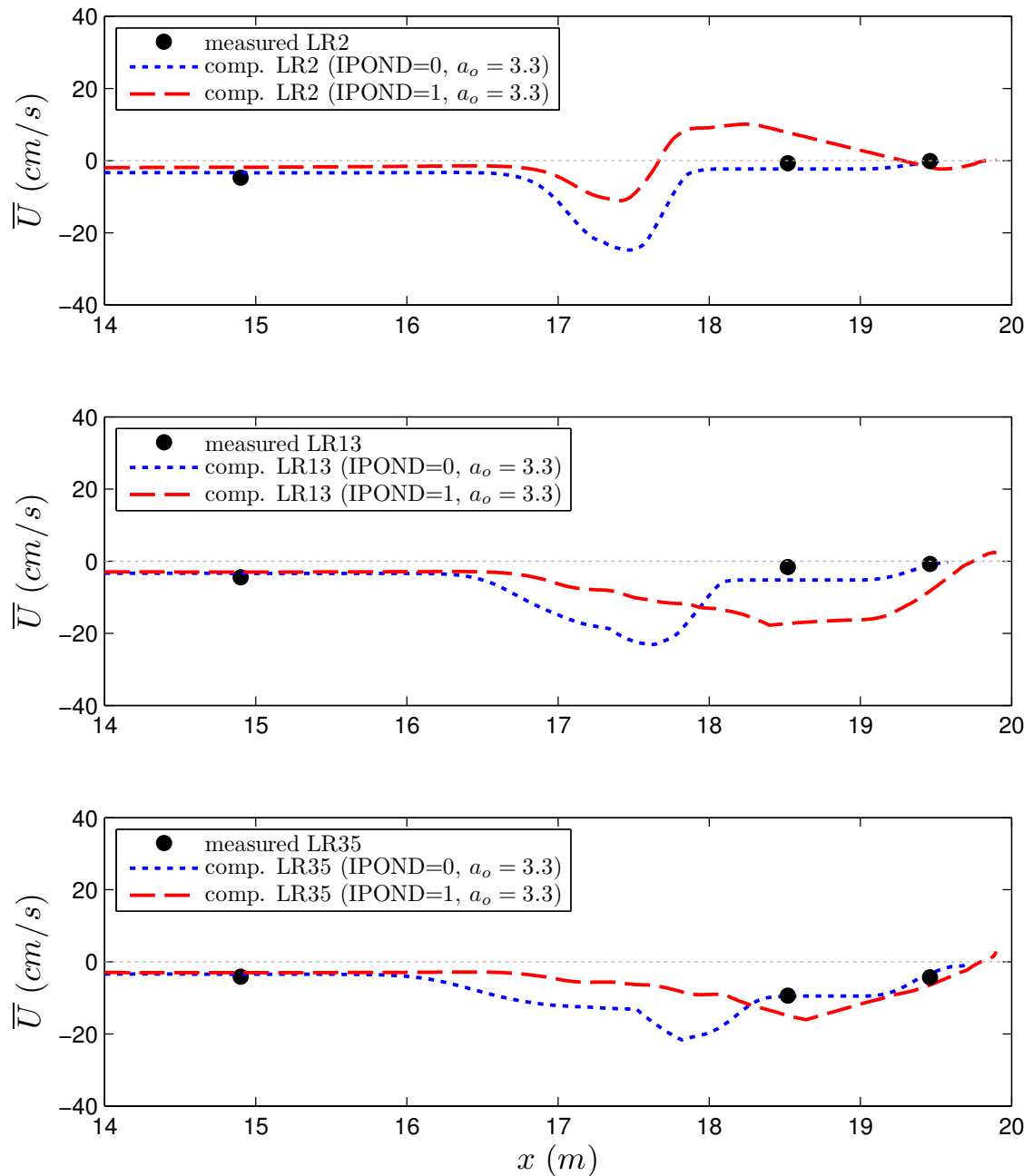


Figure 5.12: Measured (circles) and computed (lines) mean cross-shore velocity \bar{U} for 3 runs of the LR test. The results for the two computation options $IPOND = 1$ and $IPOND = 0$ are shown as red dashed and blue dotted lines, respectively.

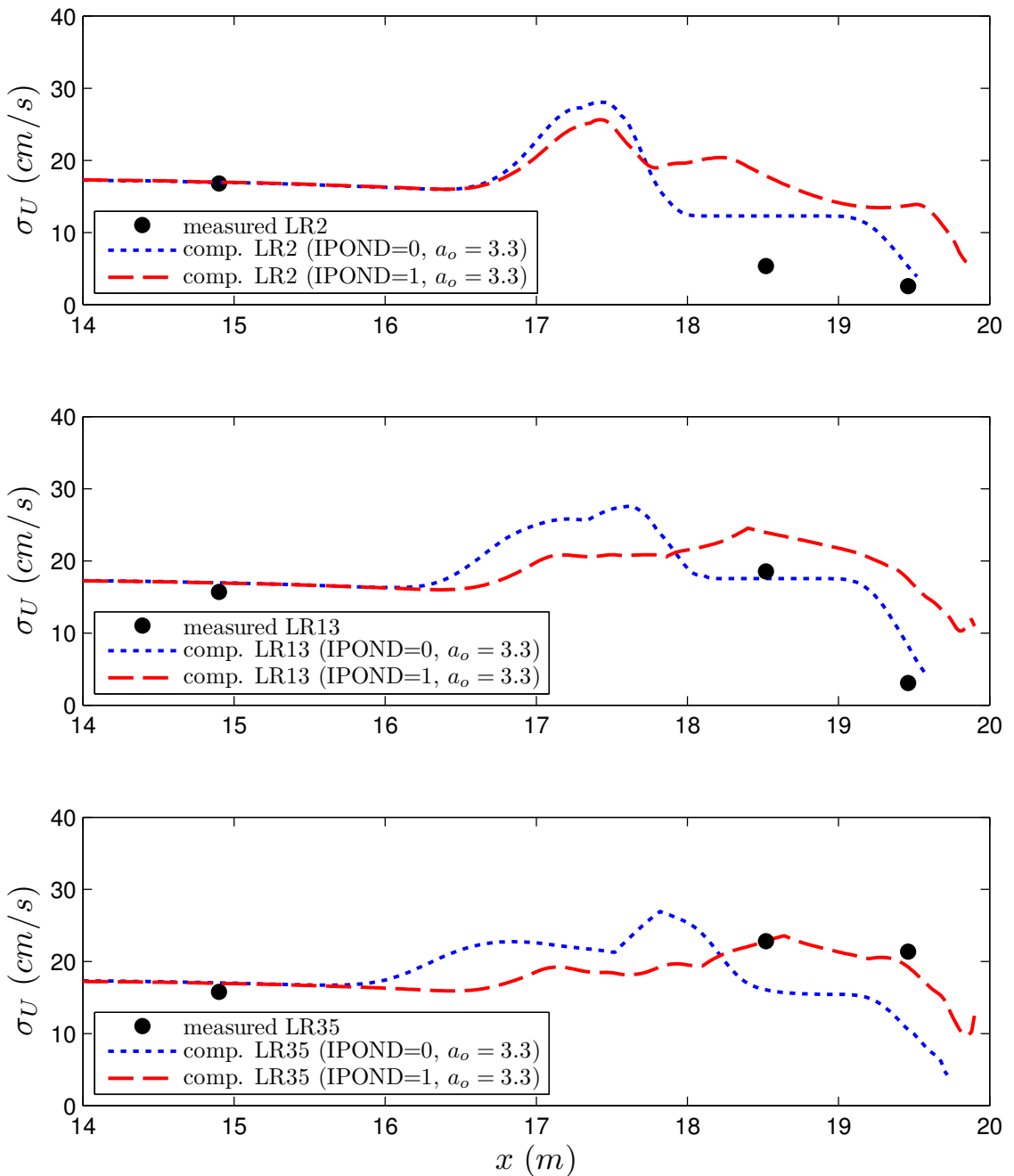


Figure 5.13: Measured (circles) and computed (lines) standard deviation of the cross-shore velocity σ_U for 3 runs of the LR test. The results for the two computation options $IPOND = 1$ and $IPOND = 0$ are shown as red dashed and blue dotted lines, respectively.

5.2.3 Wet Probability

The wet probability P_w is defined in Equation (3.3) and can take on values between 0 and 1. Measured values are listed in Tables 3.12 and 3.13 for the HR and LR tests, respectively. Computed values are displayed together with measured values in Figure 5.14 for all 10 runs of the HR test ($IPOND = 1$) and in Figure 5.15 for 3 of the 35 runs in the LR test ($IPOND = 1$ and $IPOND = 0$).

The computed P_w in the HR test drops below unity on the ridge crest and returns to unity in the ponded water region in runs HR1-HR4. Qualitatively, the same behavior is found in the measured data where the first three HR runs show P_w values below unity at the WG7 location and values of unity at the WG8 location. At WG8 the computed wet probability starts to drop below unity in run HR4 compared to HR5 for the measured data. The computed values of the wet probability at WG8, after the runnel was filled with sand, are significantly lower than the measured ones. This discrepancy may be related to the difference between the measured and computed profile evolutions as discussed in the next section since the computed profile errors strongly influence the hydrodynamic computation in the wet and dry zone. In the vicinity of the vertical wall all computed P_w values are smaller than 1 because wave overtopping occurred only intermittently.

For the LR test (Figure 5.15) the computed P_w is displayed for runs LR2, LR13, and LR35 for $IPOND = 1$ and $IPOND = 0$. The computed result using $IPOND = 0$ does not account for ponded water and the computed P_w is less than unity landward of the still water shoreline on the emerged ridge (top panel). Using the $IPOND = 1$ option, the model reproduces the measured wet probability for the three displayed runs fairly well, even after the runnel disappeared (middle and bottom panel). The computed P_w in the vicinity of the wall approaches zero since no overtopping occurred in the LR test. The difference between $IPOND = 0$ and 1 at the wall is related to the computed wave overtopping rates for $IPOND = 0$ and

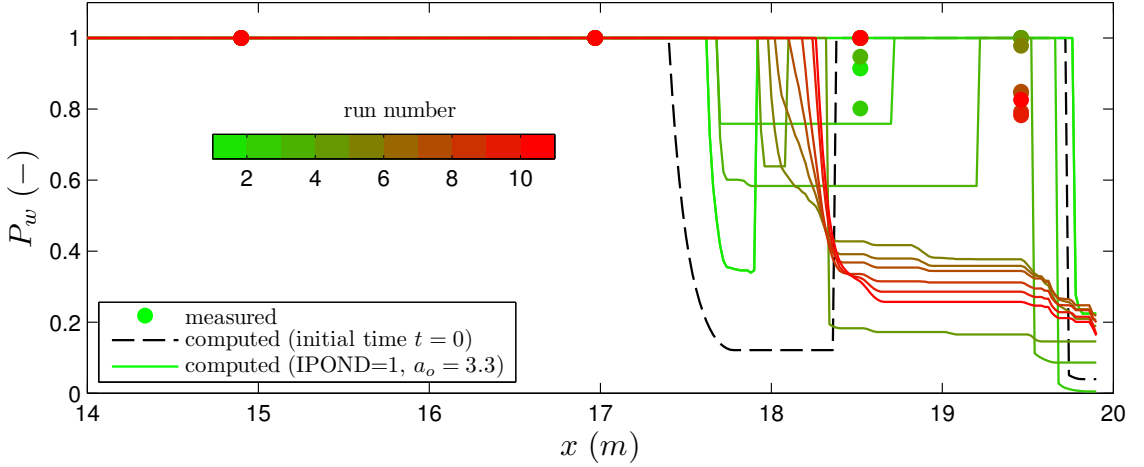


Figure 5.14: Measured (circles) and computed (lines) wet probability P_w for all 10 runs of the HR test. Colors range from green (initial run) to red (final run) to indicate changes over time.

1 as discussed in Section 5.4.

In general, CSHORE is accurate enough to predict the measured hydrodynamic variables as was the case with previous comparisons. Discrepancies mainly occur in the ridge-runnel zone of rapid profile change and water ponding. Taking water ponding into account in the computation ($IPOND = 1$) improves the hydrodynamic prediction in this zone compared to the computation without ponding ($IPOND = 0$). More detailed hydrodynamic measurements related to ridge-runnel systems are necessary but it is extremely difficult to measure the hydrodynamics in the intermittently wet and dry zone on a beach of rapid profile evolution. It may be noted that a time-dependent numerical model would predict the hydrodynamics in the ridge-runnel zone more accurately if the ridge and runnel had been fixed and immobile.

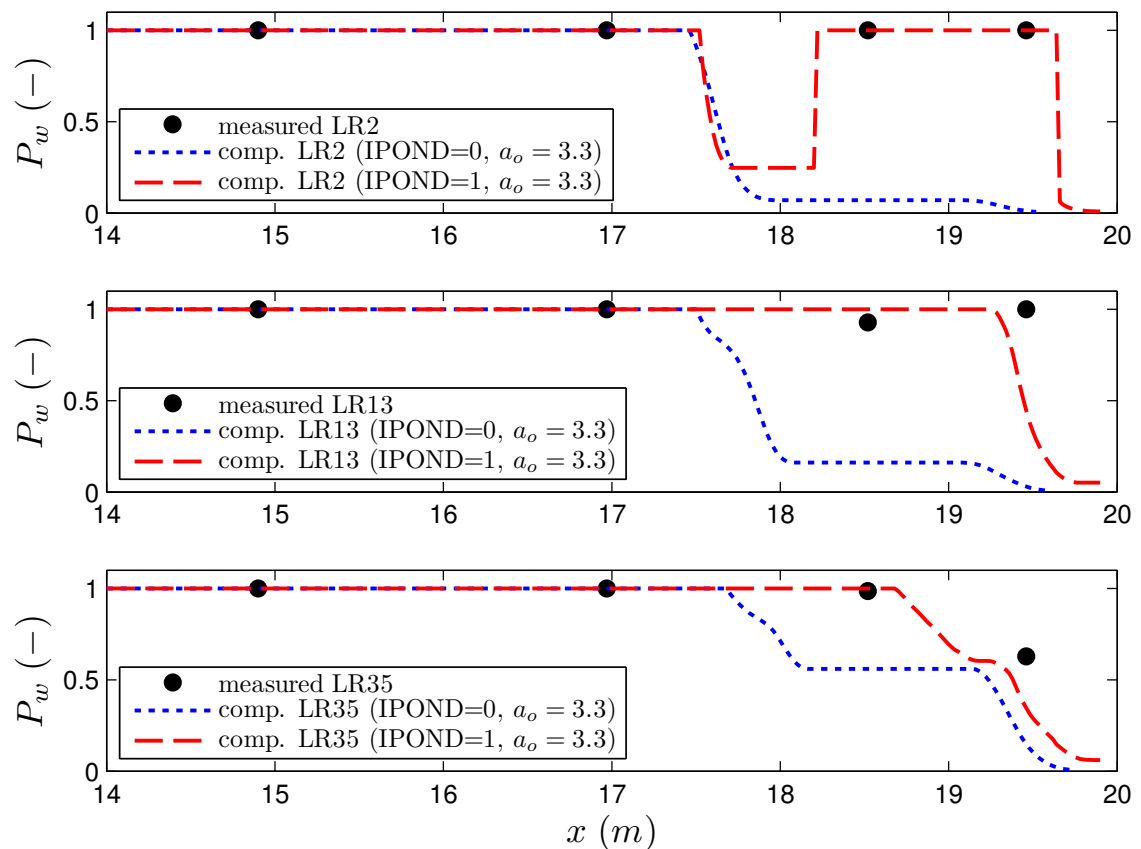


Figure 5.15: Measured (circles) and computed (lines) wet probability P_w for 3 runs of the LR test. The results for the two computation options $IPOND = 1$ and $IPOND = 0$ are shown as red dashed and blue dotted lines, respectively.

5.3 Profile Evolution

Accurate prediction of the measured profile evolution is a key element in this ridge-runnel migration study since the movement of these features plays an important role in the coastal sediment budget. The complicated interactions between hydrodynamics and sediment transport and the special importance of the ponded water in the runnel make these profile change computations challenging. Errors in the early computation stages may accumulate during the profile evolution computation since the computation is started from the initial profile in each test.

In the following, the measured and computed profiles for three runs of the HR and LR tests are presented. Computed profiles are shown for both CSHORE computation options ($IPOND = 1$ and $IPOND = 0$), to visualize the numerical effect of the water ponding routine. The overwash parameter a_o was calibrated to a value of 3.3 for both tests. The three panels in Figure 5.16 display the measured and computed profiles after run HR1 (top), HR4 (middle) and HR10 (bottom). Using $IPOND = 1$ improves the profile evolution prediction significantly compared to $IPOND = 0$ because the effect of the ponded water on sediment transport is included. Thus, the following discussion of the numerical results pertains to $IPOND = 1$ only.

The computed profile after run HR1 shows that most processes observed in the first run are reproduced by the model. Erosion on the seaward ridge slope, ridge crest lowering, and sediment deposition on the seaward side of the runnel are found in both the measured and the computed profiles. The profile lowering on the seaward ridge slope is underpredicted. The formation of a terrace close to $x = 17\text{ m}$ at $z = -0.1\text{ m}$ can be found in both the measured and computed profiles but the model fails to predict the adjacent concave profile shape accurately. The computed ridge crest is too wide and the crest lowering is slightly overpredicted. The model reproduces the measured runnel trough location and shape very well.

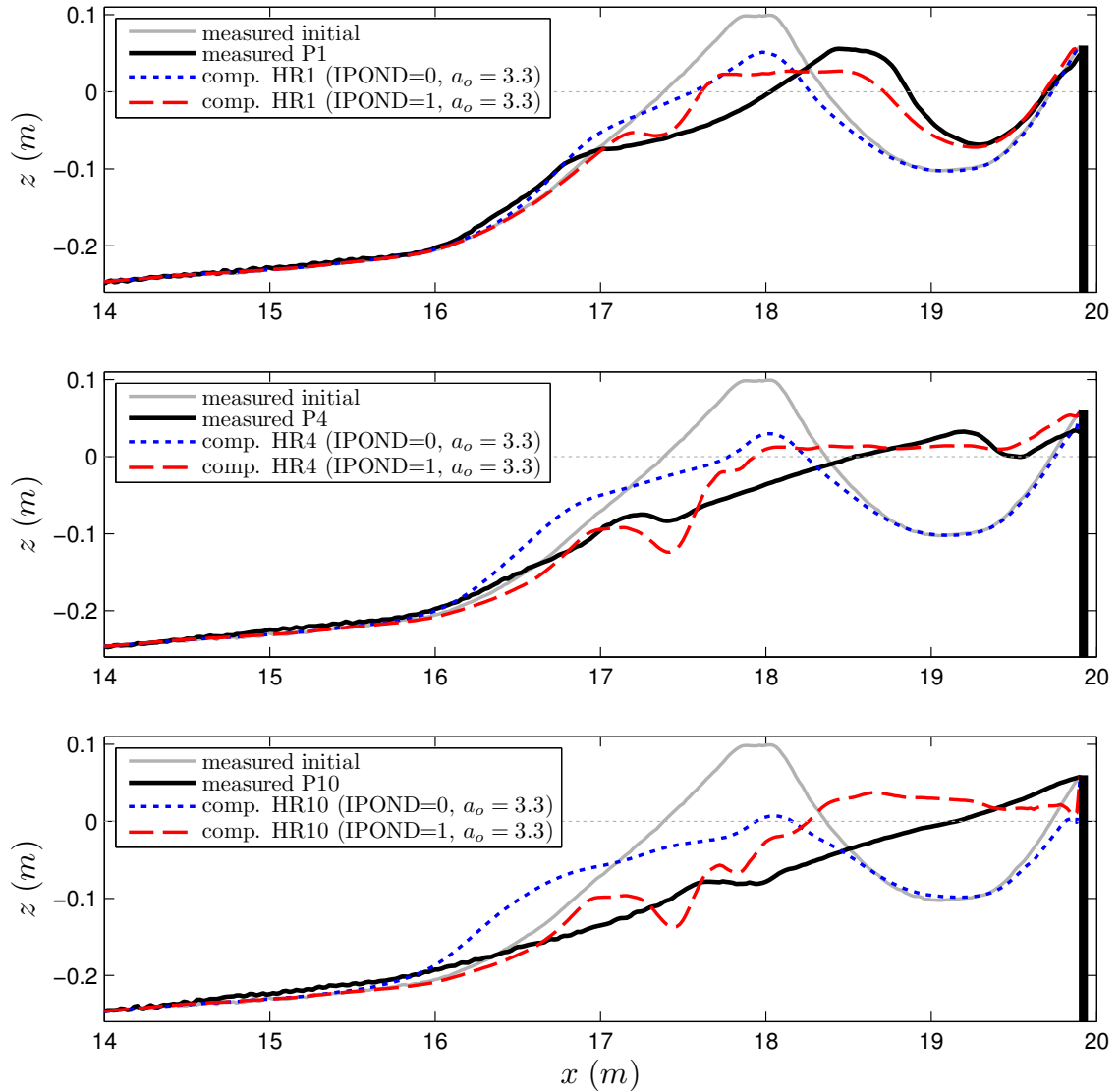


Figure 5.16: Measured and computed ridge-runnel profiles for 3 runs of the HR test. The results for the two computation options $IPOND = 1$ (red dashed lines) and $IPOND = 0$ (blue dotted lines) are shown along with the measured initial profile (gray) and the measured profile of the respective run (black) profiles.

The deposition on the landward ridge slope is slightly underpredicted. The adopted sediment transport formulation does not reproduce the landward ridge migration adequately.

After run HR4 (middle panel in Figure 5.16), the ridge-runnel system is completely smoothed out to a horizontal plateau in the computed result. In the measured profile a small ridge-runnel feature remains visible after HR4. The measured gentle seaward ridge slope after HR4 is not reproduced by $IPOND = 1$ which predicts a scour hole.

At the end of the HR test (HR10) the measured profile is essentially a sloped beach in front of the vertical wall with a 30 cm wide terrace feature around $x = 18 m$ which evolved from the terrace formed in previous runs. The computed profile shows further erosion of the ridge but the computed horizontal deposition in front of the wall does not resemble the measured sloping beach in front of the wall. The sediment transport formulation in front of the wall and the wall boundary condition may need further improvement. Nevertheless, in view of the very rapid ridge-runnel migration in the HR test, the model reproduces the essential processes observed in this test where wave overtopping and overwash over the wall continued to remove sand from the beach.

The measured and computed profile evolution for the LR test is presented in Figure 5.17 in a similar manner. The computed profiles for $IPOND = 1$ and $IPOND = 0$ are shown together with the measured profiles after runs LR1 (top), LR13 (middle), and LR35 (bottom). Profile changes in LR1 (Phase 1 in Table 3.1) are more subtle compared to Phase 1 of the HR test. The offshore return flow over the ridge is more important during LR because of no wave overtopping of the wall. The rate of onshore ridge migration, which was about four times slower for LR, is reproduced in the numerical results. As is the case for the HR test, the erosion on the seaward ridge slope, the ridge crest lowering, and the sediment deposition on

the seaward side of the runnel are found in the computed results. Ridge crest and runnel trough elevations after LR1 are reproduced well by the numerical model but erosion on the seaward slope and deposition on the landward slip-face slope of the ridge are underpredicted. The slip-face slope is the steep landward end of the ridge which develops during onshore migration.

Profile changes for $IPOND = 0$ mainly happen seaward of the ridge because sediment settling inside the runnel is not included. In the middle panel of Figure 5.17 (LR13) the computed ($IPOND = 1$) ridge crest is flattened out horizontally and the runnel cross-sectional area is reduced significantly due to overpredicted crest erosion and runnel deposition. Even though the measured seaward ridge slope is not reproduced correctly, the cross-shore location of the predicted runnel trough matches that of the measured LR13 profile. The location of the step at the seaward end of the ridge slope is similar for the measured and the computed profile.

At the end of the LR test (LR35) the computed profile matches the measured beach slope fairly well and the runnel has completely disappeared. The erosion at the toe of the seaward ridge slope, however, is underpredicted. Computed profiles for the LR test resemble their measured counterparts better than for the HR test, possibly because of the reduced ridge-runnel migration speed and the absence of wave overtopping and overwash over the vertical wall.

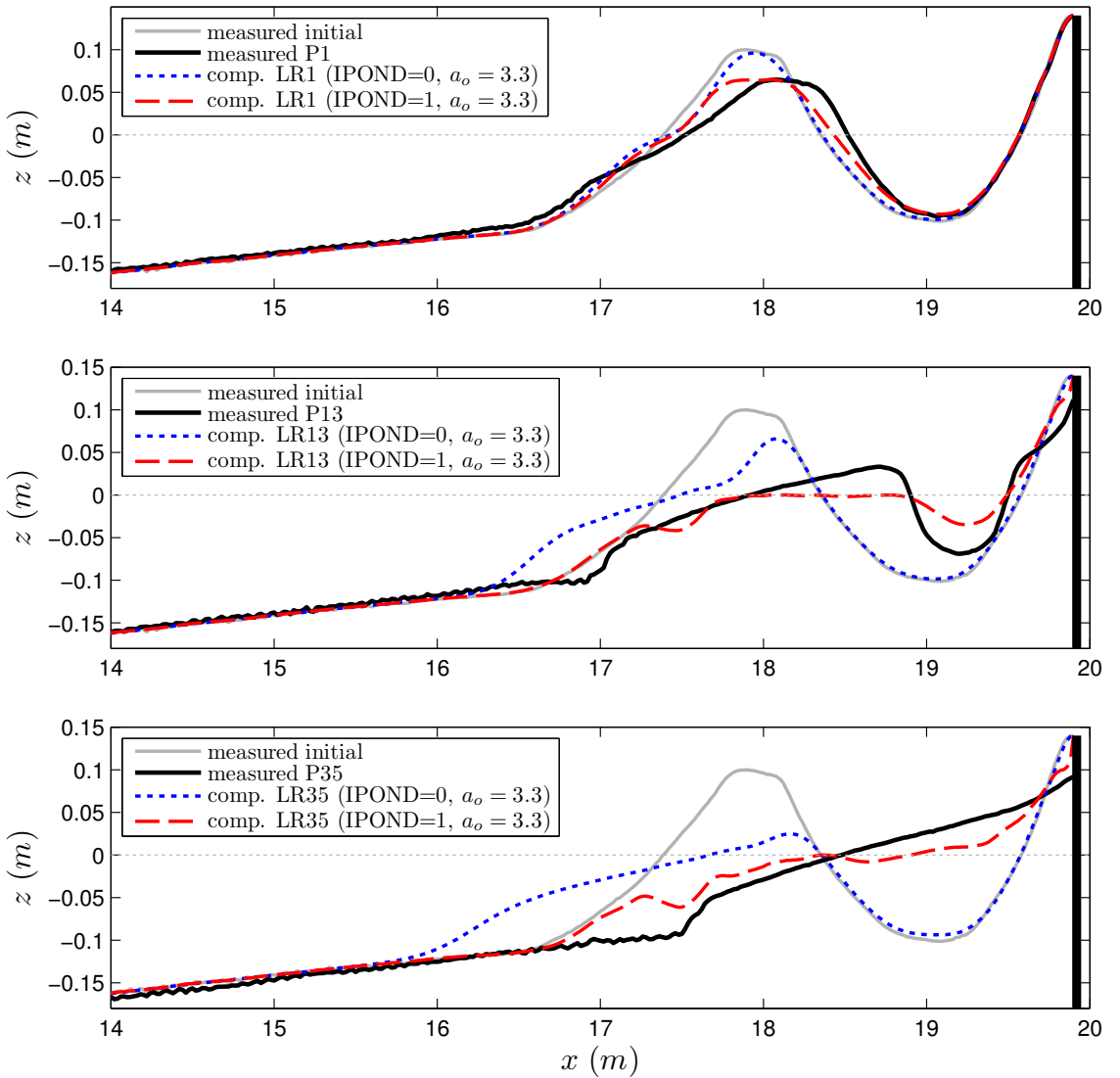


Figure 5.17: Measured and computed ridge-runnel profiles for 3 runs of the LR test. The results for the two computation options $IPOND = 1$ (red dashed lines) and $IPOND = 0$ (blue dotted lines) are shown along with the measured initial profile (gray) and the measured profile of the respective run (black) profiles.

5.4 Wave Overtopping and Overwash Rates

The average wave overtopping rate q_m and the sediment overwash rate q_{bs} during each 400-s run have been determined from the collected water and sand transported over the vertical wall adjacent to the landward end of the runnel. In addition to q_m , CSHORE computes the cross-shore distribution of the bedload transport rate q_b and the suspended load transport rate q_s where $q_{bs} = (q_b + q_s)$ at the end of the computation domain corresponds to the measured sediment transport rate over the wall.

Figure 5.18 shows the measured and computed temporal variations of the wave overtopping rate q_m (top panels) and the sediment transport rate q_{bs} (bottom panels) for the HR and LR tests together. The computed results using $IPOND = 1$ and $a_o = 3.3$ are shown in Figure 5.18. The HR test lasted 4000 s (10 runs) and the LR test lasted 14,000 s (35 runs). Measured data points are averages over the respective run and are plotted at the middle of the each 400-s run. Computed values are plotted continuously.

Only the HR test (blue) included wave overtopping and sediment overwash over the vertical wall. However, in the LR test (red) the vertical wall crest was very close to the wave runup limit. This may explain the numerical prediction of wave overtopping at the rate of $10 \text{ cm}^2/\text{s}$ or less after increasing from close to zero during LR1. Computed sediment overwash is predicted to be negligible for LR as indicated by the red dotted line in the bottom panel. The measured wave overtopping rate at the beginning of the HR test is predicted correctly at a value slightly above $20 \text{ cm}^2/\text{s}$. The subsequent dip in the measured q_m values is not reproduced in the computed time series. Instead, the computed q_m peaks in run HR4 at approximately $40 \text{ cm}^2/\text{s}$ before decreasing again close to the measured values in run HR6. The wave overtopping rate remains close to the measured values during runs HR6-HR10.

The computed initial sediment overwash rate ($q_{bs} = 0.04 \text{ cm}^2/\text{s}$) for the HR

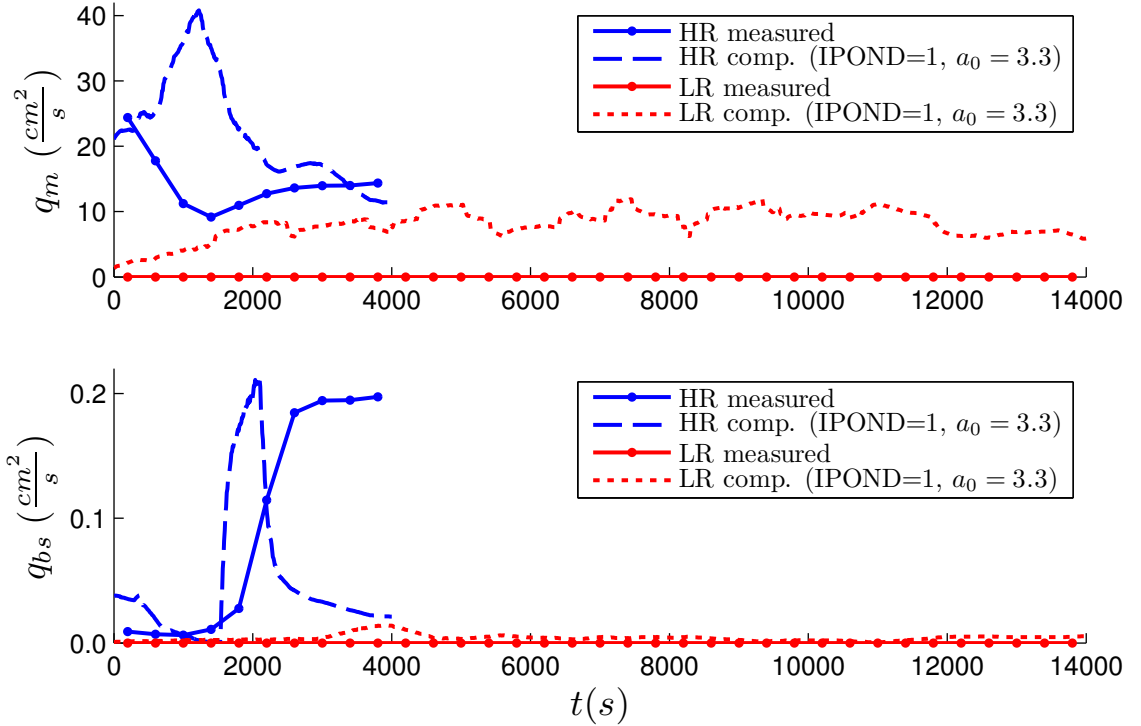


Figure 5.18: Measured and computed wave overtopping rate q_m (top) and sand overwash rate q_{bs} (bottom) for HR (blue) and LR (red) tests at the vertical wall.

test is larger than the measured initial value of $q_{bs} = 0.01 \text{ cm}^2/\text{s}$ but drops to the correct value in run HR2. The rapid transition to larger values of $q_{bs} = 0.2 \text{ cm}^2/\text{s}$ after HR4 is represented fairly well in terms of timing and magnitude even though the computed increase happens quicker (HR5-HR6) than the measured one (HR5-HR7). Contrary to the measured values, which stay constant at the high level of $q_{bs} = 0.2 \text{ cm}^2/\text{s}$ for the remainder of the HR test, the computed time series drops rapidly in HR6 to values below $0.05 \text{ cm}^2/\text{s}$. This may be related to the fact that the beach profile in front of the wall is not well predicted as shown in Figure 5.16.

The comparison shows that the exact evolution of wave overtopping and sediment overwash rate are hard to predict because of the small water depth and velocity above the moveable bed in the wet and dry zone. Even though CSHORE manages

to predict the initial values of wave overtopping and sediment transport closely, further morphological changes and the effect of water ponding in this experiment cause some deviation from the measured values. The fact that the q_{bs} transition time and magnitude are predicted correctly for the HR test shows that CSHORE can deal with water ponding but the sediment transport model for erosion in front of the wall needs to be improved further by more detailed measurements of hydrodynamics and sediment transport variables on sloped beaches in front of the wall. The instrument deployment arranged for the ridge-runnel profile evolution in this experiment will need to be modified for such detailed measurements.

Chapter 6

VERIFICATION OF CSHORE

Figlus et al. (2009) conducted three laboratory dune overwash tests and modified CSHORE to extend its capability to major overwash events. They introduced the new overwash parameter a_o in Equation (4.31) which needs to be calibrated depending on the severity of overwash. The profile changes, wave overtopping rates and sediment transport rates from these three tests with major overwash are compared with the new CSHORE version with $IPOND = 0$ and 1 in the following.

Kobayashi et al. (2010) used a previous version of CSHORE to assess profile changes measured in two laboratory studies and at two field sites. The laboratory studies included two tests with no or minor overtopping by Kobayashi et al. (2009) and three dune erosion tests by van Gent (2008). The field measurements comprised pre- and post-storm surveys of Delaware and Maryland beaches (Wise et al., 1996). CSHORE is also compared to these measured data to show that the present version of the program can predict profile evolution in the laboratory and in the field with similar or better accuracy as previous versions even if no or only little overtopping occurs. All comparisons are shown for $IPOND = 0$ and $IPOND = 1$ to assess the benefits of including wave ponding in the computations. The parameter a_o is adjusted to the prevailing overtopping and overwash conditions.

6.1 Laboratory Dune Data

Figlus et al. (2009) conducted three laboratory dune overwash tests (BD, WD, and SD) using the same experimental setup as in Chapter 2 to investigate the

transition from minor to major overwash and the resilience to destruction of various dune shapes. Measured data included detailed profile scans, wave overtopping rates and sediment overwash rates over the vertical wall landward of the dune. Profile and overwash evolution was separated into three distinct phases. Phase 1 included the initial adjustment of the profile to the incident wave conditions with only little overtopping and overwash. In Phase 2 the transition from minor to major overwash occurred and the dune in each test was destroyed by wave overtopping. Erosion of a sloped beach in front of a vertical wall occurred in Phase 3.

Figure 6.1 compares the measured profiles of the BD, WD, and SD tests to the computed ones using both $IPOND = 0$ (dashed lines) and $IPOND = 1$ (dotted lines). Results are shown for the region of major profile change ($x = 16\text{--}20\text{ m}$) at the end of each evolution phase with the respective run (400-s wave burst) numbers listed in each panel. The parameter a_o is calibrated individually for each test to values of 2.2, 3.6, and 3.2 for the BD, WD, and SD test, respectively. A comparison between individually calibrated and average a_o values indicates that profile changes are not very sensitive to small variations in a_o (Figlus et al., 2009). The comparison between the $IPOND = 0$ and $IPOND = 1$ results shows that both computation options represent profile changes in Phases 1 and 2 fairly well but underpredict erosion in front of the wall. The same was found by Figlus et al. (2009). The inclusion of water ponding, however, reduces the depth of artificial dips in the computed profiles. In other words, the option of $IPOND = 1$ tends to remedy the tendency of CSHORE to produce an erosion hole in front of the vertical wall.

The time series of the wave overtopping rate q_m and the sediment overwash rate q_{bs} for the BD, WD, and SD tests is reexamined in Figure 6.2 with focus on the comparison of the computation options $IPOND = 0$ and $IPOND = 1$ in the latest CSHORE version. Wave overtopping and sediment transport rates are both sensitive to the choice of computation option. For $IPOND = 1$, the shape

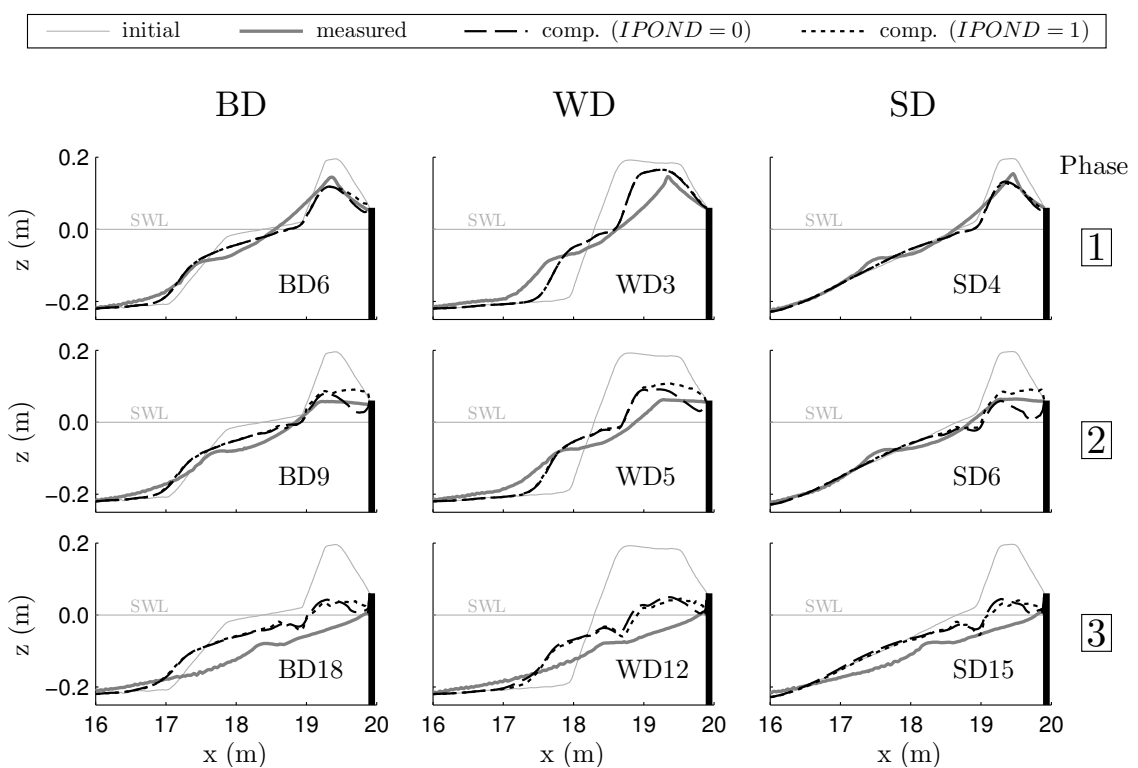


Figure 6.1: Measured and computed profiles for BD, WD, and SD tests.

and magnitude of both rates are predicted slightly better. Computed overtopping rates show a smoother and more accurate evolution and the overprediction of peak sediment transport rates is eliminated. In addition, the gradual decrease in q_{bs} values after the peak is modeled better if $IPOND = 1$ is employed. In general, the inclusion of water ponding improves the CSHORE predictions for profile changes, wave overtopping and sediment overwash for these three tests even if no ridge-runnel systems exist initially.

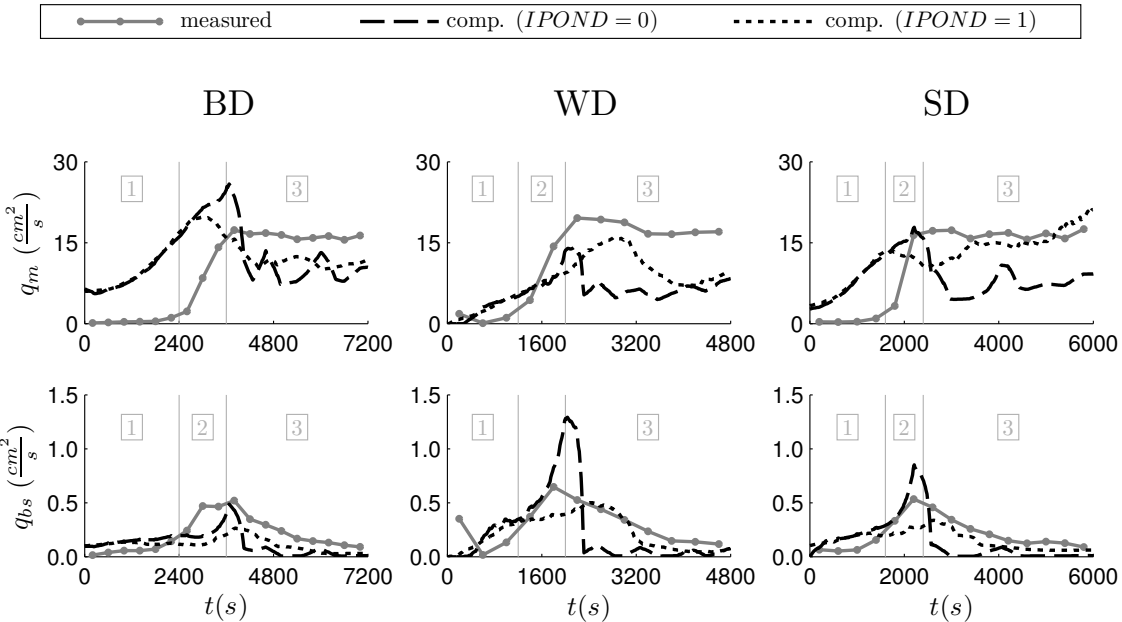


Figure 6.2: Measured and computed wave overtopping and sediment transport rate for BD, WD, and SD tests.

Kobayashi et al. (2009) conducted two small-scale experiments on berm and dune erosion for a high and narrow berm (Experiment H) as well as a low and wide berm (Experiment L). The sand volume for the different berms was approximately the same. The experiments were conducted in the same sand tank as in Chapter 2. The median diameter, fall velocity, specific gravity, and porosity of the fine sand were 0.18 mm , 2.0 cm/s , 2.6 and 0.4 , respectively. The significant wave height and spectral peak period were approximately 19 cm and 2.6 s , respectively. The still

water level S above the datum corresponding to the initial water level at time $t = 0$ was varied by an increment of 5 or 10 cm during each experiment that lasted 6.11 hours to simulate the changing water level during a storm.

Figures 6.3 and 6.4 compare the measured and computed profiles at time $t = 2.0, 3.67$, and 6.11 h starting from the initial profile at $t = 0$ for Experiments H and L, respectively. Measured initial profile and profile at each plotted time level are displayed as solid lines whereas computational results are shown as dashed red and dotted blue lines. Two different computational results are shown, both using $IPOND = 0$ and $a_o = 0.1$, since the $IPOND$ option had only little effect on the profile changes with no ponded water and $a_o = 0.1$ is calibrated for this experiment with only minor wave overtopping. The bedload parameter b and the constant friction coefficient f_b are different. The result shown as dotted blue lines pertains to $b = 0.001$ and $f_b = 0.002$ as used by Kobayashi et al. (2010) whereas the result shown as dashed red lines utilizes $b = 0.002$ and $f_b = 0.015$ which are the calibrated values used throughout this report. The maximum still water level (SWL) was 15 cm above the datum during $t = 3.0 - 3.67\text{ h}$. Erosion on the dune face above SWL and corresponding deposition below SWL is slightly overpredicted at all time levels.

The agreement of the dune profile evolution in Figure 6.3 and the agreement in Figure 6.4 are similar to those presented by Kobayashi et al. (2010) using the numerical model without the overtopping term $a_o U_a V_s$ in Equation (4.31) but with the other parameter a in Equation (4.31) modified to unity in the unidirectional flow zone of $\bar{U} > 0$ over the dune crest. The computed cross-shore variations of the sediment transport rates q_b and q_s given by Equations (4.30) and (4.31) indicate that the dune erosion in Experiments H and L was caused predominantly by the offshore transport of suspended sand seaward of the dune crest.

Comparison is also made with the large-scale dune erosion tests by van Gent (2008). The median diameter, fall velocity, specific gravity and porosity of the fine

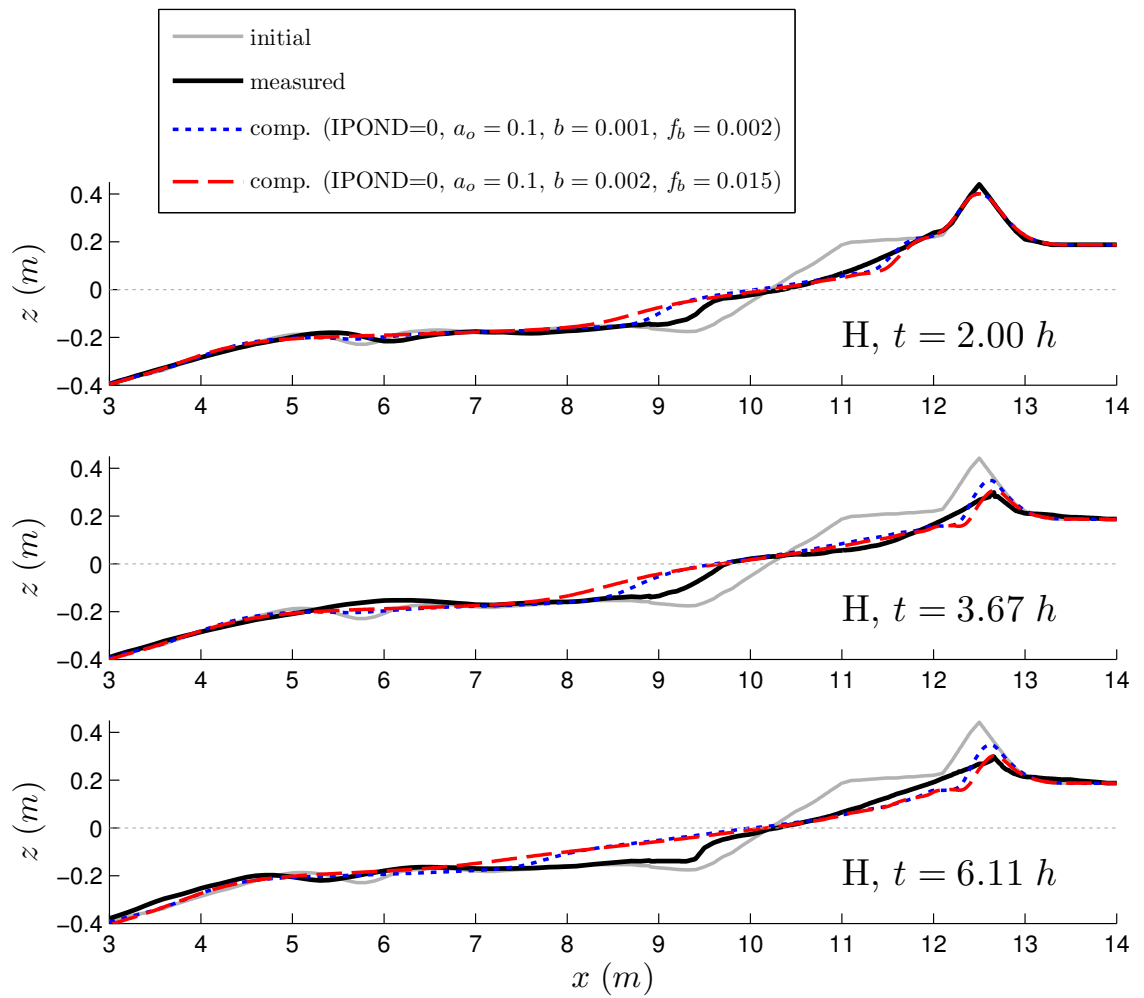


Figure 6.3: Measured and computed profiles for Experiment H.

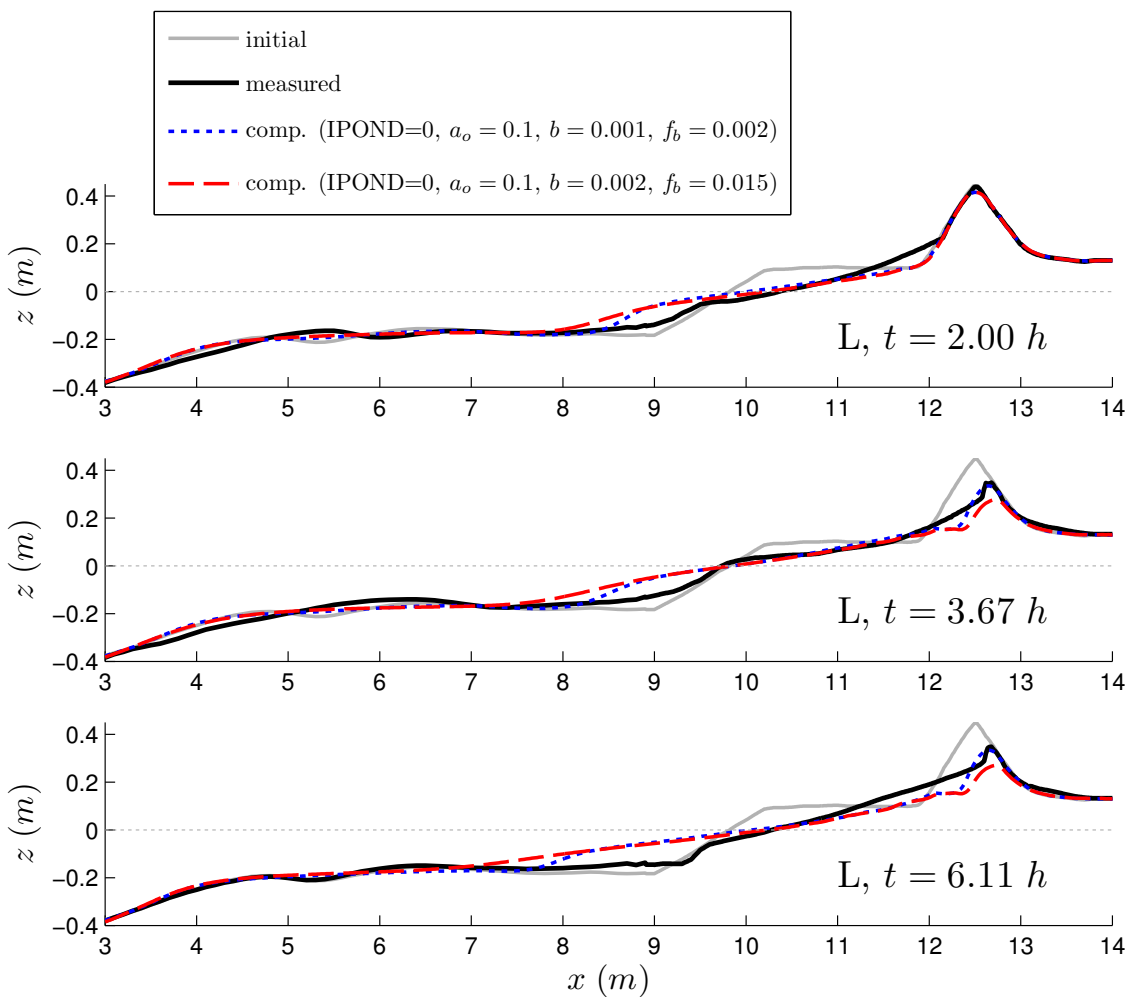


Figure 6.4: Measured and computed profiles for Experiment L.

sand used in these tests were 0.20 mm , 2.5 cm/s , 2.65 and 0.4 , respectively. The still water level was constant in three tests $T01$, $T02$ and $T03$. The spectral peak period was 4.9 , 6.1 and 7.3 s for tests $T01$, $T02$ and $T03$. The significant wave height was 1.41 , 1.49 and 1.52 m for tests $T01$, $T02$ and $T03$. The duration of each test was 6 hours. Figure 6.5 compares the measured and computed profiles at the end ($t = 6\text{ h}$) of the three tests where $a_o = 0.1$ is chosen since little or no overwash occurred. Computed results are presented for the same two parameter sets as in the previous comparison for the L and H experiments. $IPOND = 0$ is used for both computations. The dotted blue lines show the computed results using $b = 0.001$ and $f_b = 0.002$ and the dashed red lines pertain to computation results utilizing $b = 0.002$ and $f_b = 0.015$. Again, these two different parameter sets produce only minute differences in computed profile change behavior for these large-scale tests.

The numerical model underpredicts the dune erosion and corresponding de-positional area in contrast to the comparison shown in Figures 6.3 and 6.4. The agreement in Figure 6.5 is similar to that obtained by Kobayashi et al. (2009) using a scarping procedure with no wet and dry zone. The present computation reaches the landward end located at $x = 184\text{ m}$ but the computed overtopping and overwash rates are essentially zero. The present explicit modeling of the sediment transport on the steep dune face does not cause sufficient dune erosion perhaps because the computed offshore transport of suspended sediment at the toe of the eroding dune face is underpredicted.

The laboratory profile data presented in this section spans cases from major overwash to little or no overwash. The comparisons are useful in assessing the validity of the present CSHORE version. The present version of CSHORE with the modified suspended sediment transport equation (4.31) can predict profile evolution for laboratory situations ranging from no wave overtopping and overwash to major wave overtopping and overwash if the parameter a_o is calibrated. The choice of

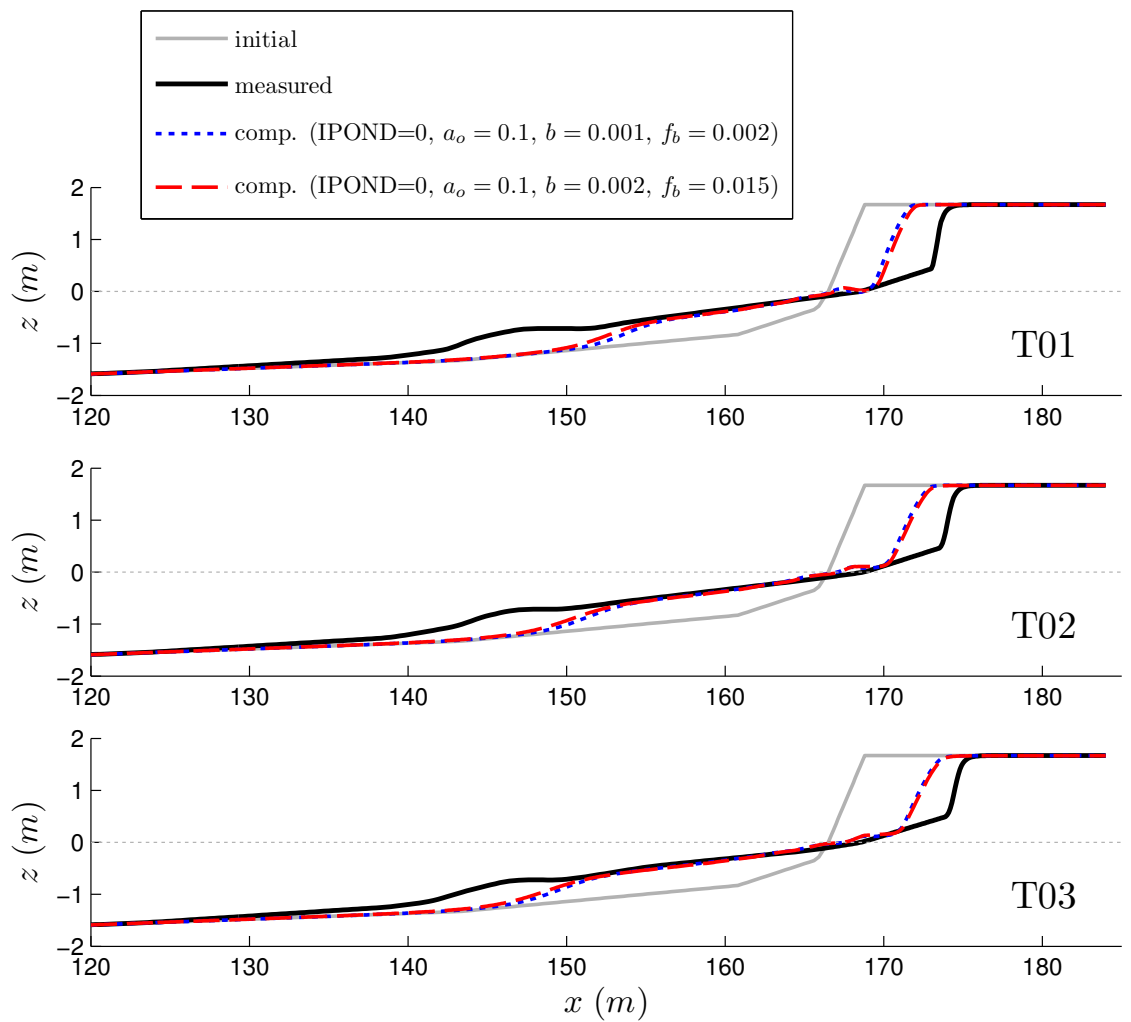


Figure 6.5: Measured and computed profiles for tests T0, T1, and T3.

$IPOND = 0$ or $IPOND = 1$ is shown to have essentially no effect on profile evolution in the absence of water ponding in the computation domain. Furthermore, the two different combinations of the bedload parameter b and bottom friction factor f_b produce very similar beach and dune profile evolutions for these laboratory experiments using fine sands because suspended load is dominant in these laboratory experiments. In the following section, comparisons with field data are presented. Use is made of $b = 0.001$ and $f_b = 0.002$ in the field data comparisons as in Figlus et al. (2009).

6.2 Field Dune Data

Only few field data sets describing overwash of dunes are available. They are limited to pre- and post-storm profile measurements with considerable time lag between surveys. Flow velocities on the backdune, overtopping and overwash rates during dune overwash have not been measured in the field. This lack of measured hydrodynamic variables makes the numerical model calibration for such cases more difficult. In the following, CSHORE is compared with field data of overwashed dune profiles obtained at two locations at Ocean City, Maryland and one location at Dewey Beach, Delaware (Wise et al., 1996). The numerical results for $IPOND = 0$ and $IPOND = 1$ are shown to be identical in the following since no ridge-runnel systems and no vertical wall at the end of the computation domain are present.

The beach at Ocean City, Maryland was impacted by the 30 October 1991 storm, 11 November 1991 storm, and 4 January 1992 storm after a major beach nourishment project. Wave and water elevation time series were measured at a depth of approximately 10 m. This location is taken as the seaward boundary $x = 0$ for the CSHORE computation. The October storm lasted about 4 days, with a peak significant wave height of approximately 3 m and a peak water level of 1.5 m above the datum $z = 0$ taken as the National Geodetic Vertical Datum (NGVD). The November storm lasted about 3 days with a peak significant wave height of 3 m and a peak water level of 1.2 m. The January storm lasted about 3 days with a peak significant wave height of 4 m and a peak water level of 2 m. The assumption of normally incident waves is made for lack of directional wave information. The median sand diameter was $d_{50} = 0.35 \text{ mm}$.

Figure 6.6 shows the comparison for Profile OJ86 in the report by Wise et al. (1996). The initial profile corresponds to the measured profile on 26 June 1991. The measured profile after the three storms was obtained on 11 January 1992. Measured pre and post storm profiles are displayed as thin and thick solid lines, respectively.

The computation was carried out for the combined time series of the waves and water level for the three storms over the duration of 371 hours, neglecting the intervals between the storms. Only the zone of noticeable profile changes is shown in this and subsequent figures. The overwash parameter a_o is set to 0.1 for all the field data presented here.

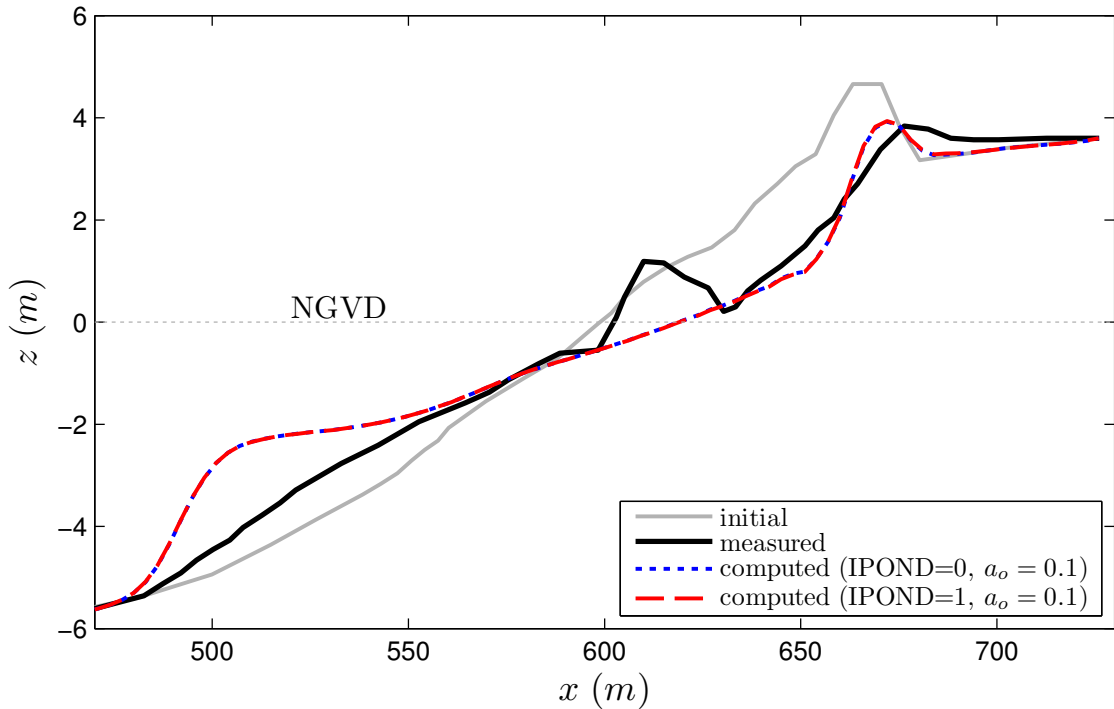


Figure 6.6: Measured and computed beach profile (No.86) for Ocean City, MD. Surveys were conducted in June 1991 and January 1992. Computed profile evolution is based on the combined time series of three storms between the surveys.

CSHORE predicts the dune crest elevation well but underpredicts its onshore migration by approximately 10 m. The present numerical model with $a_o = 0.1$ predicts the overwashed dune profile well but does not predict the berm near the shoreline perhaps because the beach recovery after the January storm is not simulated. The computed wave overtopping rate q_o per unit width at the landward end located at $x = 726$ m is as large as $0.14 \text{ m}^2/\text{s}$ for a few hours. The corresponding suspended

sand and bedload transport rates are $q_s = 1.6 \text{ cm}^2/\text{s}$ and $q_b = 0.25 \text{ cm}^2/\text{s}$. The present numerical model does not predict the deposition landward of the dune crest possibly because it does not include the lateral spreading in the dry zone landward of the dune crest. The computed profiles indicate that the dune erosion for OJ86 must have been caused mostly by offshore sand transport.

Figure 6.7 shows the comparison for Profile NJ74 where the initial profile corresponds to the measured profile on 2 November 1991 after the October storm. The measured profile was surveyed on 11 January 1992. The computed profiles for $IPOND = 0$ and 1 are based on the computations made for the combined time series of the waves and water level for the November and January storms over the duration of 168 hours. The computed profiles show reasonable agreement in dune crest elevation but the landward migration of the dune crest is not predicted. Computed q_o at the landward end ($x = 510 \text{ m}$) is as large as $0.18 \text{ m}^2/\text{s}$ for a few hours. The corresponding sand transport rates are $q_s = 2.5 \text{ cm}^2/\text{s}$ and $q_b = 0.45 \text{ cm}^2/\text{s}$. Comparison of the initial and final measured profiles suggests that the dune crest lowering must have been caused mostly by offshore sand transport.

Comparison is also made with dune erosion data with no dune crest lowering in the report by Wise et al. (1996). The beach at Dewey Beach, Delaware was attacked by a storm on 10 December 1992. A wave gauge was located at a depth of 9 m off the coast of Dewey Beach. This location is taken as $x = 0$. This storm lasted about 4 days with a peak significant wave height of 4 m and a peak water level of approximately 2 m . The median sand diameter was $d_{50} = 0.33 \text{ mm}$. The beach profile was surveyed on 29 October 1992 and 18 December 1992. Computation is made for the duration of 6 days only. Figure 6.8 shows the comparison for Dewey Beach profile 140. The storm completely eroded the berm and parts of the dune face in the initial profile and transported the sediment offshore. CSHORE computations for $IPOND = 1$ and 0 are shown using $a_o = 0.1$. The computed final profiles

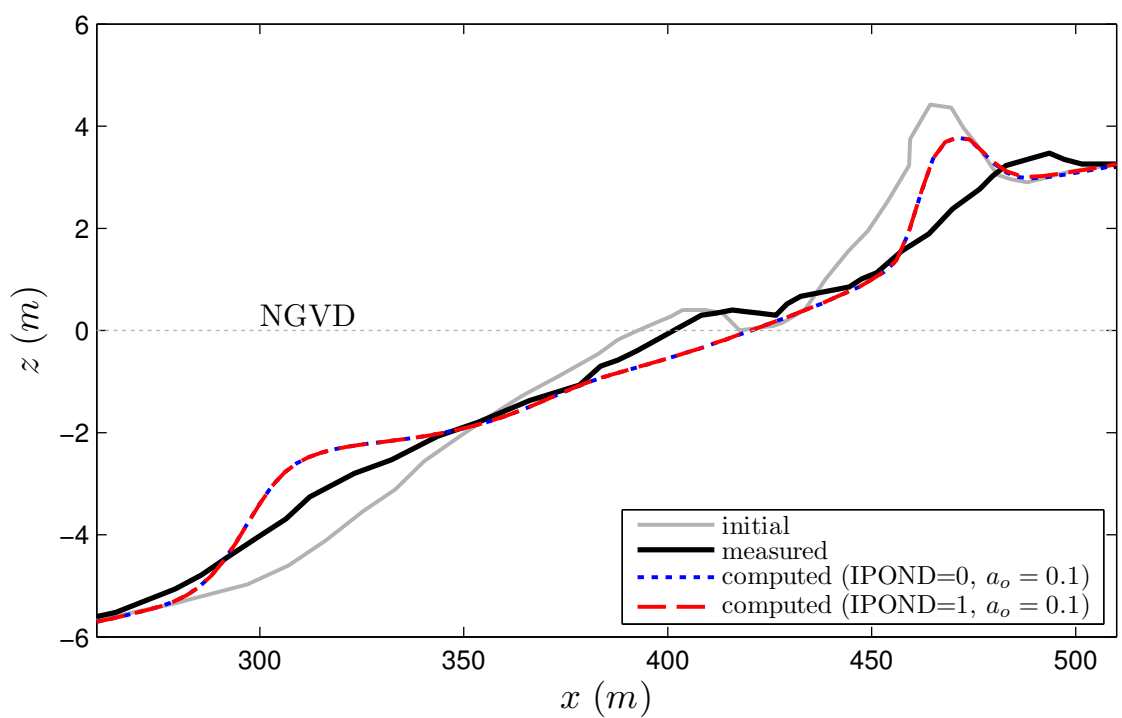


Figure 6.7: Measured and computed beach profile (No.74) for Ocean City, MD. Surveys were conducted in November 1991 and January 1992. Computed profile evolution is based on the combined time series of two storms between the surveys.

are identical because the berm is eroded before water ponding between the berm and dune affects the dune erosion. The computed profiles indicate slight erosion of the landward slope of the dune where the computed bedload transport rate at the landward end located at $x = 459\text{ m}$ is $q_b = 0.4\text{ cm}^2/\text{s}$ for several hours. The corresponding computed suspended sand transport rate reaches maximum values of $q_s = 0.8\text{ cm}^2/\text{s}$. Dune crest lowering is predicted by both computation options but the measured profiles did not show any crest lowering. This implies that the offshore sand transport rate on the seaward slope of the dune is overpredicted. The numerical model does not predict the seaward spreading of the deposited sand perhaps because of the assumption of normally incident waves and no longshore current. Longshore current increases the volume of suspended sediment which can be transported offshore by return (undertow) current.

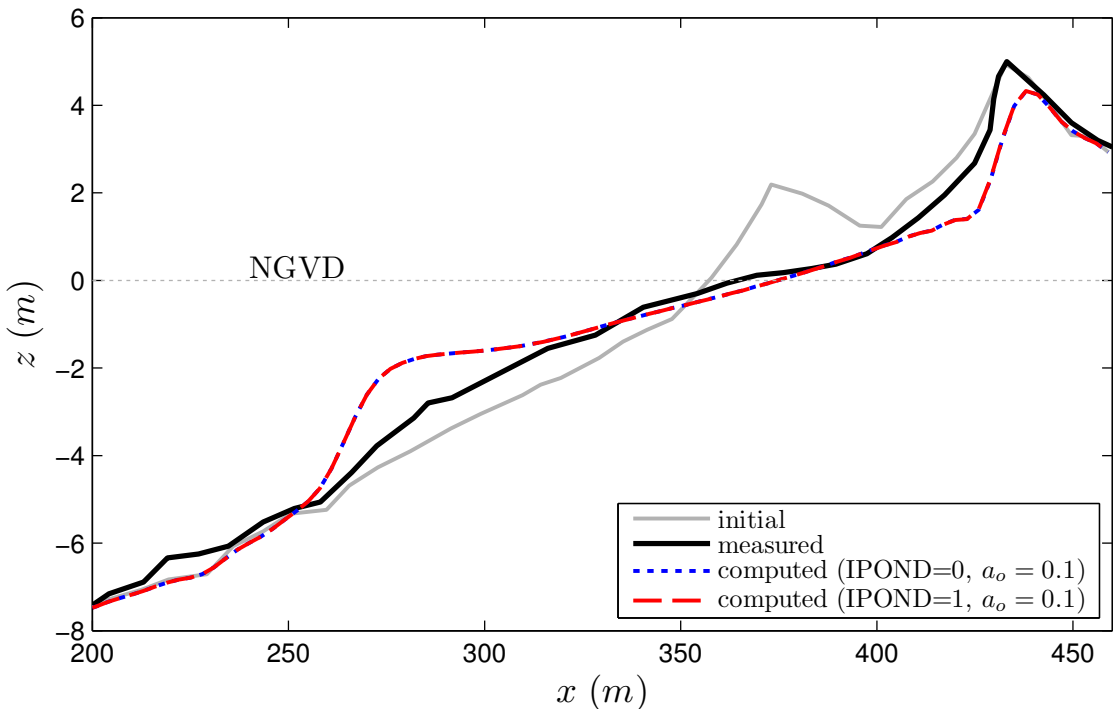


Figure 6.8: Measured and computed beach profiles for Dewey Beach profile 140. Surveys were conducted in October and December 1992. Computed profile evolution is based on the time series of a 6-day storm in December 1992.

The degree of the agreement for the field data in Figures 6.6 - 6.8 is practically the same as for the compared results presented in Figlus et al. (2009) using the previous version of CSHORE. The numerical model is not calibrated for the field data alone because of the additional assumptions made for the field data comparison such as the assumption of normally incident waves and no profile change during the intervals before, between, and after the storms specified as input. Computation will need to be extended to the interval of beach recovery to assess the capability of the present numerical model in predicting beach recovery after a storm.

Chapter 7

CONCLUSIONS

Ridge-runnel systems can comprise large volumes of sand. Thus, their migration can influence the coastal sediment budget significantly. Wave-induced ridge-runnel migration was investigated in a moveable-bed flume experiment. Two similar initial ridge-runnel profiles at different elevations were built with fine sand in front of a low-crested vertical wall to mimic two different runnel drainage scenarios found in natural ridge-runnel systems. The High Ridge (HR) test allowed for wave overtopping of the vertical wall to simulate drainage of the runnel through rip-channels. In the Low Ridge (LR) test water could only exit the runnel as offshore return flow over the ridge crest similar to alongshore uniform ridge-runnel systems in nature. The still water levels were kept constant during each test. A cross-shore array of eight capacitance wave gauges and up to three acoustic Doppler velocimeters provided hydrodynamic data during a total of 45 runs, each with 400 s of irregular waves.

Detailed free-surface and velocity measurements were taken in the ponded water zone of the runnel and in the intermittently wet and dry zone on the ridge crest to investigate the effect of water ponding and runnel drainage on ridge migration. A laser line scanner system consisting of two distance lasers, a rotating mirror assembly and a motorized cart recorded 3D bathymetry in high resolution in a continuous fashion. The 3D bathymetry was measured before each test and after noticeable profile changes. Water and sediment transported over the low-crested vertical wall

behind the runnel in the HR test were collected in a basin with a sand trap. The trapped sand volume and collected water volume were used to obtain the wave overtopping rate and onshore sediment transport rate for each HR run. Both tests were continued until the ridge-runnel system was completely smoothed out by the wave action and a sloping beach was formed in front of the wall.

Three phases of the observed profile evolution were identified in both tests. Phase 1 was confined to the first 400-s run in each test and included initial ridge crest lowering and runnel filling with relatively rapid onshore ridge migration. In Phase 2 the ridge-runnel cross-sectional area reduced progressively until the entire feature blended into a sloping beach. Phase 3 consisted of the evolution of the sloping beach in front of the vertical wall. In the LR test this sloping beach was at equilibrium but in the HR test wave overtopping over the vertical wall led to continued onshore sediment transport over the vertical wall. In both tests the ridge migrated onshore, but at different speeds. Ridge migration in Phase 2 of the HR test was five times faster than in the LR test because of the allowed wave overtopping of the vertical wall landward of the runnel. This suggests that rapid beach recovery may occur if the runnel is drained through rip channels. The landward slip-face of the onshore migrating ridge was steeper for the LR test with a gentler seaward ridge slope due to the increased importance of the offshore return flow out of the runnel over the ridge crest opposing the incident waves breaking on the seaward ridge slope.

Water ponding inside the runnel affected the hydrodynamics and sediment transport patterns because the reduced flow velocities in the runnel led to increased sediment settling. The numerical model CSHORE is modified to account for water ponding in the wet and dry zone of the profile to improve the prediction of measured hydrodynamics, profile change and overwash rate in the experiment. The sediment settling in the ponded water is modeled using an exponential decay factor with its cross-shore length scale based on the runnel width and the overwash parameter a_o .

This modification mimics settling of sediment transported over the ridge crest onto the seaward side of the runnel in order to produce onshore ridge migration and runnel filling as observed in the experiment. The strong feedback of the rapid bathymetric change to the wave motion in very small water depths over the ridge, in the runnel and over the vertical wall makes the time-averaged numerical modeling challenging because of the highly unsteady hydrodynamics. Planned future experiments include detailed hydrodynamic measurements on sloping beaches in front of the wall during Phase 3 to gain a better insight into the complicated processes which are not predicted well by the present CSHORE. Detailed laboratory experiments are essential in guiding the development of realistic numerical models.

The versatility and consistency of the present CSHORE was further demonstrated by comparing the numerical model to additional laboratory experiments and available field data previously presented in Figlus et al. (2009). Comparison of CSHORE with three sets of laboratory dune experiments showed that the adjustment of the overtopping parameter a_o in the suspended sediment transport formulation is sufficient to obtain similar agreement for profile evolutions with no, minor, and major overwash. The water ponding routine was found to smooth out spurious profile dips computed in front of the vertical wall. The overwash parameter a_o will need to be evaluated further in the future because the present CSHORE differentiates minor and major overwash by specifying different values of a_o as input.

The comparison of CSHORE with pre and post storm profiles of dune overwash and dune erosion has shown that the new CSHORE version reproduces field profile changes with the same accuracy as the previous version. The water ponding routine does not affect these particular computations involving no runnel or dip during the profile evolution. The two-dimensional effect of lateral spreading of overwash flow and overwash sediment on the landward side of the dune is not included in this cross-shore one-dimensional model. Further improvements of the numerical model

may require lateral spreading of overwash in the sediment transport formulation as well as the prediction of beach recovery after a storm to improve and expand its field applications.

References

- Aagaard, T., Hughes, M., Møller-Sørensen, R., and Andersen, S. (2006). Hydrodynamics and sediment fluxes across an onshore migrating intertidal bar. *Journal of Coastal Research*, 22(2):247–259.
- Acuity (2003a). *AccuRange 1000 laser distance sensor user's manual*. Schmitt Measurement Systems, Inc.
- Acuity (2003b). *AccuRange 4000 laser rangefinder and AccuRange line scanner user's manual*. Schmitt Measurement Systems, Inc.
- Battjes, J. and Stive, M. (1985). Calibration and verification of a dissipative model for random breaking waves. *Journal of Geophysical Research*, 90(C5):9159–9167.
- Boers, M. (1996). Simulation of a surf zone with a barred beach: Part 1: wave heights and wave breaking. Communication on Hydraulic and Geotechnical Engineering, Report No. 96-5, Delft University of Technology, Delft.
- de Vriend, H. J., Capobianco, M., Chesher, T., de Swart, H. E., Latteux, B., and Stive, M. J. F. (1993). Approaches to long-term modelling of coastal morphology: A review. *Coastal Engineering*, 21:225–269.
- Dunnum, C. (2006). *CTI-HSIF-PCI software library for Acuity AR4000 laser distance sensors and PCI High-Speed Interface Card programmer's guide and reference manual*. Crandun Technologies, Inc.

Figlus, J., Kobayashi, N., and Gralher, C. (2010). Wave-induced overwash and destruction of sand dunes. In *Proceedings of the 32nd International Conference on Coastal Engineering*. (accepted for publication).

Figlus, J., Kobayashi, N., Gralher, C., and Iranzo, V. (2009). Experimental and numerical study on the transition from minor to major wave overwash of dunes. Research Report CACR-09-04, University of Delaware, Center for Applied Coastal Research.

Goda, Y. (2000). *Random seas and design of maritime structures*, volume 15 of *Advanced Series on Ocean Engineering*. World Scientific, Singapore.

Gralher, C. (2010). Experimental study on the migration of coastal ridge and runnel systems. Diploma thesis, Leibniz University of Hanover, Germany.

Holland, K. T., Holman, R. A., and Asbury H. Sallenger, J. (1991). Estimation of overwash bore velocities using video techniques. In Kraus, N. C., editor, *Coastal Sediments '91*, volume 1, pages 489–487. ASCE.

Holtz, R. D. and Kovacs, W. D. (1981). *An introduction to geotechnical engineering*. Prentice Hall, Englewood Cliffs, N.J.

Houser, C. and Greenwood, B. (2007). Onshore migration of a swash bar during a storm. *Journal of Coastal Research*, 23(1):1–14.

Kobayashi, N., Buck, M., Payo, A., and Johnson, B. D. (2009). Berm and dune erosion during a storm. *Journal of Waterway, Port, Coastal, and Ocean Engineering*, 135(1):1–10.

Kobayashi, N., Cox, D. T., and Wurjanto, A. (1990). Irregular wave reflection and run-up on rough impermeable slopes. *Journal of Waterway, Port, Coastal, and Ocean Engineering*, 128:238–248.

- Kobayashi, N., DeSilva, G., and Watson, K. (1989). Wave transformation and swash on gentle and steep slopes. *Journal of Geophysical Research*, 94(C1):951–966.
- Kobayashi, N., Farhadzadeh, A., Melby, J. A., Johnson, B. D., and Gravens, M. (2010). Wave overtopping of levees and overwash of dunes. *Journal of Coastal Research*, (in press).
- Kobayashi, N., Herrman, M., Johnson, B. D., and Orzech, M. (1998). Probability distribution of surface elevation in surf and swash zones. *Journal of Waterway, Port, Coastal, and Ocean Engineering*, 124(3):99–107.
- Kobayashi, N., Meigs, L. E., Ota, T., and Melby, J. A. (2007). Irregular breaking wave transmission over submerged porous breakwater. *Journal of Waterway, Port, Coastal, and Ocean Engineering*, 133(3):104–116.
- Kobayashi, N., Payo, A., and Schmied, L. (2008). Cross-shore suspended sand and bed load transport on beaches. *Journal of Geophysical Research*, 113(C07001).
- Kobayashi, N., Zhao, H., and Tega, Y. (2005). Suspended sand transport in surf zones. *Journal of Geophysical Research*, 110(C12009):1–21.
- Masselink, G. (2004). Formation and evolution of multiple intertidal bars on macrotidal beaches: application of a morphodynamic model. *Coastal Engineering*, 51:713–730.
- Masselink, G., Kroon, A., and Davidson-Arnott, R. G. D. (2006). Morphodynamics of intertidal bars in wave-dominated coastal settings - a review. *Journal of Geomorphology*, 73:33–49.
- Mei, C. C. (1989). *The applied dynamics of ocean surface waves*, volume 1 of *Advanced Series on Ocean Engineering*. World Scientific, Singapore.

- Robin, N., Levoy, F., and Monfort, O. (2009). Short term morphodynamics of an intertidal bar on megatidal ebb delta. *Marine Geology*, 260:102–120.
- Tega, Y. and Kobayashi, N. (1996). Wave overwash of subaerial dunes. In *Proceedings of the 25th International Conference on Coastal Engineering*, pages 4148–4160. World Scientific, Singapore.
- van Gent, M. (2008). Large-scale tests to analyse the influence of collapsed dune revetments on dune erosion. In *Proceedings of the 31st International Conference on Coastal Engineering*, volume 3, pages 2583–2595. World Scientific, Singapore.
- Vincent, C. E. and Green, M. O. (1990). Field measurements of the suspended sand concentration profiles and fluxes and of the resuspension coefficient γ_0 over a rippled bed. *Journal of Geophysical Research*, 95(C7):11,591–11,601.
- Wise, R. A., Smith, S., and Larson, M. (1996). SBEACH: Numerical model for simulating storm-induced beach change. Report 4. cross-shore transport under random waves and model validation with SUPERTANK and field data. Technical Report CECR-89-9, U.S. Army Engineer Waterways Experiment Station.